12-13-2019

Numerical modeling of compacted fills under landing mats subjected to aircraft loads

Jeremiah Matthew Stache

Numerical modeling of compacted fills under landing mats subjected to aircraft loads

By

Jeremiah Matthew Stache

A Dissertation
Submitted to the Faculty of
Mississippi State University
in Partial Fulfillment of the Requirements
for the Degree of Doctor of Philosophy
in Civil Engineering
in the Department of Civil and Environmental Engineering

Mississippi State, Mississippi

December 2019

Numerical modeling of compacted fills under landing mats subjected to aircraft loads

By

Jeremiah Matthew Stache

Approved:

_____

Farshid Vahedifard
(Major Professor/Graduate Coordinator)

_____

John F. Peters
(Committee Member)

_____

Isaac L. Howard
(Committee Member)

_____

Youssef Hammi
(Committee Member)

_____

Paul F. Mlakar
(Committee Member)

_____

Jason M. Keith
Dean
Bagley College of Engineering

Name: Jeremiah Matthew Stache

Date of Degree: December 13, 2019

Institution: Mississippi State University

Major Field: Civil Engineering

Major Professor: Farshid Vahedifard

Title of Study: Numerical modeling of compacted fills under landing mats subjected to aircraft loads

Pages in Study: 126

Candidate for Degree of Doctor of Philosophy

Rutting failures are prominent in expedient airfields constructed with AM2 landing mats over soft existing subgrades. There are many issues that must be addressed when approaching this multi-faceted problem. The load transfer mechanism occurring at interlocking mat joints and the mat-soil interface bonding condition affect near surface subgrade response. The repeated loading coupled with lateral aircraft wander causes significant principal stress rotation in the subgrade. This kneading action then causes variations in the excess pore-water pressure and a subsequent softening of the soil. The purpose of this study is to investigate the critical factors that lead to subgrade rutting failures in landing mats constructed over soft subgrades. A three dimensional finite element (3D FE) model of a landing mat system over soft subgrade is implemented under both static and pseudo-dynamic loading conditions with aircraft wander. To capture the complex stress histories induced by the simulated moving gear loads over the unique structural features of the AM2 mat system, an elastoplastic kinematic hardening constitutive model, the Multi-Mechanical Model, is developed, calibrated and used to represent the subgrade response. Under both static and pseudo-dynamic loading, the FE model results match very well with the stress and deformation results from full-scale instrumented testing of the AM2 mat over

6 CBR subgrade. Results show that incorporating the load transfer mechanism occurring at the mat joints and varying the mat-soil interface condition affect the near surface subgrade deformation and stress responses that contribute to rutting failures. Furthermore, rotation of the principal stress axes and changes in excess pore-water pressures occur in the subgrade because of the moving tire load. These phenomena contribute to extension of the field of deformation influence around the trafficked area in the subgrade and upheaval at the edges of the test section. Findings of this study show that although layered elastic analysis procedures are the basis of current airfield design methodologies, critical design features and the corresponding deformation responses can be better modeled using the FE approach. Furthermore, the proposed 3D modeling approach implementing aircraft wander can provide a reliable platform for accurately simulating the subgrade response under pseudo-dynamic loading conditions.

DEDICATION

To my wife *Erin* and my daughter *Bayley Ann*.

ACKNOWLEDGEMENTS

I would like to express my gratitude to Dr. Farshid Vahedifard for his constant support throughout my PhD research. He has proven to be a very knowledgeable, dedicated, and patient advisor, and I feel very fortunate to have been mentored by him.

I would also like to thank Dr. John Peters for the countless hours he willingly spent in the GSL conference room with me as he clarified the finer details of Endochronic Theory and aided me significantly in my subsequent modeling efforts. I am deeply indebted to him for all he has done for me.

I would like to thank Dr. Paul Mlakar for helping me get started on this project and walking with me throughout this journey. He has been a great mentor and friend.

I would like to thank Dr. Isaac Howard for his many helpful comments to me at crucial stages of my research. I would like to also thank Dr. Youssef Hammi for helping in my model calibration efforts.

I would like to thank Dr. Brock Barry for his mentorship during my time at West Point and helping me get my "foot in the doorway" with this project. Dr. Led Klosky also served as a wonderful sounding board and mentor in geotechnical engineering for which I am grateful.

I would like to thank Dr. Wayne Hodo for his generous contribution of the legacy work of the late Dr. Don Smith that aided me greatly in my work. I am also thankful for his helpful suggestions throughout my research. In a similar vein, I would like to thank Mr. David Dumas for his invaluable expertise in helping me navigate the HPCMP at ERDC.

I would like to thank my leadership and all my colleagues in the Airfields and Pavements Branch at ERDC for their support and expertise throughout the duration of my research.

Dr. Carlos Gonzalez has been such an incredible mentor and teacher. I am grateful for his time and efforts in helping me work through various problems and teaching me the fundamentals of pavement engineering and FORTRAN.

I would like to thank my parents for their love and support. They taught me from an early age what it means to work towards a higher goal. I am so grateful for their constant encouragement. My desire to be a civil engineer has always been stimulated by my father, and my mother has always been one of my best friends. My sisters Koral and Karly have been an inspiration to me with all they have accomplished in their lives. I am so proud of them. I love you all very much.

I want to thank my lovely wife, Erin. You have been with me every step of the way and have burdened the responsibilities of homemaker, event planner, and travel agent. More importantly, you are truly my best friend and partner in crime. You are such a wonderful mother to our beautiful daughter, Bayley. "The heart of her husband trusts in her, and he will have no lack of gain. She does him good, and not harm, all the days of her life" (Proverbs 31:11-12). *I love you…so very much*.

Finally, to the Triune God, the Lord of all creation: "by the word of the Lord the heavens were made" (Psalm 33:6), he "upholds the universe by the word of his power" (Hebrews 1:3), and "in him all things hold together" (Colossians 1:17). All of life is created and sustained by your sovereignty and providence. *To you belongs all glory and honor in any endeavor – for thine is the kingdom, the power, and the glory forever*.

TABLE OF CONTENTS

LIST OF TABLES

LIST OF FIGURES

CHAPTER I

INTRODUCTION

1.1 Background

The United States military has deployed the AM2 landing mat system to austere locations around the world to construct expedient airfields since World War II. Airfield mats are emplaced when equipment and manpower are limited, logistics are challenging, and the quality of engineered materials are marginal (Gartrell, 2007). As a result, expedient airfields consisting of AM2 mat systems are typically constructed over soft existing subgrades, where rutting is the primary failure mechanism (Rushing and Tingle, 2007; Stache et al., 2019c). Properly addressing the issue of rutting requires uncovering the unique factors that contribute to the subgrade deformation response in the matting problem.

There are structural aspects of the AM2 mat that contribute to potential rutting failures. The AM2 landing mat consists of a single aluminum extrusion with hinge-type male-female connectors. The adjacent sides are joined by welded overlap-underlap connections secured with an aluminum locking bar. The load transfer mechanism in these joints lead to higher near surface stress and displacement responses in the subgrade. The mat panels are very thin at only 38.1 mm, thus providing noticeably less aircraft load distribution to the subgrade compared to conventional pavement structures. Furthermore, there is little bonding at the mat-soil interface in AM2 airfield structures. This leads to significantly higher rotations of the principal stresses near the surface compared to conventional pavement structures with fully bonded layer interface conditions.

Expedient airfields constructed with landing mats also see a variety of aircraft loads. For example, the F-15E Eagle fighter aircraft consists of a single wheel main gear with very high tire pressures, whereas the C-17A Globemaster III cargo aircraft consists of a multi-wheel main gear with a very large gross weight. In contrast to channelized traffic experienced on highways, these different loading conditions are exacerbated by the lateral wander of aircraft during taxiing, takeoff, and landing as it results in a kind of "kneading" of the supporting subgrade. The lateral wander of trafficking aircraft causes principal stress axes rotations and variations in the excess pore-water pressures, leading to a softening effect of the subgrade material.

Historically, the military has conducted extensive accelerated field testing of various landing mat systems. Testing of the AM2 goes back as far as the 1960s (e.g., Thompson and Burns, 1960; Burns and Fenwick, 1966; Ulery and Wolf, 1971) to more recent efforts in the Rapid Parking Ramp Expansion program (Rushing and Tingle, 2007; Rushing et al., 2008; Rushing and Mason, 2008; Garcia et al., 2014a, 2014b). While these field tests produced insights into subgrade behavior, the primary focus was on the performance and optimization of the mat itself. Numerical analyses of the AM2 mat system are significantly less prevalent (e.g., Foster, 2007; Leski et al., 2012; and Doyle et al., 2012). Foster (2007) and Leski et al. (2012) again focused only on mat performance, while Doyle et al. (2012) highlighted the vertical stress subgrade response under monotonic loading conditions.

This study investigates the multiple factors that contribute to subgrade rutting failures in AM2 airfield structures. A fully three-dimensional finite element (FE) model incorporating mat joint load transfer, the mat-soil interface bonding condition, and aircraft traffic wander is used to simulate the subgrade deformation response. The soft subgrade is modeled by implementing the

Multi-Mechanical Model (MMM), a user-defined elasto-plastic kinematic hardening model capable of modeling clays under repeated loadings and complex stress histories.

1.2 Objective

The objective of this work is to investigate the critical factors that contribute to subgrade rutting failures in landing mats constructed over soft subgrades. For this purpose, a kinematic hardening constitutive model capable of capturing complex stress histories is developed and calibrated. The constitutive model is implemented into a three-dimensional FE model of the AM2 mat system under static and pseudo-dynamic loadings to investigate the critical factors contributing to subgrade deformation response. Using this methodology, this work shows that the structural features of the AM2 mat system and the moving aircraft loads from traffic wander affect the subgrade deformation response and contribute to rutting failures in expedient airfield structures.

1.3 Scope and Organization of Dissertation

This dissertation is divided into five chapters. Chapter 1 provides an overview, main objective and scope of this research. Chapter 2 discusses the development, calibration, and testing of the Multi-Mechanical Model (MMM). While the field of soil constitutive modeling is rich, the availability of models that capture the behavior of different soil types under complex loading is limited. This chapter presents the development and validation of the MMM. The MMM is an elasto-plastic kinematic hardening model, which extends an earlier endochronic model by introducing the third stress invariant, accounts for shear-volumetric coupling in granular materials, and displays ratcheting behavior during stress reversals. A series of triaxial and isotropic consolidation tests are used to calibrate the MMM to materials found in

conventional unbound granular materials and subgrades, such as crushed limestone, Leighton Buzzard sand, and Vicksburg Buckshot clay. The MMM is tested against resilient modulus test data that present complex stress histories.

Chapter 3 investigates the critical factors affecting subgrade rutting failures in landing mats constructed over soft subgrades under static loading conditions. Subgrade rutting failures in matting structures present a unique challenge in expedient airfields. Mats are often constructed over existing soft subgrades and can experience aircraft with large gross loads and high tire pressures. It is important to understand and predict the critical factors that contribute to deformation in these thin structures. This chapter presents results of a comprehensive study on the critical factors contributing to rutting in the AM2 matting system under static loading, using a combination of full-scale instrumented testing, layered elastic analysis (LEA), and three-dimensional FE modeling. The FE model of the AM2 mat system is built by implementing the MMM as a user-defined material model in the commercial FE software *ABAQUS* to simulate the soft soil subgrade response. The results of the FE model are compared against those attained from a set of linear and nonlinear LEA and full-scale testing. The FE model is then used in a series of sensitivity studies to explicate the varying effects that factors such as loading conditions, subgrade cover material, mat joint load transfer, and mat-soil interface condition have on deformation response.

Chapter 4 looks at the effects of principal stress rotations and changes in excess pore-water pressure on subgrade deformation of landing mat structures under pseudo-dynamic loading. In addition to the rutting issues caused by landing mat construction over soft subgrades, the problem is accentuated by aircraft traffic wander. Mechanistic-empirical performance models are used to predict failures in various pavement structures, but this approach is typically confined

to static load computations. Two-dimensional axisymmetric FE models can simulate cyclic loading but are restricted to a single point of application. The main objective of this study is to properly investigate the soft subgrade deformation of the AM2 matting system under repeated, wandering aircraft traffic, which causes rotation of the principal stress axes and induces variations in excess pore-water pressures in the subgrade. For this purpose, we develop a full three-dimensional FE model that incorporates traffic wander using a pseudo-dynamic time-staggered series of tire imprints to represent a moving aircraft. The soft subgrade is modeled by implementing the MMM to capture the resulting principal stress rotations, excess pore-water pressure changes, and complex stress histories.

Chapter 5 provides the conclusions and recommendation for future works. The MMM was calibrated for Type 610 crushed limestone, Leighton Buzzard sand, and saturated Buckshot clay. Simulation results matched well with the shear stress, pore-water pressure, and volume change responses from conventional triaxial tests and the kinematic hardening behavior from a resilient modulus test. In a problem involving unique structural features in the AM2 mat and moving loads due to traffic wander, it was shown that the MMM was capable of capturing complex stress histories due to principal stress axes rotations. Research is still needed in laboratory and field testing to further validate the MMM in a 3D FE analysis. For example, reliable directional shear or cubical triaxial test data are needed to validate the MMM with respect to principal stress rotations. Furthermore, properly characterizing the load transfer mechanism at the AM2 mat joint and the bonding condition at the mat-soil interface require special laboratory and field testing for accurately simulating these phenomena in 3D FEA.

CHAPTER II

A KINEMATIC HARDENING MODEL BASED ON ENDOCHRONIC THEORY FOR COMPLEX STRESS HISTORIES

This chapter has been published as an article in the journal of Computers and Geotechnics (Stache, J., M., Peters, J. F., Hammi, Y., and, Vahedifard, F. (2019). "A Kinematic Hardening Model based on Endochronic Theory for Complex Stress Histories." Computers and Geotechnics, 114, 103117, DOI: 10.1016/j.compgeo.2019.103117). The paper has been reformatted and replicated herein with minor modifications in order to outfit the purposes of this dissertation.

2.1 Introduction and Background

Despite over 60 years of research effort, available constitutive models that accurately simulate behavior of soil, including volume change, under complex loading are still limited with respect to complex stress paths that include principal axes rotation and stress reversals. Important geotechnical engineering problems in which such models are needed include variations of principal stress axes occurring in the unbound layers and subgrade that result from the lateral distribution of traffic along runways, taxiways, and roads (Chan and Brown, 1994); earthquake engineering, particularly in situations where liquefaction is prevalent (Donaghe and Gilbert, 1983; Sadrekarimi, 2016); and settlement under vibrational loading (Issa et al., 1995). Further, a longstanding problem in constitutive behavior for soils is the response to rotation of principal stress axes (Arthur et al., 1980) that generally produces much greater plastic strain than predicted

by standard constitutive models available in commercial finite element programs. To be applicable to such problems, the constitutive model must respond to load variations, often referred to as kinematic hardening, including variations in principal stress orientations, and predict volumetric strains in response to load reversals.

Table 2.1 Review of soil constitutive models used for pavement applications

Model	**Nonlinear initial loading**	**Shear-dilatancy**	**Kinematic hardening**	**PSR**[8]	**Flow law**	**Conventional lab tests**
3-SKH [1]	yes	no	yes	no	non-associative	yes
Cyclic fuzzy set [2]	yes	yes	yes	no	non-associative	no
Hyperbolic [3]	yes	no	no	no	N/A	yes
Extended HiSS [4]	yes	no	yes[9]	no	non-associative	yes
Elasto-plastic shakedown[5]	yes	no	yes	no	non-associative	no
Permanent deformation [6]	yes	no	yes[9]	no	N/A	yes
Endochronic [7]	yes	yes	yes	yes	non-associative	yes

[1] Atkinson et al. (1990); McDowell and Hau (2003); McDowell and Hau (2004); Hau et al. (2005)
[2] Klisinski et al. (1987); Klisinski (1988); Ge and Chen (2012)
[3] Duncan and Chang (1970); Helwany et al. (1998)
[4] Bonaquist and Witczak (1997); Schwartz and Yau (2001)
[5] Habiballah and Chazallon (2005); Chazallon et al. (2006); Allou et al. (2007); Hornych et al. (2007)
[6] Wu et al. (2011)
[7] Valanis and Peters (1991); Issa et al. (1995)
[8] PSR = principal stress rotations
[9] The cyclic hardening behavior is modeled as a power function during any load cycle and the plastic strain
[10] Hysteresis loops are approximated by a series of linear loading and unloading paths using empirical transfer functions

A review of different constitutive soil models used for pavement applications is summarized in Table 2.1. An illustration is shown in Figure 2.1 of the effect a moving wheel load has over an element in a pavement structure. The complex loading conditions presented in pavement problems result in stress rotations that occur in both the direction of trafficking and the lateral distribution of the wheel loads with multiple passes. Modeling this phenomenon, along with the effects of kinematic hardening, contributes to an accurate accounting of plastic strain accumulation during repeated loading (Chan and Brown, 1994; Inam et al., 2012). Two other important aspects of a constitutive model are its theoretical transparency and its simplicity in calibration (Lade, 2005). The aim of any constitutive model then should be to achieve the balance between its straightforwardness and its ability to capture complex soil behavior. Lade (2005) reviewed a number of soil constitutive models to classify them in accordance with similar criteria as described above. While several models were chosen as the highest order classification, many of these were still wanting in critical categories, such as modeling both granular and fine-grained soils, non-associated flow, cyclic (kinematic) hardening, and simplicity in acquiring model parameters. In a similar vein, while all possessing unique features of their own, the chosen sample of constitutive models discussed in Table 2.1 also reveal limitations in successfully achieving this desired balance.

The principal motivation for the present study is improving pavement analysis under complex loading histories. The complexity of loading mechanisms in pavement problems require a constitutive model for the unbound granular layer and subgrade that can capture the nonlinear behavior during initial loading, shear-dilatancy in frictional materials, kinematic hardening as a result of repeated traffic, and variation of principal stresses due to traffic wander. A particular

class of plasticity model that can address these unique phenomena is based on the endochronic plasticity for frictional media.

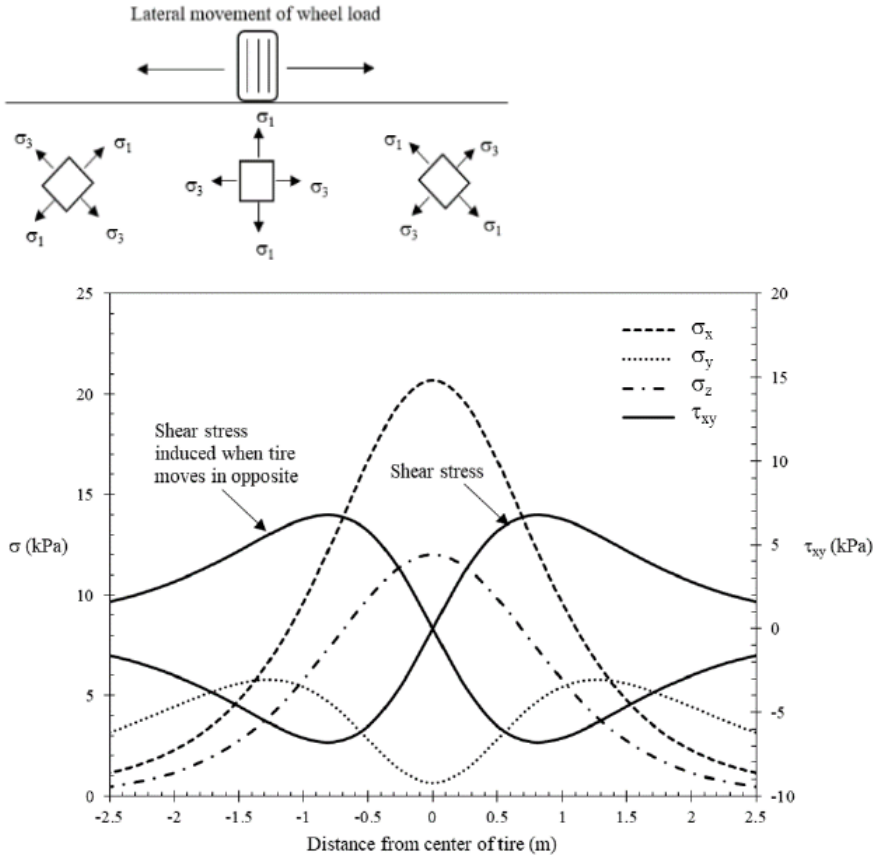

Figure 2.1 (Top) Variations in principal stresses as a result of the lateral distribution of a wheel load; (bottom) stresses induced by a moving wheel load over a vertically oriented element.

This paper presents the development of an elasto-plastic kinematic hardening model named the Multi-Mechanical Model (MMM) starting from its influences in the endochronic model formulated by Valanis and Peters (1988, 1991), and then presents an enhanced version of the MMM along with calibration and validation. This paper gives a complete description of the evolution from the Valanis and Peters (1988, 1991) model to the current MMM along with an

example analysis of progressive plastic straining under load cycles in what is commonly referred to as the resilient modulus test.

2.2 Endochronic Theory: Early Development and Recent Advances

Valanis (Valanis, 1971; Valanis and Read, 1980) initially developed the endochronic theory for metals. Valanis' motivation was to produce a theory for rate-independent materials (*i.e.*, plastic materials) that was as elegant and mathematically compact as those for viscoelastic materials. A shortcoming of the initial endochronic theory developed by Valanis (1971) was the implementation of increments of total strain to define the intrinsic time. Later, Valanis (Valanis and Read, 1980) modified his theory so the intrinsic time would be a function of increments of plastic strain. The formulation of an endochronic time measure is important for soils, where rate independent behavior is characteristic of granular materials. The endochronic theory was founded on the principles of thermodynamics that did not assume *a priori* equations for yield surfaces and flow rules characteristic of conventional plasticity. In particular, the theory naturally captured the hysteretic behavior produced by load cycles. Conventional yield surface plasticity was shown to be a derivable from the endochronic formalism (Valanis and Read, 1980).

Whereas the endochronic theory is similar to viscoelasticity as derived from internal state variable theory, the endochronic theory redefined the time parameter from the classic Newtonian measure to an *intrinsic* time measure. Instead of "clock" time measured in seconds, intrinsic time is measured with respect to plastic strain increments, making the time measure unique to each material. The endochronic theory soon became a "class" of models, with various modifications made by different researchers as applications varied from metals (e.g., Watanabe and Atluri, 1985; Hsu et al., 1991; Jain, 2012) to applications in concrete (e.g., Bazant and Bhat, 1976, 1977; Bazant and Shieh, 1980; Valanis and Read, 1986), powder forming processes (e.g., Khoei and

Jamali, 2005), the liquefaction of sands (e.g., Cuellar and Bazant, 1977; Bazant et al., 1983; Elizaroughi, 1978; Zienkiewicz et al., 1978; Blazquez et al., 1980; Bhatia and Nanthikesan, 1987), the shear-volume coupling phenomenon of granular soils (Valanis and Peters, 1988, 1991), and to rubber components (Baazer and Heining, 2015). While this demonstrates the widespread use of the model for different materials and loading conditions, the theory's ability to model the non-closure of hysteresis loops from repeated loading during kinematic hardening and represent the effect of the reversal of principal stress axis orientation make it a noteworthy candidate to model unbound granular layers and subgrade materials in airfield and highway pavement problems.

2.3 Fundamental Constitutive Equations of Valanis-Peters Model

2.3.1 Intrinsic Time-Based Stress Formulation

The development of the MMM stems from the Valanis-Peters (V-P) model (Valanis and Peters, 1988, 1991). Peters (1987) presented examples of the general capabilities for complex loading and calibration procedures that informed the development of the V-P model. Highlighting some fundamental constitutive equations for the V-P model may inform comparison and distinction from the MMM. The deviatoric and hydrostatic stresses are functions of their corresponding deviatoric and hydrostatic components of the Helmholtz free energy.

$$\boldsymbol{s} = \frac{\partial \psi_d}{\partial \boldsymbol{e}^p} \tag{2.1}$$

$$\sigma = \frac{\partial \psi_h}{\partial \boldsymbol{\varepsilon}^p} \tag{2.2}$$

where $\boldsymbol{s}$ and σ are the deviatoric and hydrostatic stresses and ψ_d and ψ_h are the free energies associated with the deviatoric and hydrostatic deformation respectively. The plastic strain $\boldsymbol{\varepsilon}^p$ has

been decomposed into deviatoric plastic strain $\boldsymbol{e}^p$ and hydrostatic plastic strain ε^p. The deviatoric and hydrostatic components of the free energy are functions of the plastic strains and the internal variables:

$$\psi_d = \frac{1}{2}\sum_{r=1}^{N^d} \boldsymbol{A}_r \, \|\boldsymbol{e}^p - \boldsymbol{q}^r\|^2 \tag{2.3}$$

$$\psi_h = \frac{1}{2}\sum_{r=1}^{N^h} B_r \, |\varepsilon^p - q^r|^2 \tag{2.4}$$

where the summation implies the free energies are distributed among N^d and N^h internal mechanisms acting in parallel. The strain-like internal variables for the deviatoric response $\boldsymbol{q}^r$ and the hydrostatic response q^r act in series with the individual elastic components parametrized by the elastic response parameters $\boldsymbol{A}_r$ and B_r. This form of free energy is similar in form to a generalized Maxwell model for a linear visco-elastic material, where the spring and dashpot are constructed in series with each spring-dashpot pair subjected to a common strain. In addition to the free energy, a dissipation relationship is required to define the evolution of the internal variables.

One of the unique features of endochronic theory is the introduction of a new definition of time. As opposed to the classic Newtonian definition of time, the intrinsic time measure is a function of the plastic strain. This distinguishes the endochronic dashpot from the classic viscoelastic dashpot, because it is driven by an intrinsic time common to all dashpots (Valanis and Peters, 1991). Whereas the equations are linear in terms of endochronic time, they inevitably produce a nonlinear stress-strain response. For isotropic materials, the intrinsic time dz common to all dashpots can be expressed in its deviatoric and hydrostatic components to read as follows:

$$dz^2 = \|d\boldsymbol{e}^p\|^2 + k^2|d\varepsilon^p|^2 \tag{2.5}$$

where the increment of plastic strain $d\boldsymbol{\varepsilon}^p$ has been decomposed into an increment of deviatoric plastic strain $d\boldsymbol{e}^p$, an increment of hydrostatic plastic strain $d\varepsilon^p$, and the two components are related by a coupling parameter *k*. Valanis and Peters discovered that by coupling the interaction of each internal hydrostatic mechanism with the *global* deviatoric deformation rather than at the mechanism level, volume change in unloading should correctly change from dilation to contraction (Valanis and Peters, 1991). The resulting stress-strain response that stems from this shear-volumetric coupling at the global level for deviatoric and hydrostatic components is as follows:

$$\boldsymbol{s} = \int_0^{z_d} \phi_d(z_d - z') \frac{d\boldsymbol{e}^p}{dz'} dz' \tag{2.6}$$

$$\sigma = \int_0^{z_h} \phi_h(z_h - z') \frac{d\varepsilon^p}{dz'} dz' + \int_0^{z_d} \Gamma(z_h - z') \boldsymbol{s} \frac{d\boldsymbol{e}^p}{dz'} dz' \tag{2.7}$$

where ϕ_d, ϕ_h, and Γ correspond to the deviatoric, hydrostatic, and shear-volume coupling kernel functions, respectively. The superscript ($'$) corresponds to the derivative of the intrinsic time, z. It is evident that the coupling of the shear and hydrostatic components in Equation (2.7) is mathematically complex and lacks some of the theoretical transparency and accessibility desired to anticipate and evaluate the model's performance (Lade, 2005).

2.3.2 Development of a Yield Surface and Shear-Dilatancy Law

The introduction of an intrinsic time naturally leads to a plasticity constitutive relationship. Specifically, for the V-P formulation, the yield surface is found to be a combined kinematic-isotropic hardening form

$$\|\boldsymbol{s}-\boldsymbol{Q}_s\|^2+\left(\frac{\phi_d^0 F_d}{k\phi_h^0 F_h}\right)\left[(\sigma-Q_h)-\frac{\Gamma_0}{\phi_d^0 F_d}\boldsymbol{s}\cdot(\boldsymbol{s}-\boldsymbol{Q}_s)\right]^2-(\phi_d^0 F_d)^2=0 \tag{2.8}$$

where $\boldsymbol{Q}_s$ and Q_h are the so called back stress quantities, for shear and hydrostatic loading respectively, determined from the loading history.

Another outcome of the V-P analysis was the role that stress-dilatancy played in the shear-volume coupling. It was shown that coupling the shear and hydrostatic components through shear-volume couplings at the level of the internal variables led to incorrect volumetric response upon reversals in loading directions. Rather, it appears from relating the theory to laboratory behavior that the shear-volume coupling must be invoked between the total shear and hydrostatic responses. In the appendix Valanis and Peters (1991) show that a general stress-dilatancy relationship results:

$$k\frac{d\varepsilon^p}{d\boldsymbol{e}^p}=\frac{1-\Gamma_0^2\frac{\boldsymbol{s}^2}{\sigma^2}}{\frac{\Gamma_0 F_h\boldsymbol{s}}{\sigma^2}\cos\psi+\sqrt{\frac{F_h^2}{\sigma^2}+\Gamma_0^2\frac{\boldsymbol{s}^2}{\sigma^2}-1}} \tag{2.9}$$

where dilatant behavior occurs if $\Gamma_0\frac{\boldsymbol{s}}{\sigma}>1$ and $\cos\psi=1$ implies loading occurs and $\cos\psi=-1$ implies unloading. The parameter Γ_0 can be determined from a plot of the volumetric and axial strain for a monotonic loading test, where Γ_0 corresponds to the ratio $\boldsymbol{s}/\sigma$ at the onset of dilation. The coupling parameter *k* can be calculated from Equation (2.9) by substituting the measured dilatancy rate $d\varepsilon^p/d\boldsymbol{e}^p$ (Valanis and Peters, 1991). As noted, this endochronic plasticity model with combined isotropic and kinematic hardening was developed without *a priori* rules to accommodate for the translation and expansion of the yield surface. Furthermore, the model distinguishes itself from critical state theory in that the plastic strain increments are not normal to

the derived yield surface, resulting in a non-associated flow (Valanis and Peters, 1991). Essentially, the introduction of the mean stress in the rate equations, from which the yield equations are derived, implies that the plastic strains cannot be normal to the yield surface. Houlsby (1981) previously arrived at a similar conclusion using a similar thermodynamically based approach. Ultimately the V-P model was implemented in a finite element analysis by Issa et al. (1995) to model cryogenic storage vessels containing perlite insulation, which was found from experiment to act similarly to sand.

2.4 Multi-Mechanical Model

As a historical note, the MMM is the result of internal research on the seismic response of large dams. The general requirements of the model had been laid out by Peters (1998), including isotropic and kinematic hardening and non-associative plasticity. The development of the original version of the MMM came as a result of users' difficulties in calibrating the V-P model and implementing it in general computer codes for solving practical problems. The MMM's design is based on a reinterpretation of the endochronic model for frictional materials with shear-volume coupling developed by Valanis and Peters (1988). Experience with the model for engineering practice revealed difficulties with practical applications because of its mathematical sophistication, stiffness of the kinematic hardening response (Peters, 1987) and difficulties implementing the model into finite element analysis (Issa et al., 1995). The MMM was subsequently applied to simple pavement loading sequences by Smith (2000) who implemented the model in an *ABAQUS* UMAT. Berney (2004) adopted the MMM as the basis for his research on partially saturated soil, in which significant contributions were made to calibrations procedures.

In this study, the MMM is updated from its original four mechanisms to six mechanisms to obtain an improved non-linear stress-strain response. Furthermore, while the V-P model used a secant stiffness approach and Smith (2000) implemented a finite difference approximation of the stiffness tensor only applicable for axisymmetric conditions, the MMM presented in this paper utilizes an initial stiffness approach applicable for three dimensional problems and foregoes the computation time of recalculating a new tangent stiffness matrix each time step. While powerful and robust, users experienced difficulties in calibrating the V-P model, consequently making it impractical for implementation in general computer codes for design. The model can be simplified both mathematically and operationally by introducing the idea of *autonomous time*, whereby the endochronic time is no longer common to all mechanisms; rather, each mechanism has its own time scale. The result is that each mechanism can be represented by a simple elastic-perfectly plastic response. Thus, the model reduces to several isotropic hardening models acting in parallel similar to the concept proposed by Nelson and Dorfmann (1995) of using a collection of different mathematical models acting in parallel to capture complex behaviors such as Baushinger's effect during stress reversals. The model retains the definition of free energy as outlined by Equations (2.3) and (2.4), and the separate deviatoric and hydrostatic mechanisms tied together by a stress dilatancy equation similar to Equation (2.9). A kinematic hardening yield law equivalent to Equation (2.8) is no longer necessary, although it is reflected in the action of the model.

The resulting "Multi-Mechanical" Model then is a mechanistic interpretation of Equations (2.1) – (2.7). The mechanisms comprising the shear and hydrostatic arrays are tied together in parallel as Maxwell arrays, sharing a common strain, as seen in Figure 2.2. Each mechanism is mathematically represented by an elastic spring and perfectly plastic slider.

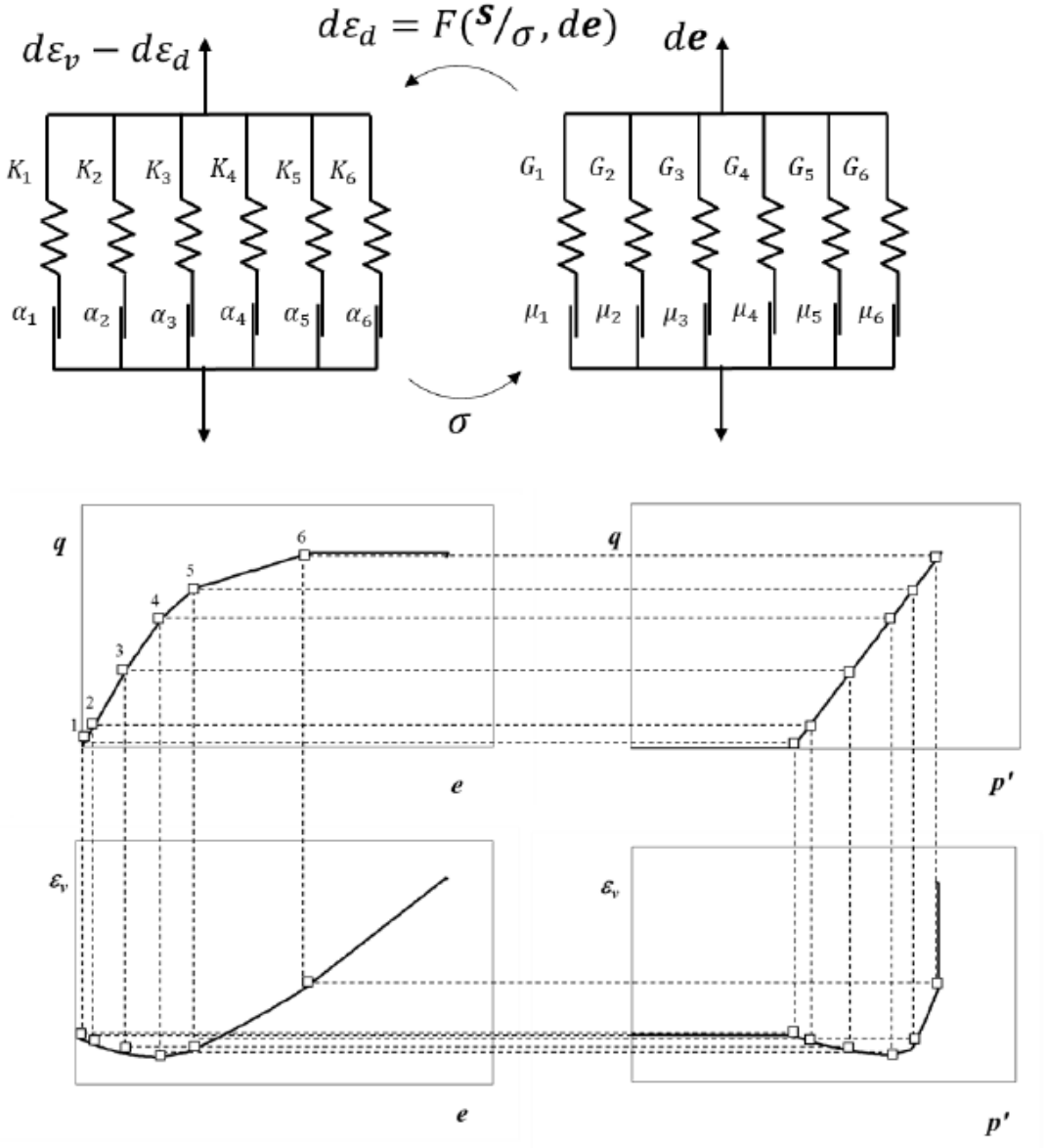

Figure 2.2 (Top) Maxwell representation of the MMM. The shear (right) and purely hydrostatic (left) mechanisms are coupled by a shear-dilatancy relationship. (Bottom) Notice each of the elastic-perfectly plastic mechanisms are engaged to form the shear and hydrostatic responses.

The elastic spring has both shear and hydrostatic components, where the behavior is characterized by the distribution of the shear and bulk moduli, respectively. The shear and

hydrostatic perfectly plastic components are characterized by the apportioning of the frictional strength and effective mean stress among the sliders making hydrostatic stress act like a parameter in the shear response.

Of course, the constitutive responses of shear and normal components are given by their own set of mechanisms. Fundamentally, to model volume change, it must first be computed at the *mechanism* level, where both the shear and hydrostatic mechanism responses are determined separately in accordance with their respective mechanism parameters. Similar to the V-P model, the complete volume change occurs as a result of a coupling of the purely hydrostatic and shear-induced dilatancy at the *global* level rather than the mechanism level as shown in Figure 2.2. Furthermore, the apportioning of the hydrostatic stress among the shear slider mechanisms causes a coupling that leads to ratcheting in the shear hysteresis under cyclic loading. This ratcheting has important implications to pavement applications and will be discussed in subsequent sections. A Matsuoka-Nakai yield law, for the shear response, and a hydrostatic compression-extension limit for the hydrostatic response, governs the plastic limit in the slider elements.

The Maxwell arrays are well suited for computation because they are strain driven. The calibration procedure is simplified by transforming the parallel Maxwell array of spring-slider mechanisms into an equivalent series Kelvin array where each mechanism shares a common stress, as can be seen in Figure 2.3. This enables for a non-iterative, stress-based calibration procedure for the mechanism parameters. As a result, although the sliders in each mechanism act in a perfectly plastic manner, both the Maxwell and Kelvin system of mechanisms are capable of modeling nonlinear stress-strain response, history effects, and kinematic hardening. This yields the concept of multiple nested yield surfaces within the model, where the MMM captures the

Baushinger's effect through unique definitions for compression and extension yielding and the evolution of the yield surface through ratcheting. The shear and hydrostatic responses are modeled independently and then coupled in a shear-dilatancy relationship similar to that found in critical state soil mechanics.

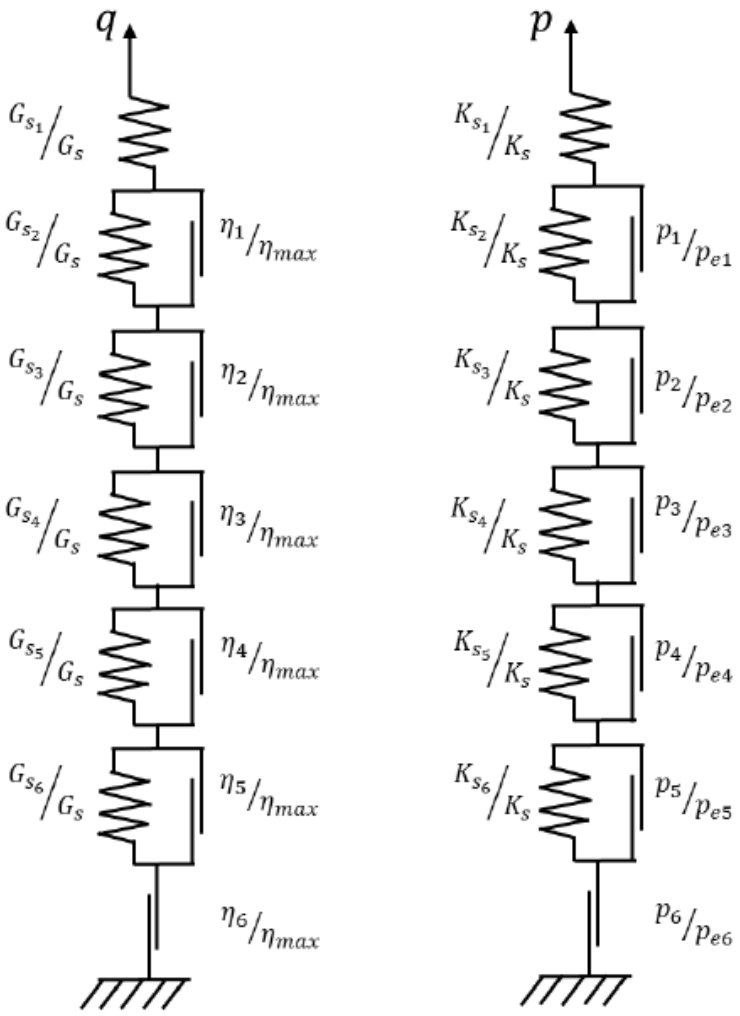

Figure 2.3 Kelvin representation of the MMM used in calibration. The shear (left) and hydrostatic (right) mechanism parameters are correspondingly transformed into series-related parameters. As a result of the transformation, each mechanism shares a common stress.

Similar to the V-P model, the stress-strain response must first be computed in the MMM at the mechanism level before the global volume change can be determined as a result of shear-volume coupling. Consequently, the MMM expresses the total intergranular stress $\boldsymbol{Q}^r$ at the mechanism level in terms of its deviatoric and hydrostatic components:

$$\boldsymbol{Q}^r = \boldsymbol{Q}_s^r + \alpha_r(\sigma + a) \tag{2.10}$$

where $\boldsymbol{Q}_s^r$ is the deviatoric shear stress for mechanism *r*, $(\sigma + a)$ is the hydrostatic stress component that consists of the sum of the total hydrostatic stress, σ, and the hydrostatic offset, a, which is a parameter adjusted from the cohesion in Mohr-Coulomb stress space. Also, α_r is a factor that distributes the hydrostatic stress seen by each mechanism *r*, where the hydrostatic stress for each mechanism, Q_h^r, is given by:

$$\sum_{r=1}^{n} Q_h^r = \sigma + a \tag{2.11}$$

2.4.1 Defining a Yield Criterion

The limit states for the hydrostatic and shear yield surfaces for each mechanism is apportioned from the total strength defined by the global parameters, where the total strength envelope is curved when viewed in a Hvorslev plot (Figure 2.4). This curvature is then passed to the individual mechanism yield surfaces, the magnitude of which are governed by the mechanism parameters.

The shear and hydrostatic mechanisms act separately with the introduction of an autonomous time and then are coupled by a shear-dilatancy law. The yielding of the hydrostatic stress mechanism in Equation (2.11) is governed by a function of the reference stress at the

prevailing void ratio, determined from the $e - logp'$ curve of a one-dimensional consolidation test. The hydrostatic mechanisms are governed by the following yield law:

$$Q_h^r = H^r P_e(e) \tag{2.12}$$

where P_e is the reference stress as a function of the void ratio, and the parameter H^r determines the yield of the hydrostatic mechanisms, checking whether or not the compression or tension limits have been reached, and is unique to each mechanism forming the stress-strain response.

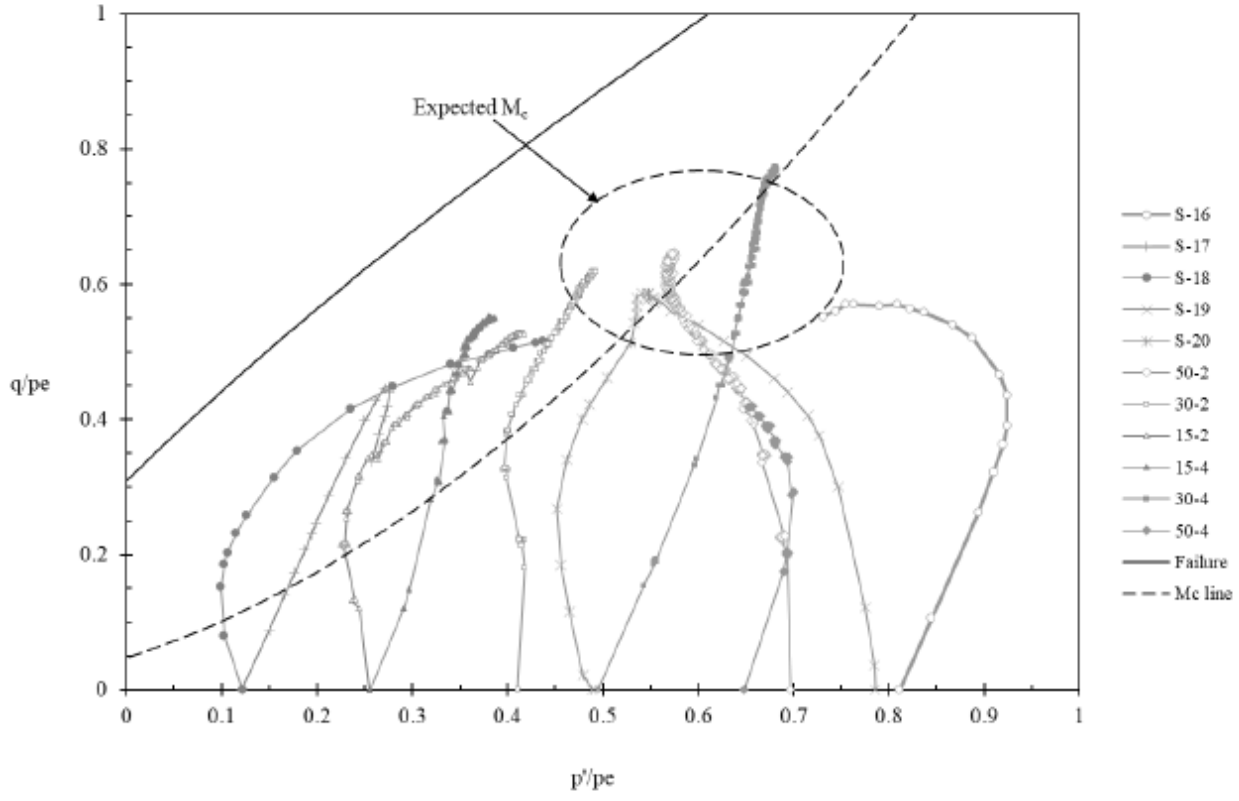

Figure 2.4 Normalized stress paths for VBC in triaxial CU tests, displaying the solid failure envelope, the dotted M_c line, and the expected location of the critical state (Berney 2004).

While theoretically the MMM could incorporate an infinite number of mechanisms in forming the response during initial loading, six elastic-plastic mechanisms were used in the work reported here, with each mechanism containing its own material properties and autonomous intrinsic time measure. Each mechanism is composed of an elastic spring and a plastic slider, governed by the yield criteria set forth by the Matsuoka-Nakai (1974) yield surface, which matches the points of triaxial compression and extension with the Mohr-Coulomb hexagonal surface in three-dimensional stress space. Using the yield surface in lieu of a dissipation relationship simplifies introduction of the third invariant into the constitutive model. The yield law is given by:

$$f(\boldsymbol{Q}^r) = \frac{I_1^r I_2^r}{I_3^r} \tag{2.13}$$

where I_1^r, I_2^r, and I_3^r are the invariant representations of the intergranular mechanism stress $\boldsymbol{Q^r}$. The stress invariants are defined with respect to the principal stresses as:

$$I_1^r = Q_1^r + Q_2^r + Q_3^r \tag{2.14}$$

$$I_2^r = Q_1^r Q_2^r + Q_2^r Q_3^r + Q_1^r Q_3^r - \left(Q_4^{r\,2} + Q_5^{r\,2} + Q_6^{r\,2}\right) \tag{2.15}$$

$$I_3^r = Q_1^r Q_2^r Q_3^r - Q_1^r Q_6^{r\,2} - Q_2^r Q_5^{r\,2} - Q_3^r Q_4^{r\,2} + 2Q_4^r Q_5^r Q_6^r \tag{2.16}$$

The yield law governs the use of the radial return-mapping algorithm, which employs an elastic predictor – plastic corrector approach when ensuring the current state of stress remains on or within the yield surface.

2.4.2 Shear-Dilatant Behavior

In critical state soil mechanics, the shear and volumetric strains are coupled together using a power equation, given by:

$$\boldsymbol{s} \cdot d\boldsymbol{e}^p + \sigma d\varepsilon_v = \sigma M_c d\boldsymbol{e}^p \tag{2.17}$$

where $\boldsymbol{s}$ is the deviatoric stress**,** $d\varepsilon_v$ is the increment of volumetric strain, and M_c is the critical state coupling parameter which represents the ratio of the deviatoric stress to effective mean stress at critical state $(q/p')_{crit}$. This equation is helpful in relating volume changes during shearing, but its application is typically restricted to the particular case of $d\boldsymbol{e}^p \neq 0$ (Valanis and Peters, 1988) and $d\varepsilon_v > 0$ and is only applicable during monotonic loading (Schofield and Wroth, 1968). It was shown in the V-P model that shear-volume coupling cannot be done at the mechanism level but with the *total* deviatoric and hydrostatic responses. Consequently, the total shear and hydrostatic responses in the MMM are coupled by the shear-dilatancy law M_c, as shown below:

$$\gamma \boldsymbol{s} \cdot d\boldsymbol{e}^p + \sigma d\varepsilon_d = \gamma M_c \sigma \sqrt{d\boldsymbol{e}^p \cdot d\boldsymbol{e}^p} \tag{2.18}$$

where γ is a dilatancy scaling parameter that modulates the effect of the shear-volume coupling and $d\varepsilon_d$ is the increment of hydrostatic strain resulting from the shear-volume coupling. As opposed to the Cam-Clay shear-dilatancy model, the resulting formulation distinguishes pure hydrostatic volume changes from shear-induced volume changes. Also, while Equation (2.17) requires positive volume changes during unidirectional loading, Equation (2.18) senses the direction of shear loading and correctly predicts the magnitude and direction of the volumetric strain during unloading. During unidirectional loading the soil goes through contraction then

dilation as the stress ratio exceeds the constant volume value. Equation (2.18) also captures the contraction that occurs upon unloading, a key feature of the V-P theory.

2.5 Calibration

2.5.1 Overview of Calibration Procedure

The calibration procedure for the proposed multi-mechanical model is straightforward and transparent. The parameters required to calibrate the MMM can be obtained from standard laboratory tests. The model is separated into global components derived from common soil mechanics concepts associated with strength, stress-dilatancy, and consolidation and response functions that control the shape of the stress-strain response. This dichotomy is similar to that used in the original endochronic model. In some respects the simplified nature of the proposed model provides for improvements in model capability. In particular, the sliders in the MMM are governed by yield laws that enable the introduction of the third invariant, which was not a part of the original V-P model. While providing an overview of the calibration procedure, further insight of how the global and mechanism parameters are used in the MMM will also be discussed.

The first ten parameters are considered global and can be directly extracted from conventional laboratory test data – *i.e.*, conventional triaxial compression tests and isotropic consolidation tests. Using the isotropic consolidation test's $e - logp'$ plot, the compression index is found by finding the slope of the normal consolidation line, while the hydrostatic intercept is identified where p' = 6.895 kPa. The cohesion and friction angle are Mohr-Coulomb parameters from triaxial data, whereas the shear and bulk elastic moduli are determined from the deviatoric stress-strain plot from triaxial compression tests and the effective mean stress-volumetric strain plot from isotropic consolidation tests, respectively. These global parameters describe the total strength envelope but are then apportioned to each mechanism to define the

individual limit states. The coupling parameter M_c and the friction ratio ϕ_{ratio} are critical state parameters determined from normalized stress path plots from triaxial test data. The coupling parameter represents the ratio of the deviator stress and mean effective stress at critical state, whereas the ϕ_{ratio} is the ratio of the minimum and maximum angles of the failure surface on the normalized stress path plot defined in Figure 2.4 and typically is concave downward. The M_c line is typically concaving upward and changes with the dilatancy angle ψ, as shown in Figure 2.4 and Equation (2.19) below:

$$M_c = \frac{6 \sin \psi}{3 - \sin \psi} \tag{2.19}$$

The dilatancy parameter γ is determined from a plot of the volumetric strain against axial strain from triaxial test data, since it scales the effects of shear-induced volume change. Finally, the decay parameter controls the curvature of the strength envelope in a normalized Hvorslev plot from Figure 2.4 to ensure it captures the critical state response from the stress paths by adjusting the friction angle for each mechanism ϕ_r, as shown in Equation (2.20):

$$\phi_r = \phi(r)\left\{\phi_{ratio} + (1 - \phi_{ratio})e^{(d\frac{p\prime}{P_e})}\right\} \tag{2.20}$$

Equation (2.20) includes both global and mechanism parameters, including: $\phi(r)$, which is the product of the global friction angle and the mechanism strength factor parameter μ_r; ϕ_{ratio}, described above is used to distribute p' to the shear mechanisms by coupling it with the friction, and *d*, which scales the curvature of the strength envelope defining the yield law. The strength factor μ_r and the mean stress factor α_r describe the strength mobilized by the friction angle and the mean stress seen by each plastic slider, respectively. As the shear stress is updated for each mechanism, the effective mean stress seen by each hydrostatic mechanism is then scaled

by the mean stress factor α_r as shown in Equation (2.10) and used to update the predictor stress. The yield law as a function of Equation (2.20) governs the predictor stress and maps a plastic corrector back to the yield surface if necessary. The overall effect achieved by these parameters is the distribution of the effective mean stress to the shear mechanisms. Furthermore, the introduction of these parameters in the MMM enables the inclusion of the third stress invariant – another important distinction from the V-P model.

With respect to the elastic response, two mechanism parameters are used to distribute the elastic stiffness to each mechanism. The shear ratio G_{ratio} is the ratio of the shear stiffness distributed to each spring mechanism in accordance with the points defined by the user from the triaxial deviator stress-strain plot with respect to the global shear modulus. The bulk ratio K_{ratio} is the ratio of the volumetric stiffness distributed to each spring mechanism in accordance with the points defined by the user from the isotropic consolidation $e - logp'$ plot with respect to the global bulk modulus. The compression limit H^r is the ratio of the individual mean stress for each mechanism defined by the user from the $e - logp'$ plot with respect to the reference stress P_e. Consequently, the mechanism parameters govern the distribution of the global parameters that form the total strength envelope and apportion them to define the different limit states of each shear and hydrostatic mechanism.

Figure 2.5 illustrates the history effects by tracking the stress paths taken by each mechanism during initial loading, unload, and reload. Each mechanism is governed by its own limit states. The stress-strain response is shown in the first plot. In the second plot the stress path for the cyclic load shows the total response follows the straight line that is typical of a drained triaxial test. The remaining six plots show the stress path taken by each mechanism. The stress path for each mechanism follows a loop rather than a straight line as a result of the individual

limit states for each mechanism. In the case of mechanism 5 the mechanism barely reaches the limit state, hence the stress path for that mechanism is nearly a straight line.

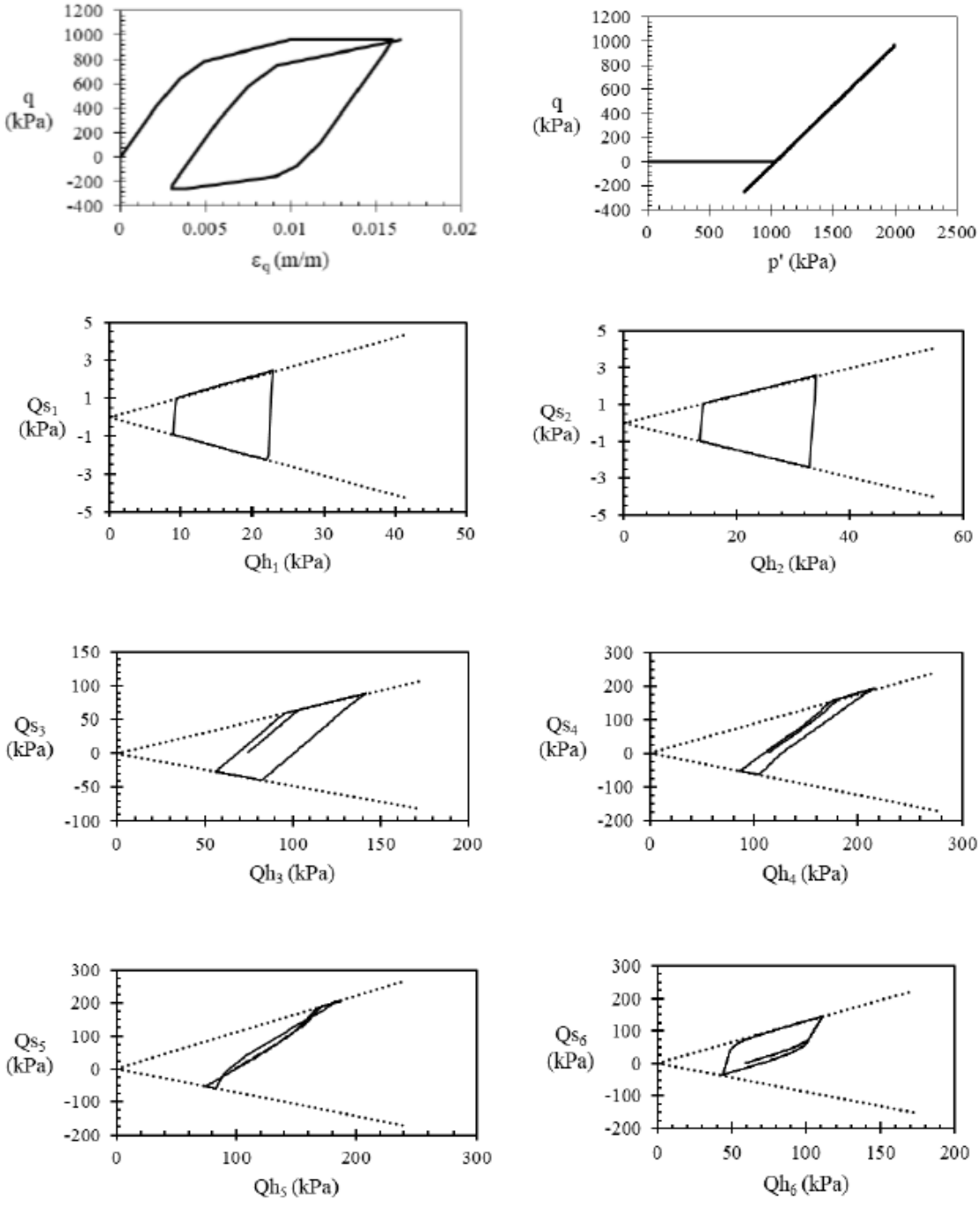

Figure 2.5 History effects from state dependence in MMM. (Top row) shear response where hysteresis loop nearly closes and corresponding stress path for load, unload, and reload; (2^{nd}-4^{th} rows) shear mechanism Qs(r) stress paths versus effective mean stress adjusted by α_r.

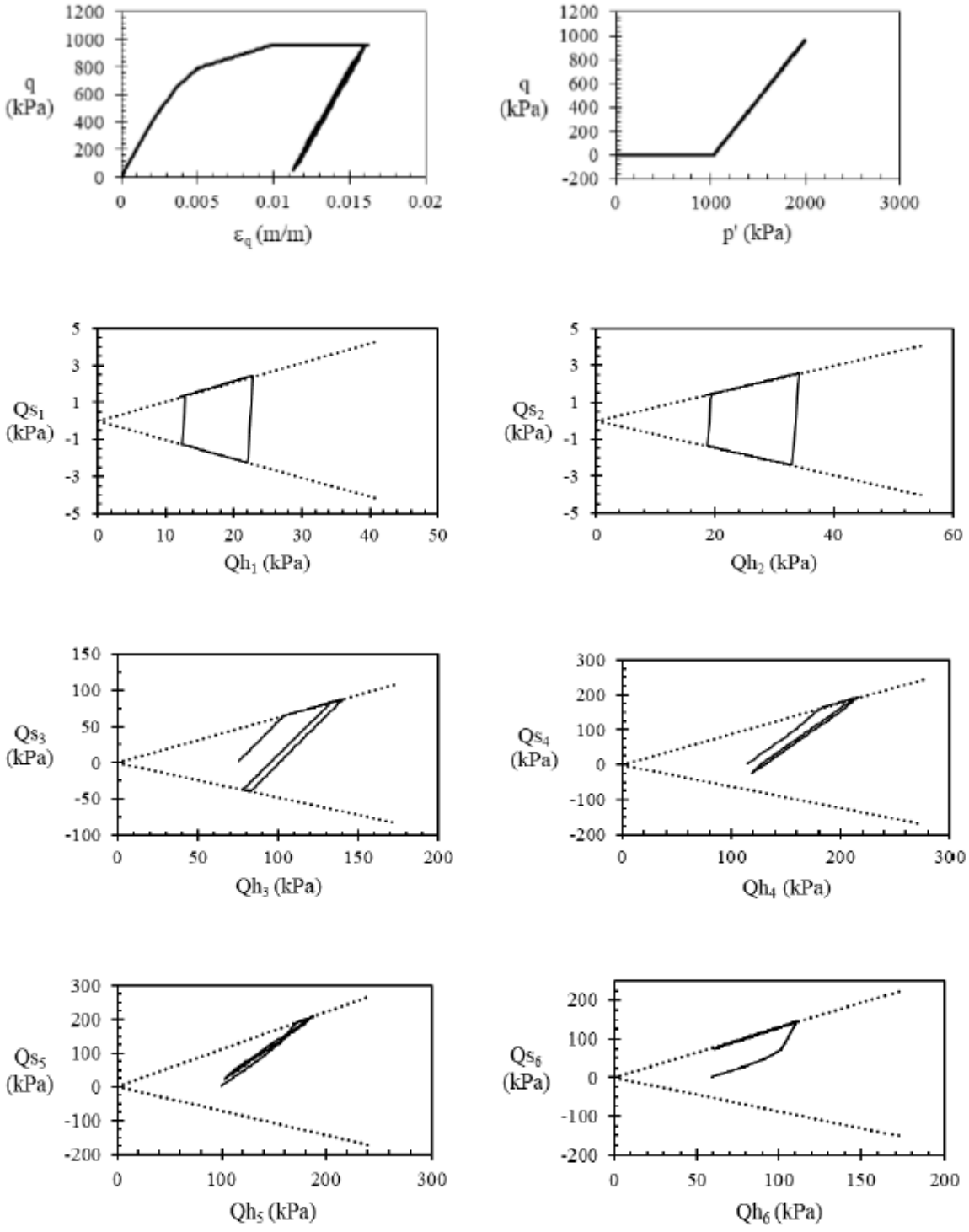

Figure 2.6 History effects from state dependence in MMM. (Top row) shear response where ratcheting occurs and corresponding stress path; (2^{nd}-4^{th} rows) shear mechanism Qs(r) stress paths versus effective mean stress adjusted by α_r.

Also note that the stress path loops do not always close as can be seen for mechanism 3. Whether a mechanism reaches a limit state depends on the distribution of shear stiffness among the mechanisms, the distribution of limit state, and the distribution of mean stress. Thus, the ratcheting that results during a resilient modulus test is controlled by several parameters implying that calibrations producing the same stress-strain response to monotonic loading tests could produce different degrees of ratcheting under cyclic loading. For example, notice Figure 2.5 is for a cycle that goes from fully yielded in compression to nearly yielded in extension and back. Thus the hysteresis loop nearly closes. On the other hand, Figure 2.6 shows the first stress reversal leg of the resilient modulus test simulated later in the paper where ratcheting is occurring. While the first two mechanism stress paths reach their individual limit states, mechanism 3 does not travel along the extension yield surface as long, and the subsequent mechanisms never reach their respective extension limit states. As a result, the hysteresis loop on the first stress reversal leg does not close and ratcheting occurs, as will be discussed later in the simulation of the resilient modulus test.

At the user level, the calibration procedure of the mechanism parameters consists in defining points along the deviatoric stress-strain plots from triaxial compression tests and $e - logp'$ plots from isotropic consolidation tests that correspond to the number of mechanisms. For calibration, the Maxwell configuration for the elastic-perfectly plastic mechanisms is converted to a Kelvin configuration. For the Kelvin configuration, each spring-slider pair is in series such that all mechanisms have the same common stress, making the fit to stress-strain curves relatively simple. Given the parameters for the Kelvin configuration, the corresponding parameters for the Maxwell series model are obtained through straightforward algebraic

manipulation. This procedure thus enables users to quickly and easily calibrate the model with the requisite conventional laboratory data.

2.5.2 Laboratory Data Used For Calibrating Model Parameters

There are three different materials calibrated in this investigation to the MMM, under three different loading conditions. The first set of laboratory test data are from Berney (2004) on Vicksburg Buckshot clay (VBC). The two primary tests from this testing program used in this paper are the consolidated undrained (CU) triaxial compression tests on saturated specimens with pore pressure measurements (ASTM D 4767), as well as isotropic consolidation test run in conjunction with the CU triaxial tests (ASTM D 2435). A series of tests were run at 103 kPa, 207 kPa, and 345 kPa confining pressures on Standard energy Proctor samples (Berney, 2004). It should be noted that the formation of slickensided shear banding in the VBC specimens invalidated some of the tests for strains beyond shear-band initiation.

The second set of laboratory test data are from Al-Aghbari and Mohamedzein (2004) on Leighton Buzzard sand (LBS). Al-Aghbari and Mohamedzein conducted conventional triaxial compression tests on LBS at 40 kPa, 100 kPa, and 150 kPa where both shear response and volume change were recorded. Finally, the third set of laboratory test data are from Smith (2000) on crushed limestone type 610 (CL610). This testing program implemented conventional triaxial compression tests at 207 kPa, 345 kPa, and 552 kPa, and a resilient modulus test at 345 kPa. Of particular interest is simulating variations in the principal stresses and the ratcheting effect resulting from the kinematic hardening during stress reversals. Descriptions for the global and mechanism properties are given in Table 2.2 and Table 2.3, respectively. All the global and mechanism parameters for the three different soil types are shown in Table 2.4 and Table 2.5, respectively.

Table 2.2 Global material properties of the Multi-Mechanical Model

Parameter	**Symbol**	**Description**
Compression index	β	Reciprocal of Cc on the NCL
Hydrostatic intercept	e_{ncl}	Intercept of the NCL on *e*-log*p'* plot
Cohesion	c	Mohr-Coulomb cohesion parameter
Shear-volume factor	Mc	Coupling parameter for shear-induced volume changes
Dilatancy scaling factor	γ	Reduces the effects of dilatancy during shearing
Friction angle	ϕ	Mohr-Coulomb friction angle
Decay	d	Controls rate of frictional strength reduction with over consolidation
Friction ratio	ϕ_{ratio}	Ratio of max and min angles of
Bulk modulus	K	Elastic bulk modulus
Shear modulus	G	Elastic shear modulus

Table 2.3 Mechanism parameters of the Multi-Mechanical Model

Parameter	**Symbol**	**Description**
Strength factor	μ_r	Scales frictional strength seen by each plastic slider
Mean stress factor	α_r	Scales mean stress seen by each plastic slider
Shear stiffness factor	G_{ratio}	Distributes the shear stiffness across springs
Compression limit	H^r	Compression limit for hydrostatic yield law
Volumetric stiffness factor	K_{ratio}	Distributes the volumetric stiffness across springs

Table 2.4 Calibrated global model parameters for different soil types

Parameter	**VBC**	**LBS**	**CL610**
β	3.757	115.21	8.685
e_{ncl}	1.4	1.05	0.7
c	86.2 kPa	0.69 kPa	1.72 kPa
Mc	1.0	1.3	0.72
γ	0.015	0.85	1.0
ϕ	11.5 degrees	29 degrees	48 degrees
d	1.5	1.5	1.8
ϕ_{ratio}	0.619	0.5	0.5
K	38956 kPa	66880 kPa	68948 kPa
G	29213 kPa	42058 kPa	179263 kPa

Table 2.5 Calibrated mechanism parameters for different soil types, where each column represents the parameters associated with a particular spring-slider mechanism

Leighton Buzzard Sand						
Parameter	1	2	3	4	5	6
μ_r	0.67548	0.70059	0.74207	0.74904	0.80354	1.00000
α_r	0.75501	0.72968	0.55954	0.20109	0.10484	0.08572
G_{ratio}	0.59333	0.22472	0.09692	0.04505	0.02894	0.00821
K_{ratio}	0.72490	0.09629	0.09560	0.00052	0.02227	0.01286
H^r	0.68700	0.78760	0.89330	0.89390	0.92000	0.93550
Crushed Limestone Type 610						
Parameter	1	2	3	4	5	6
μ_r	0.69807	0.57015	0.60656	0.56746	0.83400	1.00000
α_r	0.70408	0.60218	0.65109	0.53867	0.27954	0.14887
G_{ratio}	0.43263	0.08383	0.02486	0.06684	0.02770	0.04643
K_{ratio}	0.57131	0.10293	0.03998	0.02319	0.02379	0.02438
H^r	0.43700	0.64600	0.67600	0.70000	0.72400	0.75000
Vicksburg Buckshot Clay						
Parameter	1	2	3	4	5	6
μ_r	0.44336	0.48118	0.66653	0.70206	0.87370	1.00000
α_r	0.62550	0.27681	0.10924	0.21151	0.09600	0.20173
G_{ratio}	0.57764	0.19639	0.08254	0.03556	0.01165	0.01971
K_{ratio}	0.30400	0.17500	0.19900	0.11100	0.10100	0.00600
H^r	0.15990	0.36472	0.55459	0.69153	0.90460	0.95460

2.5.2.1 Vicksburg Buckshot Clay

The VBC specimens were fully saturated, sheared under undrained conditions and thus required prediction of pore pressure generated during shear. An additional feature was incorporated into the model to account for these short-term effects. First, to couple pore pressure response with the updates to total stress, a simple subroutine was added to update the pore pressure each load step as a function of the Skempton pore pressure parameter *B*, where $B = 0.98$ for saturated conditions. Furthermore, the undrained and drained bulk moduli were summed at each increment in the update of the elasticity tensor.

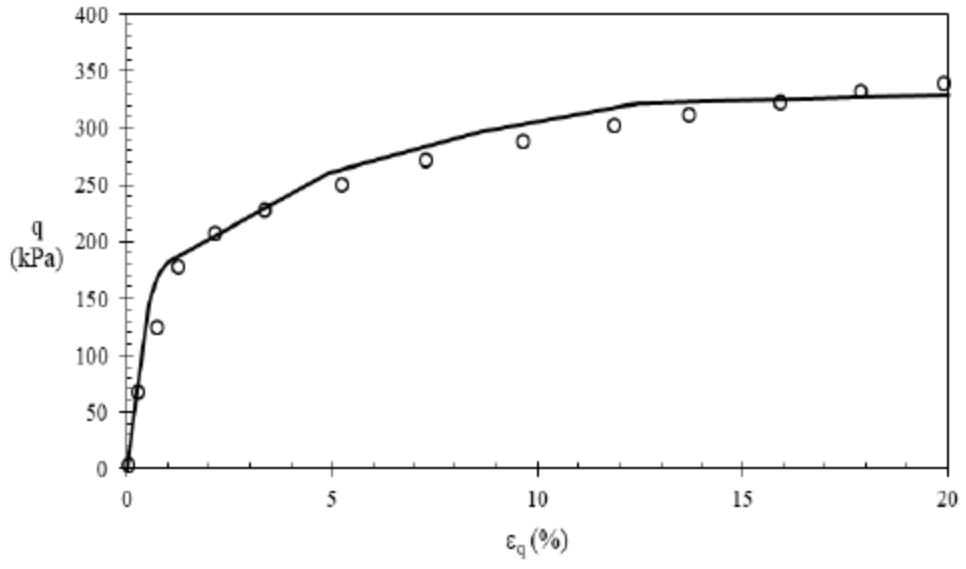

(a)

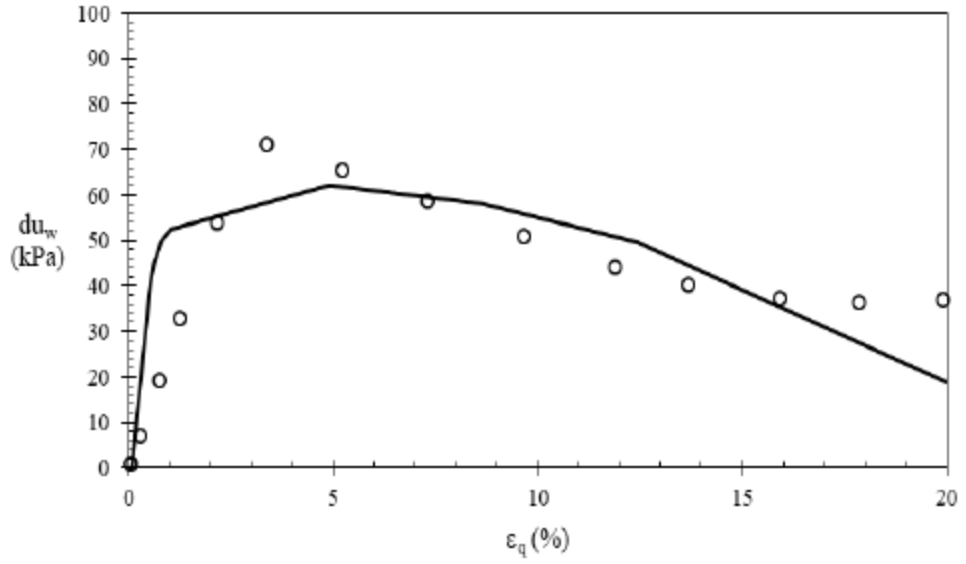

(b)

Figure 2.7 The calibration results for (a) the deviator shear and the (b) excess pore pressure test data for VBC at 345 kPa, where the solid line represents the model and the points are test data.

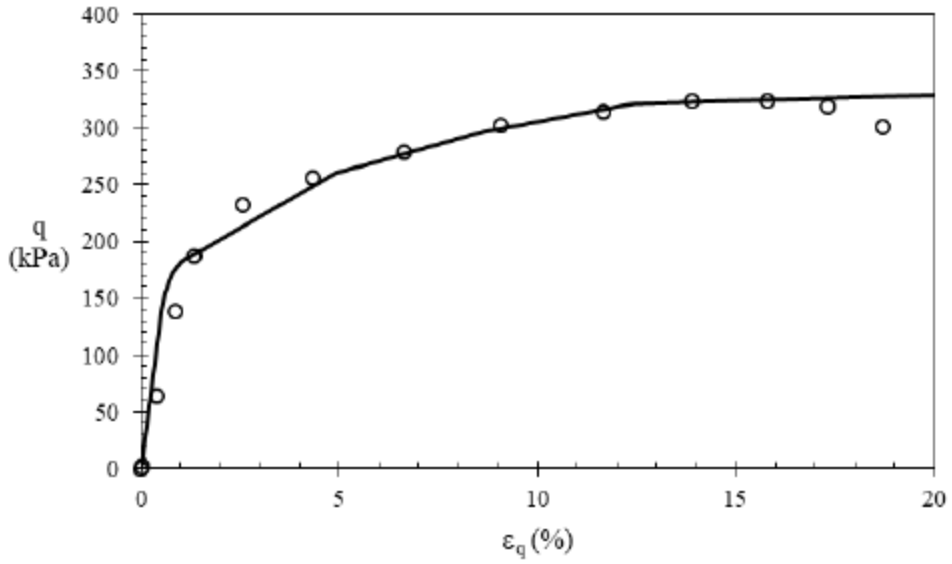

(a)

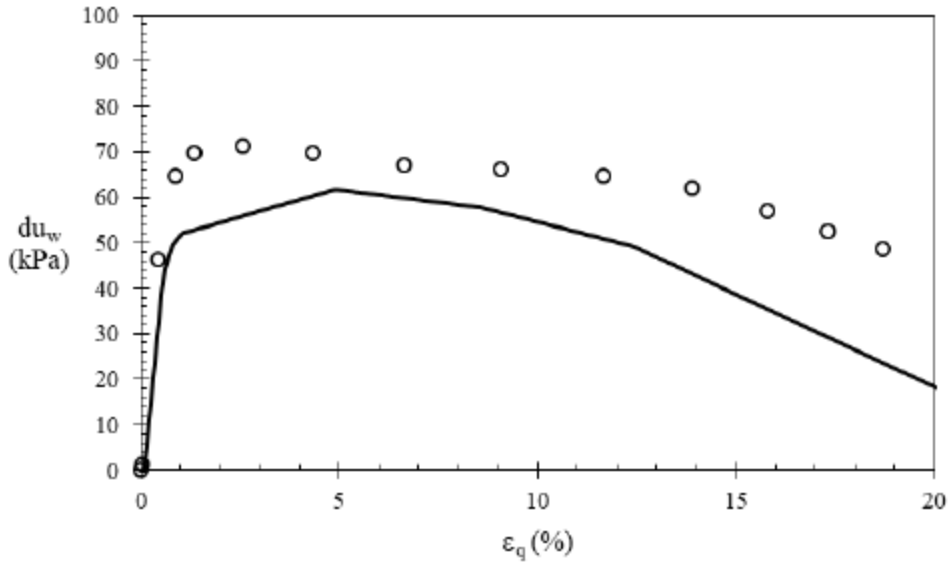

(b)

Figure 2.8 The testing results for (a) the deviator shear and the (b) excess pore pressure test data for VBC at 207 kPa, where the solid line represents the model and the points are test data.

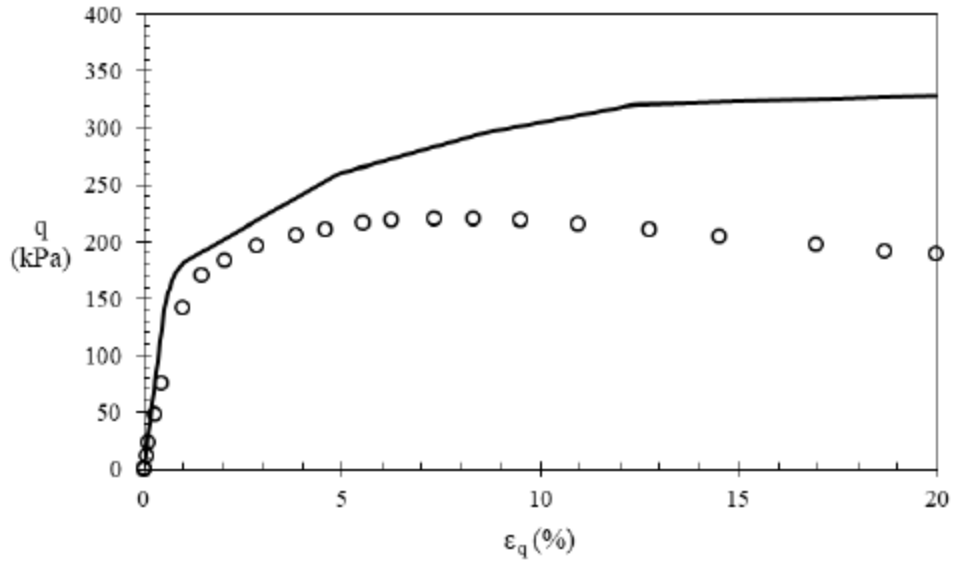

(a)

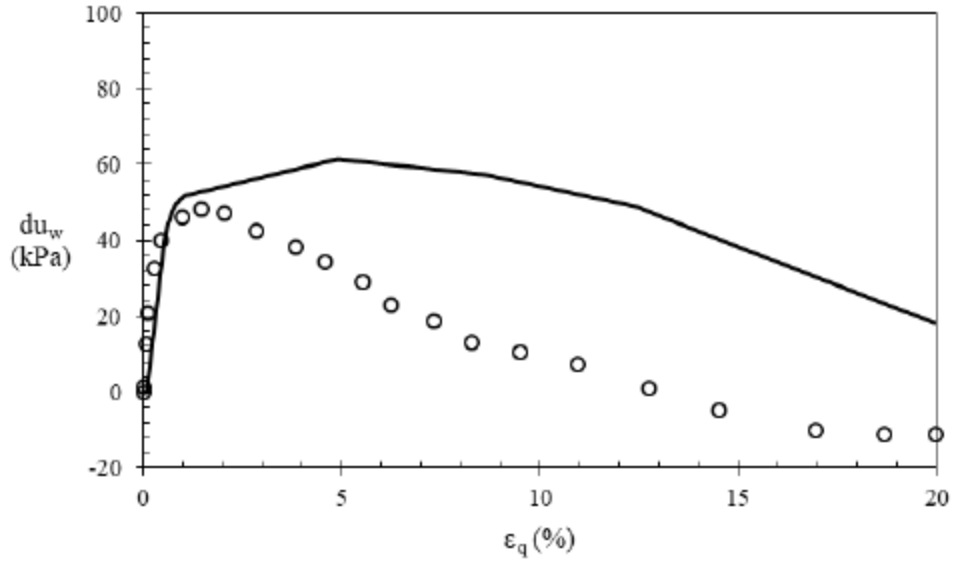

(b)

Figure 2.9 The testing results for (a) the deviator shear and the (b) excess pore pressure test data for VBC at 103 kPa, where the solid line represents the model and the points are test data.

Another feature which is absent from Smith (2000), but was added to Berney (2004) is accounting for the curvature of the M_c line for different materials. The M_c line is a function of the dilatancy curvature parameter ψ, defined by Equation (2.21):

$$\psi = \psi_{max} + (\psi_{min} - \psi_{max})e^{(-d_v\frac{p'}{p_e}+c)} \tag{2.21}$$

where the decay parameter d_v controls the curvature of the M_c line, as opposed to the decay parameter d in Equation (2.19) that controls the curvature of the failure envelope on the Hvorslev plot. Similar to ϕ_{max} and ϕ_{min}, the dilatancy angle parameters ψ_{max} and ψ_{min} are determined from Hvorslev plot of the M_c line. The results of the model calibration against the 345 kPa test data are shown in Figure 2.7.

The MMM was then tested at the remaining two confining pressures to ensure the extracted parameters captured the requisite behavior. Figure 2.8 and Figure 2.9 show the testing results for 103 kPa and 207 kPa confining pressures. While the model predicts the undrained shear response for the higher two confining pressures, along with reasonable estimates of the excess pore water pressure response under saturated conditions, the model has a stiffer shear response than the test data at the lowest confining pressure.

2.5.2.2 Leighton Buzzard Sand

The LBS was first calibrated to the triaxial compression data provided by Al-Aghbari and Mohamedzein (2004). The model was first calibrated to the 40 kPa test data. The two sets of test data consisted in shear and volumetric responses. The results for the calibration are shown in Figure 2.10. The calibrated model was then tested against the remaining two confining pressures.

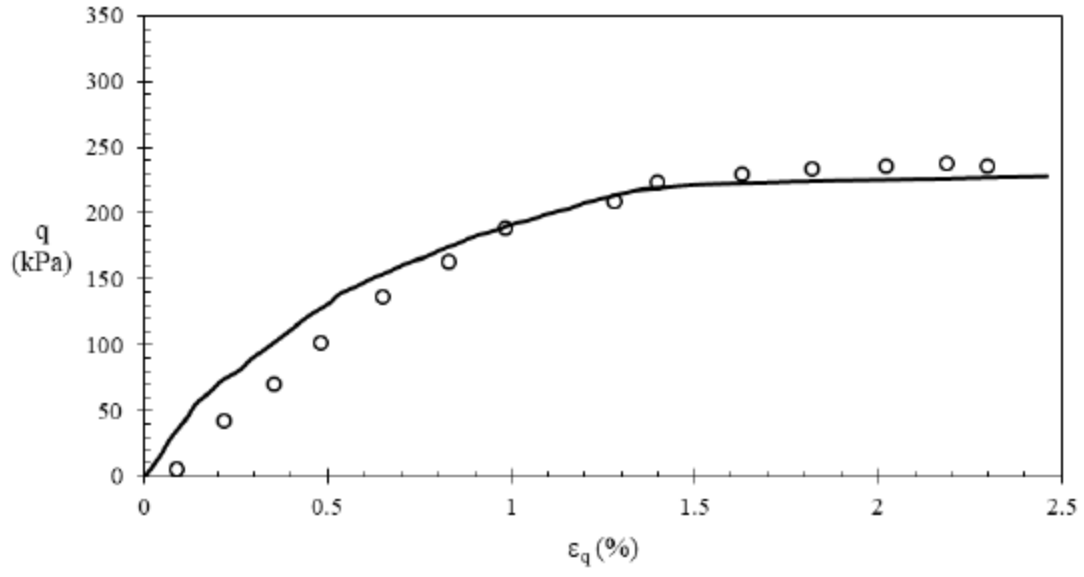

(a)

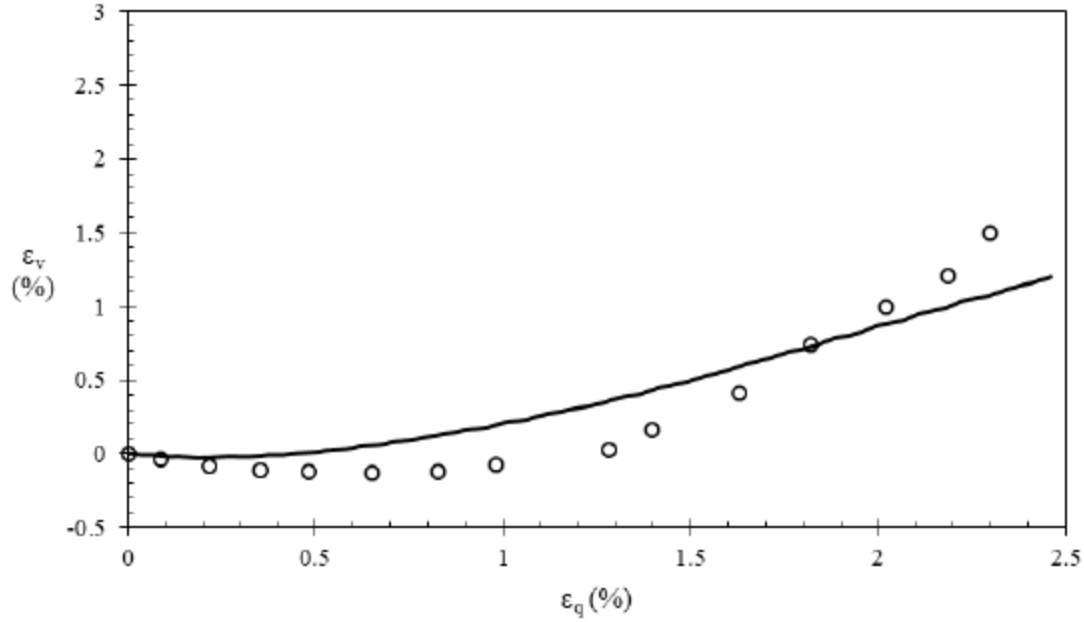

(b)

Figure 2.10 The calibration results for (a) the deviator shear and the (b) volumetric strain test data for LBS at 40 kPa, where the solid line represents the model and the points are test data.

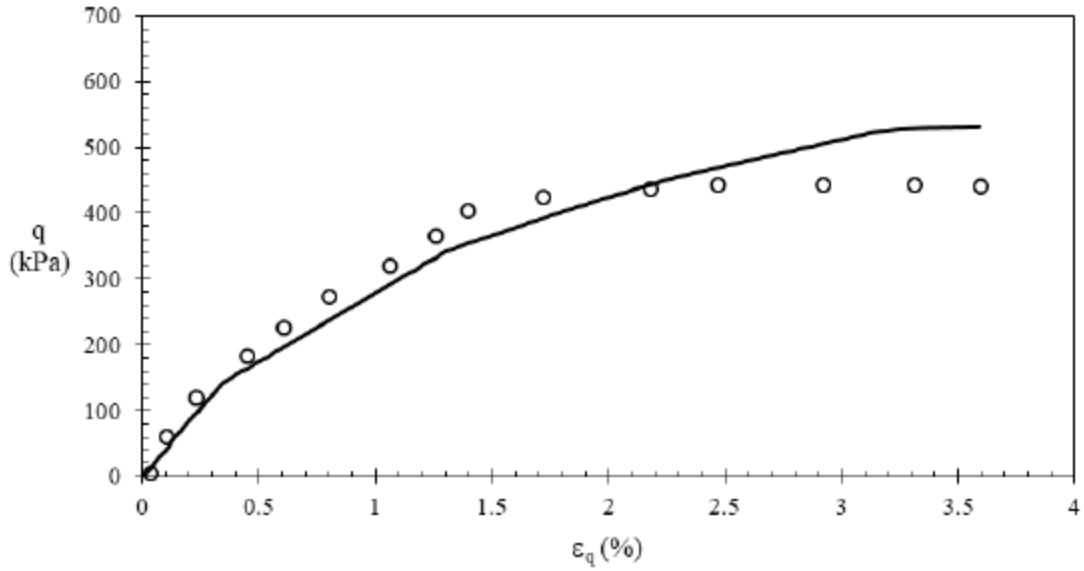

(a)

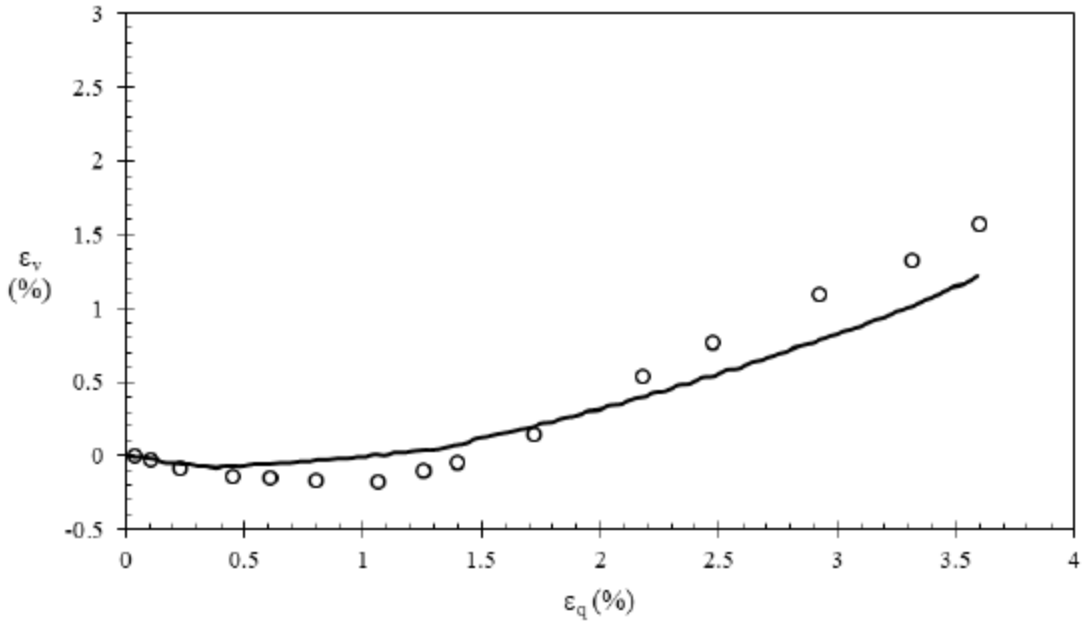

(b)

Figure 2.11 The testing results for (a) the deviator shear and the (b) volumetric strain test data for LBS at 100 kPa, where the solid line represents the model and the points are test data.

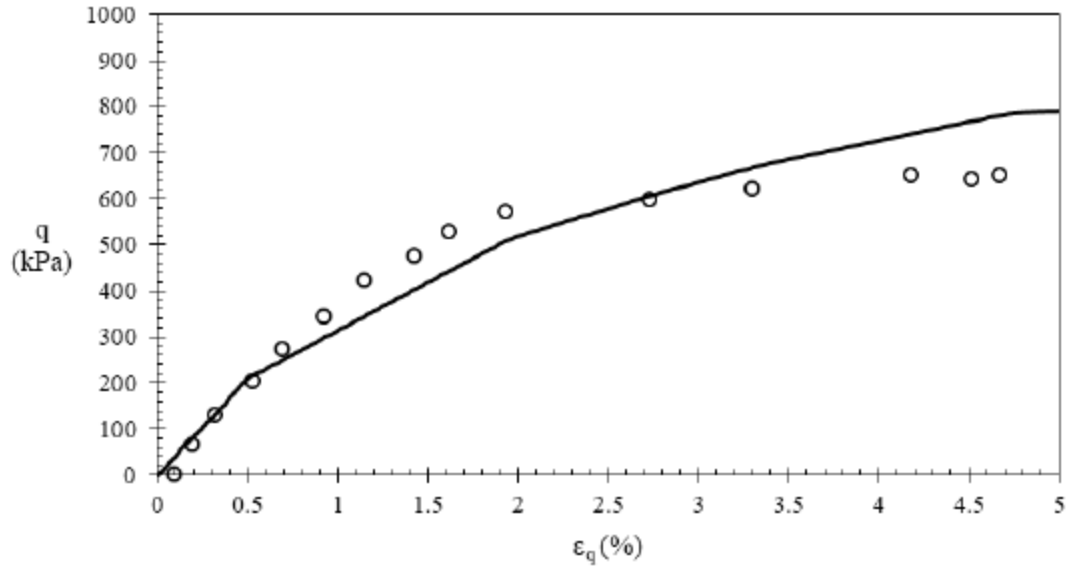

(a)

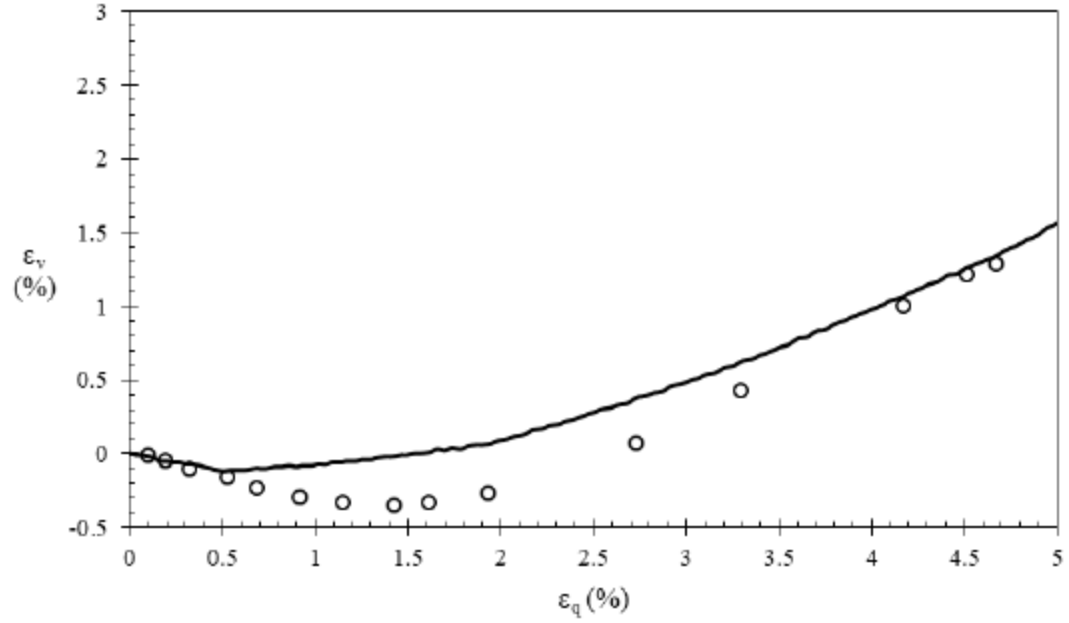

(b)

Figure 2.12 The testing results for (a) the deviator shear and the (b) volumetric strain test data for LBS at 150 kPa, where the solid line represents the model and the points are test data.

The test results for the 100 kPa and the 150 kPa are shown in Figure 2.11 and Figure 2.12, respectively. It is worth noting that the model captures both the dilation and contraction volume changes represented in the test data. The shear response at the remaining two confining pressures again is slightly stiffer than the test response, where the model does not fully mobilize the strength from all the mechanisms until higher strain levels.

2.5.2.3 Crushed Limestone Type 610

The MMM was then calibrated against the triaxial compression test data for the type 610 crushed limestone, at a confining pressure of 552 kPa. The results of the calibration can be seen in Figure 2.13. The model was then tested against the remaining two confining pressures to ensure the model captured requisite shear behavior. The testing results are shown for the 207 kPa and 345 kPa confining pressures in Figure 2.14 and Figure 2.15, respectively. For the calibration simulation at 552 kPa, the model fit the test data well during initial loading but was not as stiff as the test specimen during unloading. On the other hand, the MMM did not reach the peak deviator stress value during initial loading during the testing against the remaining two confining pressures, but matched well with the unloading test data.

The MMM was also tested against the resilient modulus test data conducted by Smith (2000). The results for the test can be found in Figure 2.16. The model assumes the stiffness upon unloading is equal to the stiffness during initial loading. The resilient modulus test data, however, shows a clear distinction between the stiffnesses upon initial loading and unloading. This could be a result of sample preparation and effects from initial seating and consolidation, where even though the sum of the internal shear and hydrostatic forces are at equilibrium before the deviator stress is applied, the stiffness response of the limestone is still clearly affected.

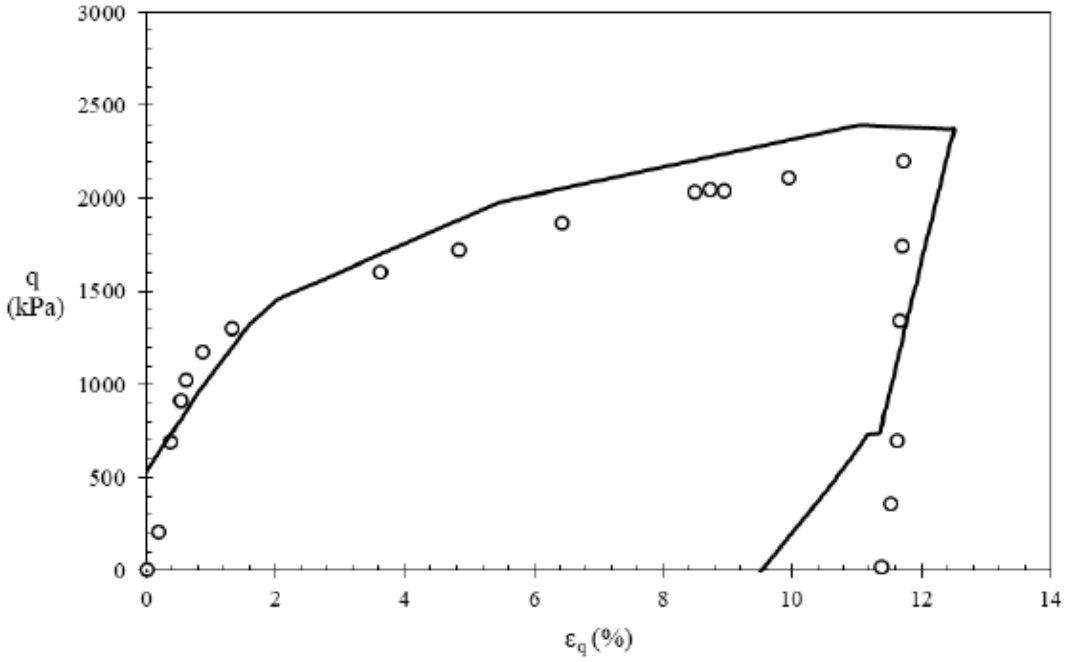

Figure 2.13 The calibration results for CL610 in triaxial compression at a confining pressure of 552 kPa, where the solid line represents the model and the points are test data.

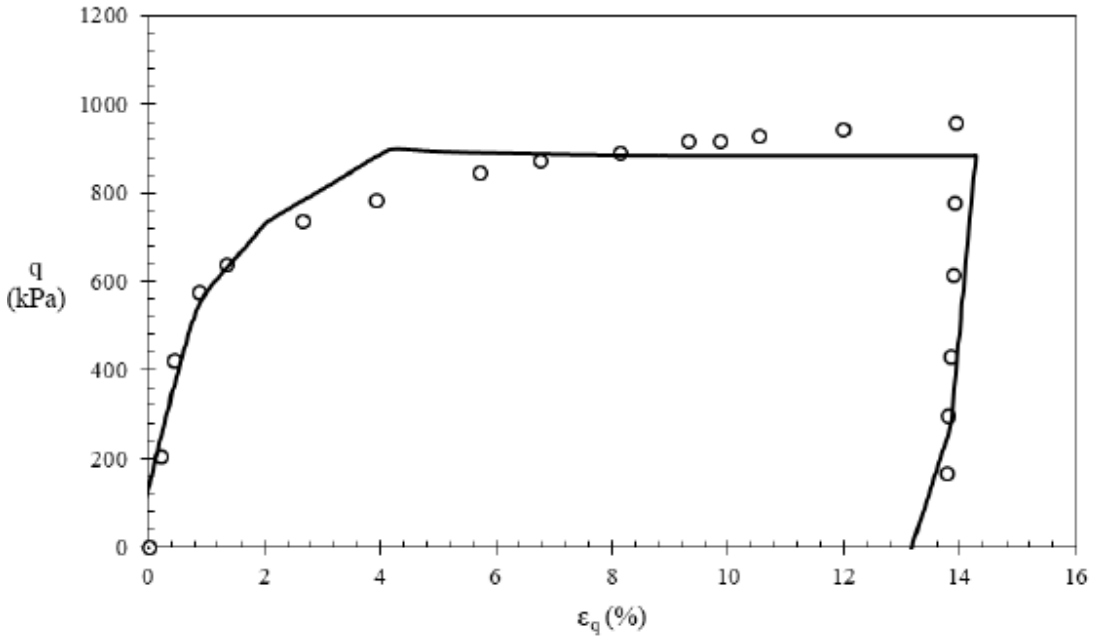

Figure 2.14 The testing results for CL610 against a confining pressure of 207 kPa, where the solid line represents the model and the points are test data.

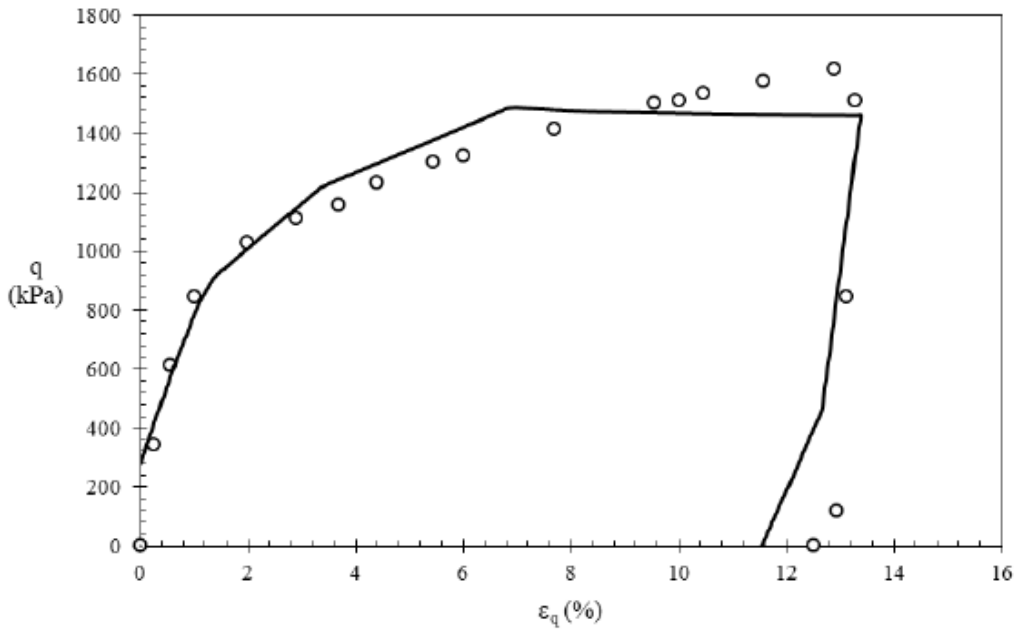

Figure 2.15 The testing results for CL610 against a confining pressure of 345 kPa, where the solid line represents the model and the points are test data.

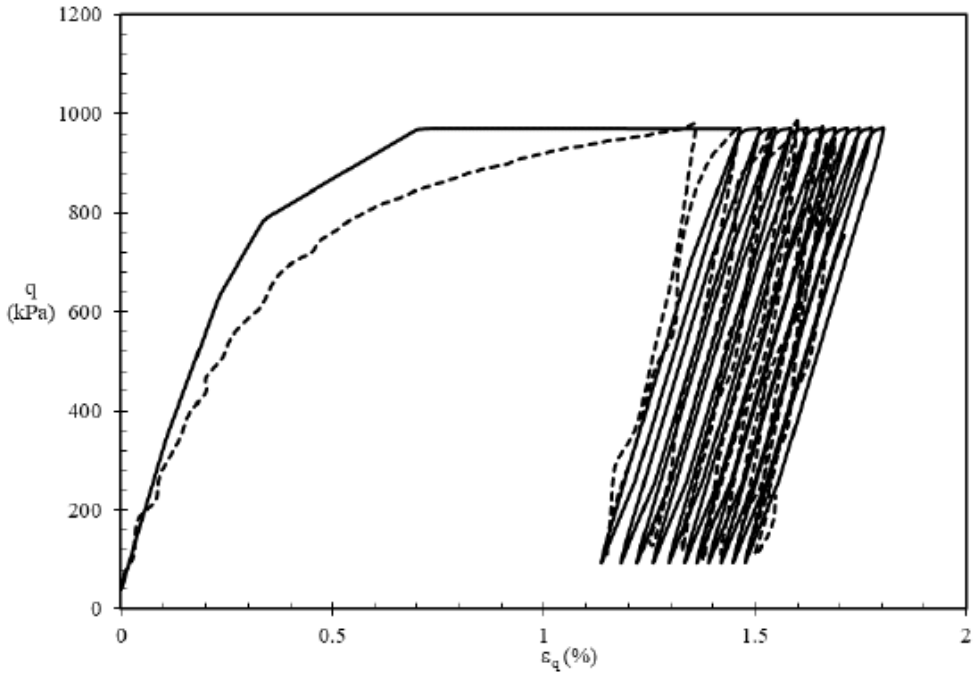

Figure 2.16 The testing results for CL610 against resilient modulus test data at a confining pressure of 345 kPa, where the solid line represents the model and the points are test data.

This phenomenon is not well understood and is an important subject to be investigated in future research. It can be seen from Figure 2.16 that the model was adjusted to have a stiffer response during initial loading to better match the stiffness during stress reversals. Figure 2.17 shows how well the model's ratcheting effects through 50 stress reversals match the test data. Lastly, a series of resilient modulus tests were simulated to show how the model is capable of representing the stress hardening effect characteristic of base aggregate materials such as limestone. Figure 2.18 shows the results of the resilient modulus test simulations, where the model is clearly demonstrating how limestone exhibits less deformation with increasing applied stress.

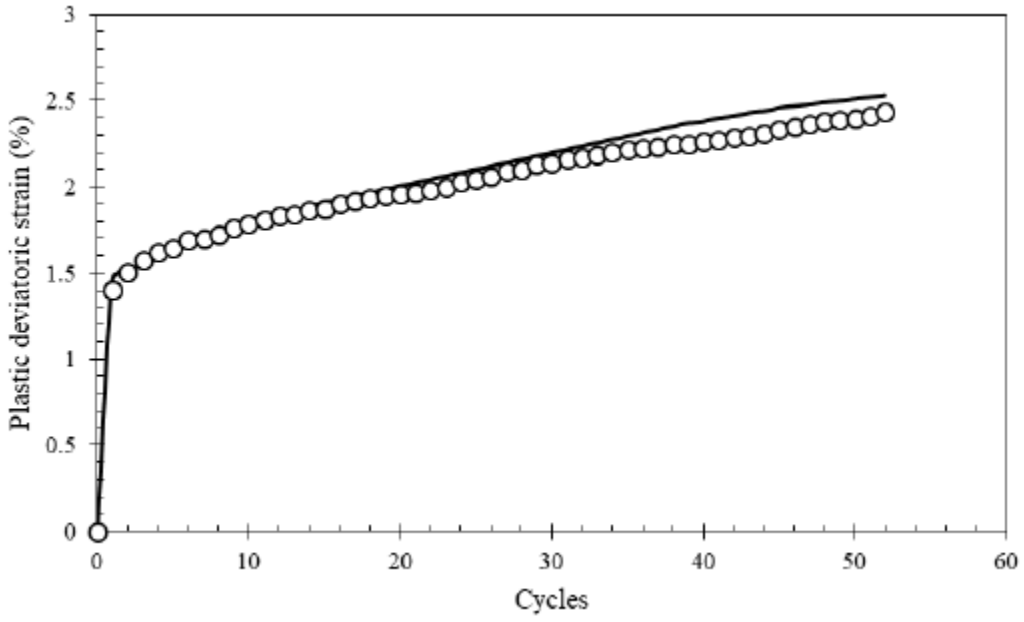

Figure 2.17 Simulated data against the data plots of plastic shear strain for each stress reversal for 50 cycles of the resilient modulus test on CL610, where the solid line represents the model and the points are test data.

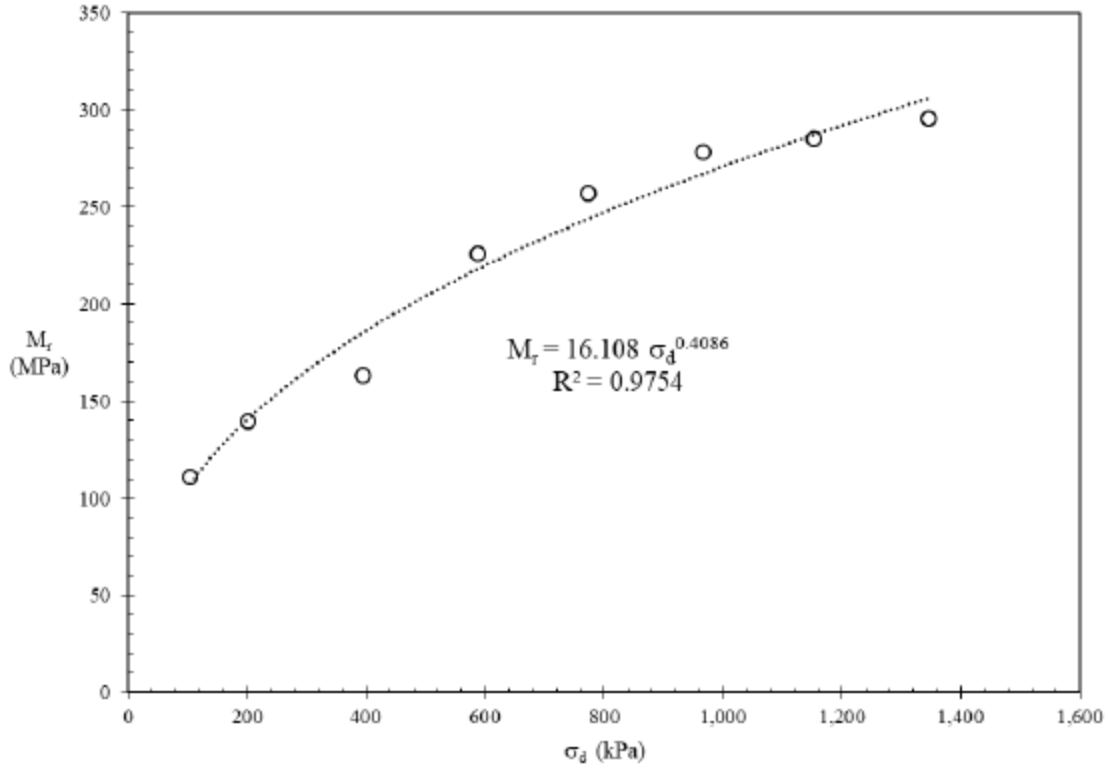

Figure 2.18 Simulations of the resilient modulus test against deviator stress, showing the hardening effects of the model characteristic of a base aggregate material such as limestone.

2.5.3 Error Analysis and Parameter Study

It is important to understand than there is no optimization technique implemented in the calibration process of the MMM. The global parameters are obtained from conventional laboratory test data, while the mechanisms are estimated using the technique provided by Berney (2004) described above. It is possible to conduct a Monte Carlo simulation where the mechanism parameters are iterated upon using a least squares approach to refine model's calibration. But the physical meaning of the mechanism parameters described by Berney (2004) then loses its significance and the user is uncertain of what the values mean.

An error analysis was conducted using a simple root mean square error (RMSE) estimator for the calibration events of each soil type. The general form of the RMSE equation is given as:

$$RMSE = \frac{1}{n}\sum_{i=1}^{n}\sqrt{\left(y_{m,i} - y_{p,i}\right)^2} \tag{2.22}$$

where the sample number is given by n, $y_{m,i}$ is the measured value, and $y_{p,i}$ is the predicted value. The RMSE value prevents positive and negative residuals from canceling out, thus providing a transparent indicator of deviation. The results of the error analysis can be found in Table 2.6.

Table 2.6 Error analysis of the Multi-Mechanical Model during calibration for each soil type.

	σ_3	RMSE		
Material	(kPa)	q (kPa)	du_w (kPa)	ε_v (%)
VBC	103	91.5	36.8	--
	207	12.2	15.3	--
	345	12.9	8.9	--
LBS	40	17.5	--	0.25
	100	43.5	--	0.18
	150	61.5	--	0.22
Limestone	207	53.4	--	--
	345	81.3	--	--
	552	177.3	--	--

The sources of error due to the model parameters can also be estimated using an approach that quantifies the contribution to variance from each parameter. To conduct this error propagation analysis, an approximation is made for the variance value, as shown in (2.23).

$$\sigma_y^2 = \sum_{i=1}^{n}\left(\frac{\partial f}{\partial x_i}\right)^2 \sigma_i^2 \approx \sum_{i=1}^{n}\left[\frac{f(x_i + \Delta x_i) - f(x_i - \Delta x_i)}{2x_i}\right]^2 \sigma_i^2 \tag{2.23}$$

where the variance for the model parameters is given by σ_y^2, f is the model function, and x_i refers to the model parameters of function f. Each parameter was varied by some small amount, Δx_i, and the sum of all the variances were taken and then used to determine each parameter's contribution to the variance in the model. The partial derivatives were estimated using a central finite difference approach. The analysis was conducted at different strain levels to observe the evolution of contribution each parameter made to the overall variance found in the model. The plotted results of the error propagation analysis can be found in Figure 2.19.

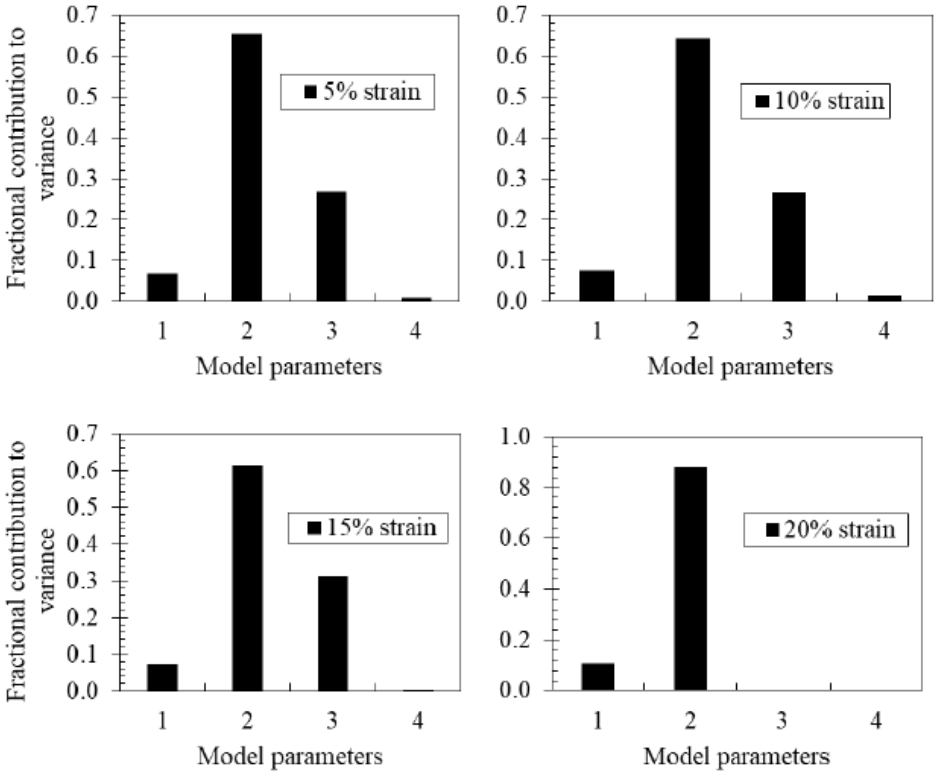

Figure 2.19 Results from error propagation analysis of the MMM against the VBC triaxial test data with respect to shear response, where model parameter 1 = μ_r, 2 = α_r, 3 = G_{ratio}, and 4 = K_{ratio}.

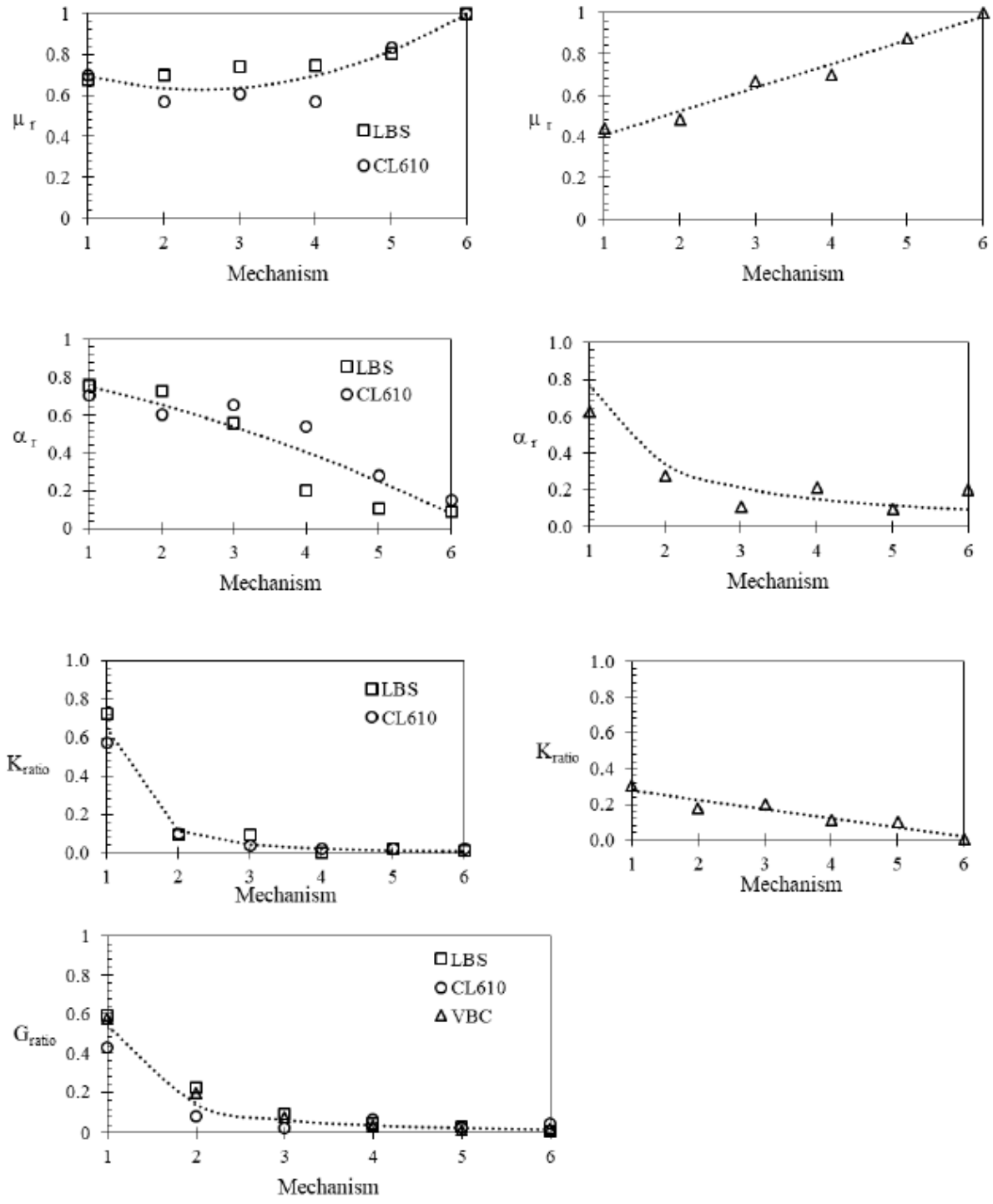

Figure 2.20 Regression plots for estimating the frictional strength parameter (top), mean stress parameter (2nd row), bulk ratio (3rd row), and shear ratio (bottom); predictive curves for granular materials are on the left side and cohesive materials on the right. The shear ratio curve fits both material types.

It is clear that the frictional strength parameter μ_r and the mean stress factor p_r are consistently contributing to the variance of the model, whereas the shear ratio is influential up until larger strains and the bulk ratio is least influential of all. This is helpful in isolating the mechanism parameters that affect the model the most.

Finally, a parameter study was conducted to further expedite calibration efforts for users. All the mechanism parameters determined in this study were plotted together, and polynomial regression equations were determined with respect to each mechanism, as shown in Figure 2.20. Each regression equation with its respective R^2 value for goodness of fit is provided in Table 2.7.

Table 2.7 Correlation equations to approximate mechanism parameters

Parameters	Material type	Correlation equations	R^2 value
Frictional strength factor	Granular	$\mu_r = 0.0295r^2 - 0.1462r + 0.8105$	0.824
	Cohesive	$\mu_r = 0.1142r + 0.2948$	0.971
Mean stress factor	Granular	$\alpha_r = -0.0094r^2 - 0.0692r + 0.831$	0.854
	Cohesive	$\alpha_r = 0.7712r^{-1.1581}$	0.832
Shear stiffness factor	General	$G_{ratio} = 0.5361r^{1.891}$	0.846
Volumetric stiffness factor	Granular	$K_{ratio} = 0.647r^{-2.483}$	0.974
	Cohesive	$K_{ratio} = -0.0514r + 0.3293$	0.901

These equations can act as good starting points for users in easily finding mechanism parameters for different soil types, but a few useful observations about the parameters can guide the user in further refinement. Both the shear and bulk ratio parameters typically add up to (but do not exceed) unity and are generally decreasing for most soils in monotonic loading. The

frictional strength parameter typically increases to unity with each mechanism, while the mean stress parameter generally decreases with each mechanism.

CHAPTER III

CRITICAL FACTORS IN SUBGRADE RUTTING FAILURES OF AIRFIELD MATS OVER SOFT SOILS UNDER STATIC LOADING

This chapter has been submitted for review and possible publication in a scholarly journal. The paper is currently under peer review process while this dissertation has been written. This chapter has been reformatted and replicated herein with minor modifications in order to outfit the purposes of this dissertation.

3.1 Introduction and Background

Matting systems such as the AM2 are used to construct expedient airfields during deployed military operations. These airfields are typically constructed over existing subgrades. Mat system applications also extend beyond military contingency operations. For example, they are used by the oil and gas industry where mobility is required over swampy terrain. Mats are also used in tundra regions due to environmental concerns as a protective surface to better distribute vehicle loads (Gartrell, 2007). Extensive field testing has shown that over relatively stiff existing subgrades (e.g., CBR > 10), AM2 mats fail in a fatigue-type failure mechanism called mat breakage (e.g., Rushing et al., 2008b; Garcia et al., 2014). On the other hand, AM2 mats placed over soft cover materials or subgrades typically fail by rutting (e.g., Rushing and Tingle, 2007). Airfield mats are emplaced when equipment and manpower are limited, logistics are challenging, and the quality of engineered materials are marginal (e.g., Gartrell, 2007). Consequently, AM2-surfaced airfields are typically emplaced over relatively soft material. As

such, it is important to identify the critical factors that contribute to the accumulation of permanent deformation in the supporting subgrade that lead to rutting failures for the accurate design and evaluation of AM2 airfield matting structures.

An expedient airfield constructed with landing mats presents a distinct geotechnical challenge in soil-structure interaction problems (e.g., White, 1971). There are analogous features of airfield mats found in low volume roads (LVR) since LVRs are also relatively thin pavement structures. Figure 3.1 shows the vertical stress at the top of the subgrade for AM2 and LVR sections, respectively. While the LVR is a relatively thin pavement structure compared to other corresponding highway and airfield structures, the LVR asphalt and base layers still clearly distribute the vehicle load more than the AM2 matting. The point of this illustration is that even with respect to LVR sections, airfield mats pose a unique challenge with respect to rutting failures.

Historically, there has been significant field testing of the AM2 mat system dating back to the 1960s, such as those discussed in the development of the original mat performance criteria (e.g., Thompson and Burns, 1960; Burns and Fenwick, 1966; Ulery and Wolf, 1971). More recent military testing and evaluation efforts of the AM2 mat systems include the Rapid Parking Ramp Expansion Program (Rushing and Tingle, 2007; Rushing et al., 2008; Rushing and Mason, 2008; Garcia et al., 2014a, 2014b), which were used in the development of a new proposed mechanistic-empirical mat performance criteria (Stache et al., 2019a). Furthermore, these studies and many other investigations not mentioned here were used in identifying the different failure mechanisms that occur in mat systems and in developing lighter expeditionary surfaces with thinner profiles, lower densities, and improved welding technologies.

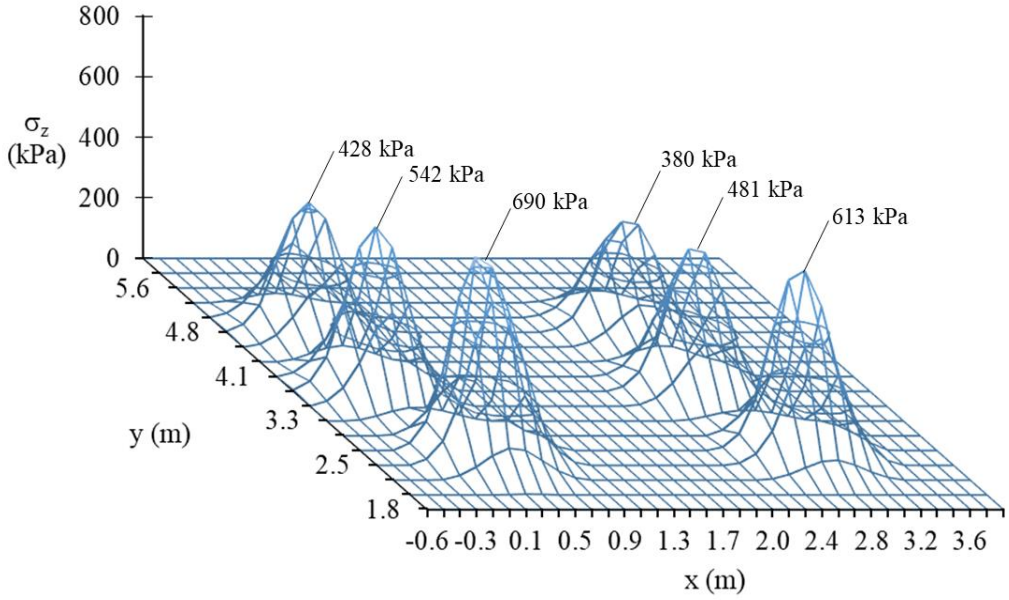

(a)

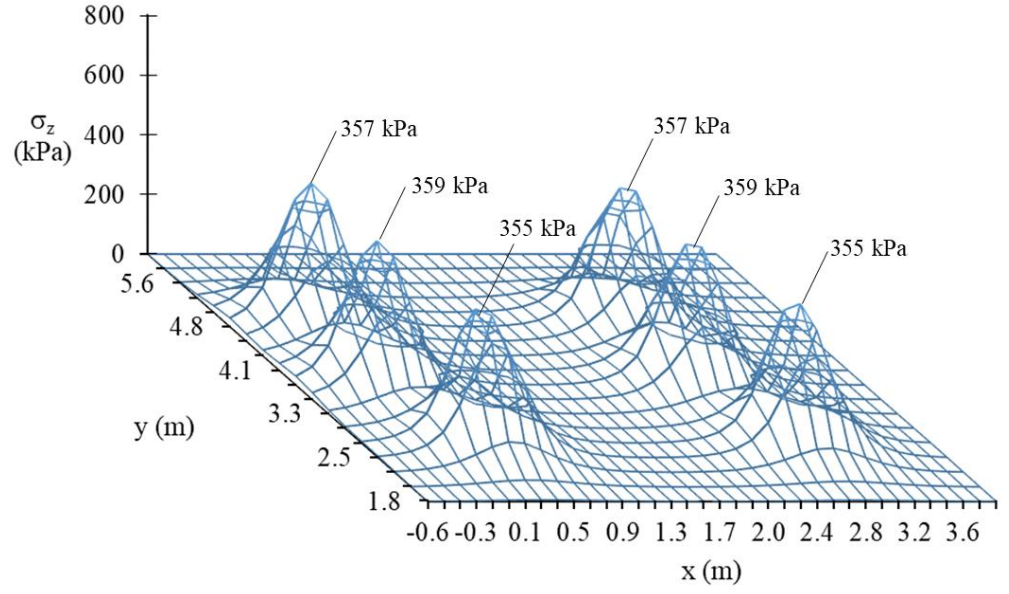

(b)

Figure 3.1 Vertical stress distribution for a C-17 main gear loaded onto (a) an AM2 mat, and (b) a LVR section.

Numerical analyses, on the other hand, are much less prevalent. Foster (2007) simulated a foam webcore mat system using an isotropic elastic material model for the subgrade with infinite elements as a part of the AM-X program. Leski et al. (2012) modeled a mobile, composite airfield mat with an elastic subgrade material model to confirm field-testing results. Finally, Doyle et al. (2012) conducted FE analysis on various mat systems using the Drucker-Prager constitutive material model for the subgrade and made comparisons with earth pressure cell (EPC) data from several test sections. It is important to note that whereas the first two papers focused on mat response, only the third study truly looked at subgrade stress response.

Looking outside the community of airfield matting numerical studies, some comparable studies in LVRs are notable. While LVRs are not as thin as airfield mats, nor do they accept vehicles with as high of gross loads or tire pressures, rutting is still the predominant failure mechanism where soft subgrades exist. For example, Allou et al. (2010), Gupta et al. (2015), and Werkmeister et al. (2015) identified rutting as the primary failure mechanism in LVRs and propose new methods to address shortcomings in current design procedures based on shakedown theory and mechanistic response (i.e., based on stresses or strains). Sahoo and Reddy (2010) and Kim and Lee (2011) highlighted the nonlinear, elastic response of the unbound granular layer using the resilient modulus, since it acts as the main structural component in LVRs with thin bituminous surfacing. Qui et al. (2000), however, pointed out that the resilient modulus is not sufficient to characterize the subgrade deformation response, and a stress-based mechanistic procedure must be incorporated into current LVR design approaches. Similarly, Tolentino et al. (2019) discuss the need for a fully mechanistic design procedure implementing an elastic-plastic constitutive model for unbound granular materials since rutting failures in base layers are not uncommon in thinly paved roads. Consequently, the findings from the aforementioned LVR

studies reinforce the point that modeling the subgrade deformation response in thin airfield mat structures is an important research need in the pavements and geotechnical communities.

The purpose of this study is to investigate how various geometric and structural factors contribute to the response of a subgrade under an AM2 matting system subjected to aircraft loads through analysis of full-scale testing, linear and nonlinear layered elastic analysis (LEA) and three-dimensional FE modeling. Such factors include the aircraft gross load, landing gear configuration, and the stiffness and thickness of the engineered cover material. Other significant factors that affect the deformation response of the subgrade include the load transfer occurring in the mat joints and the soil-mat interface bonding condition. The FE model of the AM2 mat system is built by implementing a user-defined constitutive model, MMM, to simulate the soft soil subgrade response. The results of the FE model are compared against those attained from a set of full-scale testing and LEA. The FE model is then used in a series of sensitivity studies to explicate the varying effects that factors such as loading conditions, subgrade cover material, mat joint load transfer, and mat-soil interface condition have on deformation response. Primary focus is placed on addressing two unique aspects of the mat problem that are not well understood: the effects of modeling the mat as a jointed system and modeling the soil-mat interface conditions.

3.2 Finite Element Modeling

3.2.1 Geometry

In this study, we numerically simulate the AM2 mat system using the commercial FE software *ABAQUS* (*ABAQUS*, 2017). As shown in Figure 3.2, two different FE models are used to represent the AM2 mat – a continuous, medium thick plate and a jointed system of plates assembled in a brickwork (staggered) lay pattern linked together using *ABAQUS* connector elements. The connector elements define the translation and rotation degrees-of-freedom (DOF)

for two interlocking mats. Besides allowing for load transfer to occur between interlocking mats, the connector elements better resemble the actual AM2 mat connections by providing a unique flexural response that is distinct from the continuous plate. In the case of the jointed mat FE model, the dimensions defined in Table 3.1 were used.

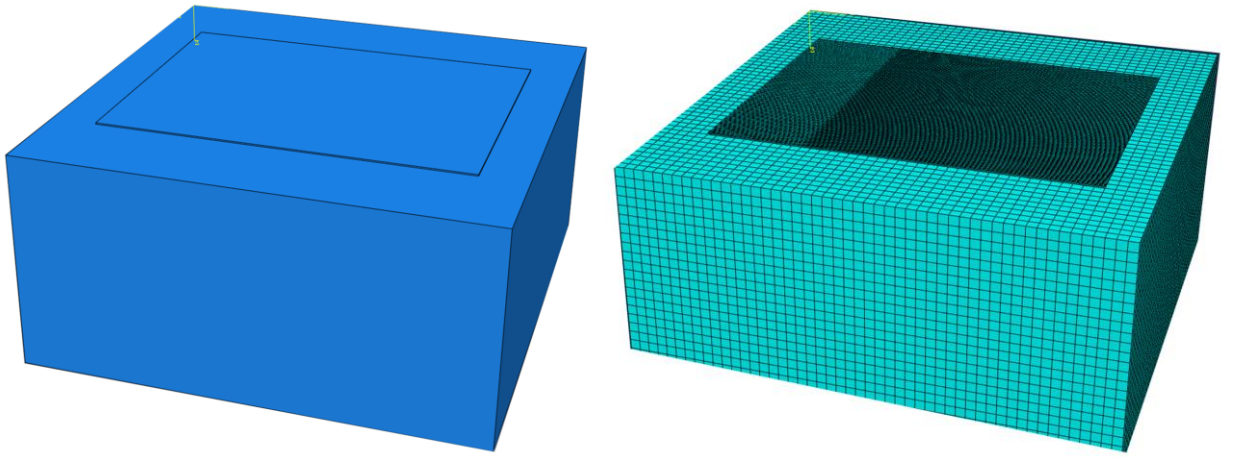

(a)

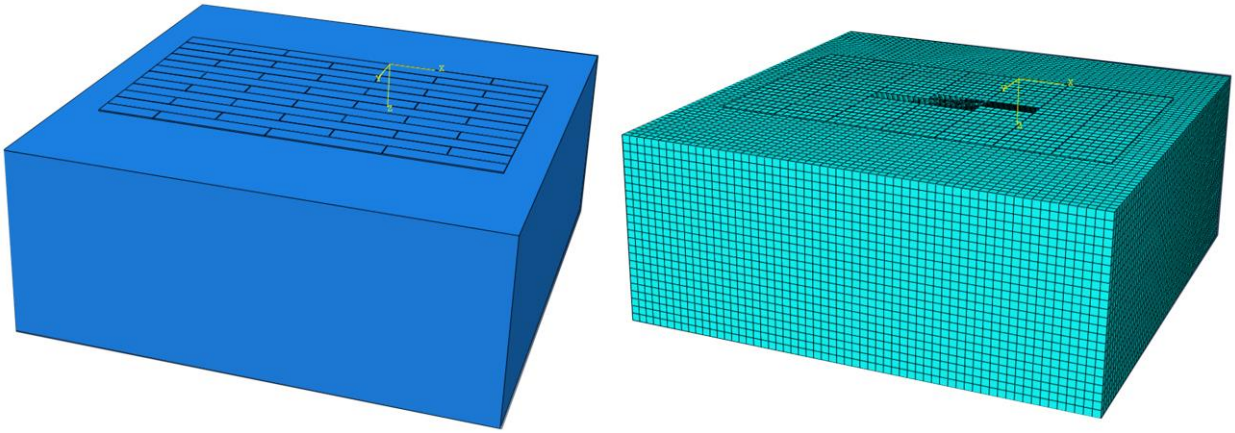

(b)

Figure 3.2 (a) FE model and mesh for the AM2 “plate” model; (b) FE model and mesh for the AM2 “jointed mat” model

Table 3.1 Geometric and density properties for the AM2 mat

AM2 Mat	Length (m)	Width (m)	Thickness (mm)	Unit Weight (kN/m^3)
Full panel	3.66	0.6	38.1	647
Half panel	1.83	0.6	38.1	331

3.2.2 Constitutive Models

The AM2 mat system is estimated as a medium-thick plate. There have been a number of methods for approximating or "back-calculating" the modulus of elasticity of the composite AM2 mat. Gonzalez and Rushing (2010) conducted a back-calculation of the modulus of elasticity using a simply supported three-point bending test. FE simulations were conducted where deflection basins were matched using the measured flexural rigidities from the test while adjusting the modulus of elasticity using the Mindlin plate solution (1951). Equation (3.1) was used to iterate upon the modulus of elasticity values in the FE model.

$$D = \frac{Eh^3}{12(1-v^2)} \tag{3.1}$$

where D is the flexural rigidity of the composite mat, E is the composite mat modulus of elasticity, h is the mat thickness, and v is the Poisson's ratio. Doyle et al. (2012) used a similar test setup as Gonzalez and Rushing (2010) for a single panel, while also attempting to quantify a composite modulus that included the joint. Doyle et al. (2012) noted that these latter values were less reliable and further research was needed. Finally, Rushing and Howard (2018) implemented a test procedure that attempted to quantify the flexural modulus of the mat in the strong and weak directions. For the purpose of this study, the methodology used in Gonzalez and Rushing (2010) is adopted to characterize the mat in the FE model. Full-scale testing of the AM2 shows

that the mat has an elastic response at low levels of stress repetitions, regardless of the subgrade stiffness. As such, it is appropriate for this study to assume the AM2 mat can be characterized by only the back-calculated composite modulus and Poisson's ratio.

To simulate the subgrade response, the MMM is defined and implemented as a user-defined material model (UMAT) in *ABAQUS*. The MMM is an elasto-plastic kinematic hardening model developed and validated in Chapter 2 (Stache et al., 2019b). The rest of this section provides an overview of key characteristics of the MMM.

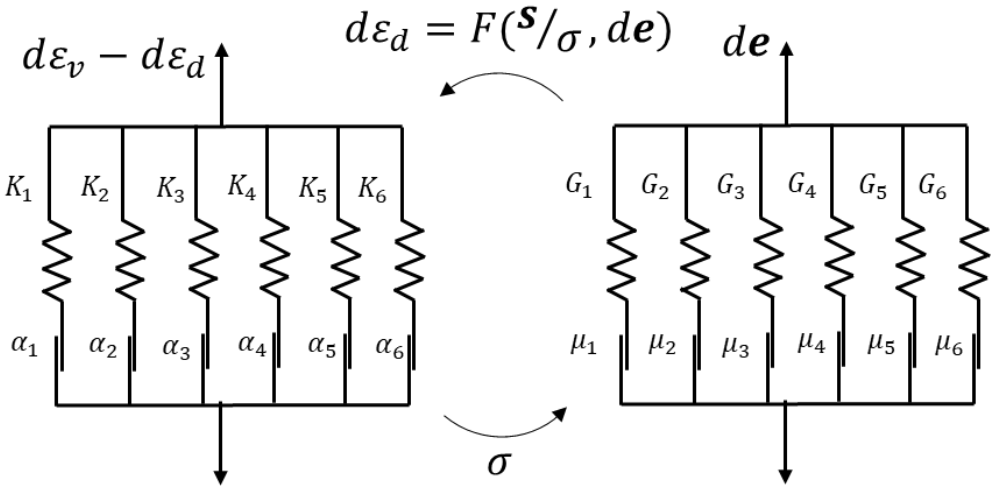

Figure 3.3 Maxwell representation of the MMM. The shear (right) and purely hydrostatic (left) mechanisms are coupled by a shear-dilatancy relationship.

The MMM (Stache et al., 2019b) is an elastic-plastic material model that consists of a Maxwell array of six elastic spring and plastic slider mechanisms. Each spring-slider mechanism is composed of both shear and hydrostatic components that are coupled by a shear-dilatancy law,

as can be seen in Figure 3.3. The fundamental constitutive equations for the MMM are as follows:

$$\boldsymbol{Q}^r = \boldsymbol{Q}_s^r + \alpha_r(\sigma + a) \tag{3.2}$$

$$\sum_{r=1}^{n} Q_h^r = \sigma + a \tag{3.3}$$

The total intergranular stress $\boldsymbol{Q}^r$ for each mechanism *r* can be expressed in terms of its deviatoric $\boldsymbol{Q}_s^r$ and hydrostatic Q_h^r components. The hydrostatic stress component consists of the sum of the total hydrostatic stress, σ, and the hydrostatic offset, a, which corresponds to the Mohr-Coulomb cohesion. Also, α_r is a factor that distributes the hydrostatic stress seen by each mechanism *r*. The shear and hydrostatic responses are governed by two yield criteria:

$$f(\boldsymbol{Q}^r) = \frac{I_1^r I_2^r}{I_3^r} \tag{3.4}$$

$$Q_h^r = H^r P_e(e) \tag{3.5}$$

Equation (3.4) corresponds to the shear yield law of the intergranular stress in the form of the Matsuoka-Nakai criterion. The stress invariant representations of the intergranular stress are given as:

$$I_1^r = Q_1^r + Q_2^r + Q_3^r \tag{3.6}$$

$$I_2^r = Q_1^r Q_2^r + Q_2^r Q_3^r + Q_1^r Q_3^r - \left(Q_4^{r\,2} + Q_5^{r\,2} + Q_6^{r\,2}\right) \tag{3.7}$$

$$I_3^r = Q_1^r Q_2^r Q_3^r - Q_1^r Q_6^{r\,2} - Q_2^r Q_5^{r\,2} - Q_3^r Q_4^{r\,2} + 2Q_4^r Q_5^r Q_6^r \tag{3.8}$$

Equation (3.5) corresponds to the hydrostatic yield law governed by a function of the reference stress P_e at the prevailing void ratio. The parameter H^r determines the yield of the hydrostatic mechanisms and is unique to each mechanism forming the stress-strain response.

The shear-volume coupling at the global level is accomplished through the following relationship:

$$\gamma \boldsymbol{s} \cdot d\boldsymbol{e}^p + \sigma d\varepsilon_d = \gamma M_c \sigma \sqrt{d\boldsymbol{e}^p \cdot d\boldsymbol{e}^p} \tag{3.9}$$

The parameter $\boldsymbol{s}$ is the deviatoric stress**,** $d\boldsymbol{e}^p$ and $d\varepsilon_v$ are the increments of plastic shear strain and volumetric strain, and M_c is the critical state coupling parameter. Lastly, the parameter γ modulates the effect of the shear-volume coupling, and $d\varepsilon_d$ is the increment of hydrostatic strain resulting from the shear-volume coupling.

Table 3.2 Average densities and moisture contents from full-scale test section (data from Rushing and Tingle 2007)

Sampling Location in Subgrade (cm)	Wet Density (kN/m^3)	Dry Density (kN/m^3)	Moisture (%)	Oven Moisture (%)
F-15E Before Trafficking				
0	18.6	14.2	30.8	35.1
15.2	18.8	14.4	30.3	33.3
30.5	18.7	14.5	29.7	33.4
45.7	18.6	14.2	30.6	33.2
61.0	18.8	14.3	30.8	33.5
76.2	18.2	13.9	31.4	32.3
C-17 Before Trafficking				
0.0	18.6	14.3	30.2	34.4
15.2	18.7	14.4	30	32.6
30.5	18.8	14.5	29.4	32.6
45.7	18.6	14.2	30.5	33.5
61.0	18.6	14.3	30.5	32.8
76.2	18.2	13.8	31.7	32.7

Since the average densities and water contents for the Buckshot clay from Table 3.2 result in a degree of saturation exceeding 90%, a fully-saturated assumption for the subgrade was made corresponding to the calibrated MMM parameters found in Stache et al. (2019b). Table 3.3

and Table 3.4 detail all the material and geometric properties used in comparing the FE model against the LEA solutions, as well as the parameters used in comparison against the full-scale instrumented test data.

Table 3.3 Geometric and material input parameters for each model

Layer and thickness	***Linear LEA***	***Nonlinear LEA***	***FE Model***
AM2 mat t_{mat} = 38.1 mm	*E* = 27,372 MPa *v* = 0.4	*E* = 27,372 MPa *v* = 0.4	*E* = 27,372 MPa *v* = 0.4
Subgrade (CH) t_{sbg} = 6,096 mm	*E* = 55,413 kPa *v* = 0.2	M_r = 55,413 kPa *v* = 0.2	Calibrated values See *Table 3.4*

Table 3.4 Calibrated MMM parameters for Vicksburg Buckshot clay

Parameter	**Description**	**Calibrated value**
β	Reciprocal of Cc on the normal consolidation line	3.757
e_{ncl}	Intercept of the NCL on *e*-log*p'* plot	1.4
c	Mohr-Coulomb cohesion parameter	86.2 kPa
M_c	Coupling parameter for shear-induced volume changes	1.0
γ	Reduces the effects of dilatancy during shearing	0.015
ϕ	Mohr-Coulomb friction angle	11.5 degrees
d	Controls rate of frictional strength reduction with OCR	1.5
ϕ_{ratio}	Ratio of max and min friction angles from failure line	0.619
K	Elastic bulk modulus	38,956 kPa
G	Elastic shear modulus	29,213 kPa

		Mechanisms and Associated Parameter Values					
Parameter	**Description**	**1**	**2**	**3**	**4**	**5**	**6**
μ_r	Frictional scaling factor	0.44336	0.48118	0.66653	0.70206	0.87370	1.00000
α_r	Mean stress factor	0.62550	0.27681	0.10924	0.21151	0.09600	0.20173
G_{ratio}	Shear ratio distribution	0.57764	0.19639	0.08254	0.03556	0.01165	0.01971
K_{ratio}	Bulk ratio distribution	0.30400	0.17500	0.19900	0.11100	0.10100	0.00600
H^r	Compression limit	0.15990	0.36472	0.55459	0.69153	0.90460	0.95460

3.2.3 Boundary Conditions, Mesh, and Loadings

In the FE models, the lateral extents and bottom of the subgrade are pinned. The mat system is also pinned, which corresponds to the anchoring system in full-scale testing. Throughout the FE simulation program, the mats were typically modeled with 10-noded tetrahedral elements (C3D10), and the subgrade was modeled with 8-noded brick elements (C3D8). Contact pairs were implemented in *ABAQUS* to define the contact at the mat-subgrade interface. The tangential behavior was either defined as a frictionless full-slip condition or a rough no-slip condition, where the mat was either allowed to slide freely over the soil surface or no sliding was allowed, respectively. The normal behavior was defined by a classical Langrage multiplier hard contact pressure-overclosure relationship, where contact pressures are fully transmitted between the mat and soil surfaces once they are in contact.

Images of individual AM2 panels, the fully constructed test section, and the F-15 and C-17 load carts are given in Figure 3.4 and Figure 3.5, respectively. Similar loading conditions are implemented in the numerical models as those used in the Rapid Parking Ramp Expansion (RPRE) full-scale instrumented testing program (Rushing and Tingle, 2007), which will be further described later in this paper. All loads are static in nature and applied as ramp loads over the duration of the time step. Tire contact areas are approximated with an elliptical shape. Each tire in the main landing gear configuration model of the C-17 are spaced in accordance with the C-17 load cart from full-scale testing.

(a)

(b)

Figure 3.4 (a) Individual AM2 full and half panels; (b) the completed AM2 test sections before trafficking (from Rushing and Tingle, 2007)

(a)

(b)

Figure 3.5 (a) The F-15 load cart and (b) C-17 load cart used in testing (from Rushing and Tingle, 2007).

3.3 Comparison to Layered Elastic Analysis

The FE model was compared to both linear and nonlinear LEA programs. The purpose of this exercise is to ensure the FE model is producing appropriate stress and displacement output by comparing it to traditional LEA output. Furthermore, given the difference in subgrade material definitions and modeling approaches it is expected that the stress-deformation response will not match at every point. Therefore, this exercise also serves as a medium for identifying the differences between these two approaches. The linear LEA software *WinJULEA* (2003) characterizes pavement layers using elastic material properties (i.e., modulus of elasticity and Poisson's ratio). The software can be found as a utility program within the Tri-Service airfield design and evaluation computer program *PCASE 2.09.06* (*Pavement-Transportation Computer Assisted Structural Engineering)* (*PCASE 2.09.06*). The nonlinear LEA software *KENLAYER* (1993) implements a variation of Thompson and Elliot's (1985) resilient modulus model for fine-grained soils, which is a stress-softening constitutive model. It is important to note that "nonlinear" in this particular case is not referring to material or geometric nonlinearity, but to the stress-dependent resilient behavior of the fine-grained material. Figure 3.6 shows the graphical representation of this stress-softening model.

The LEA and FE models implemented the same tire contact pressures and contact areas. Each layer in the LEA model is considered to be isotropic and homogeneous and extends infinitely in either horizontal direction, while the bottom layer extends downward to infinity. The interface conditions between layers can be considered fully bonded (i.e., no slip) or unbonded (i.e., full slip), which defines the amount of friction mobilized at the layer interface.

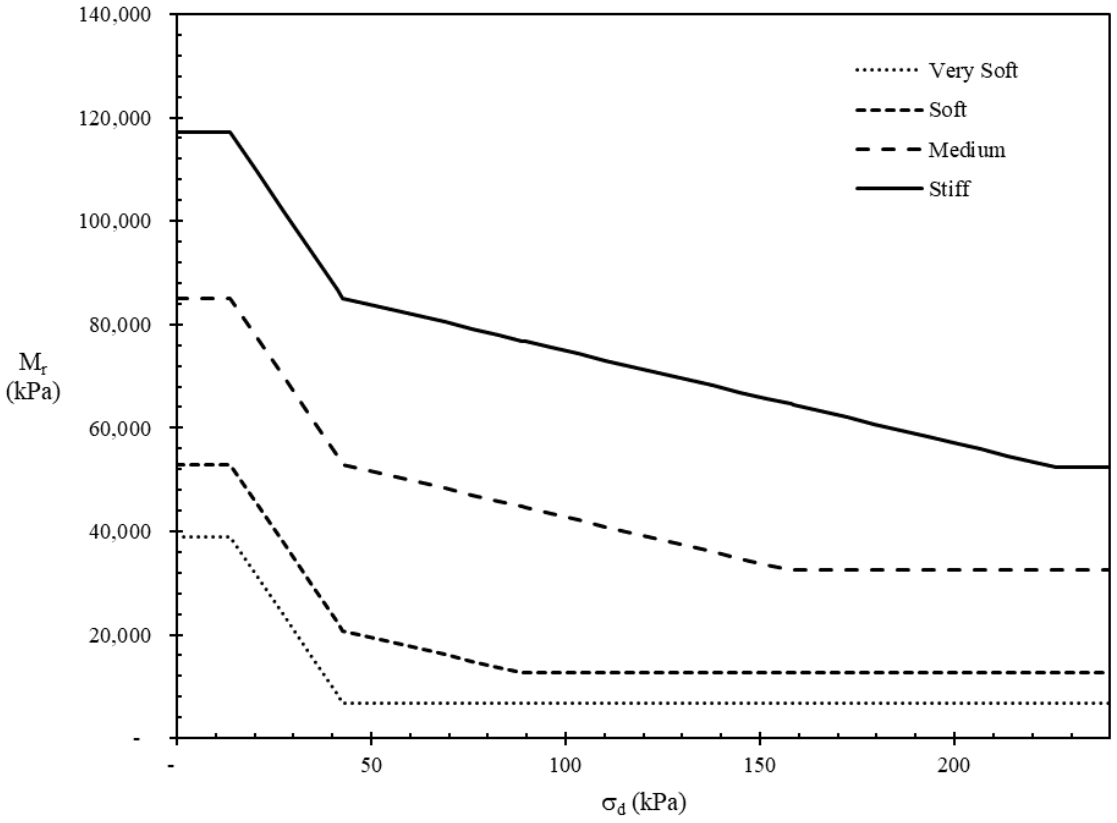

Figure 3.6 The graphical representation of the stress-softening resilient modulus model for fine-grained materials in nonlinear LEA using *KENLAYER* (after Thompson and Elliot 1985)

Figure 3.7 shows the vertical stress response of the 3D-FE model very reasonably matches the linear and nonlinear LEA solutions. As can be expected, the displacements rendered from the jointed mat FE model are slightly higher at the surface than the corresponding LEA solution, which represents the mat layer as a continuous plate. Furthermore, the differences with the displacements with depth can be attributed to two other factors. First, the LEA approach assumes that the last layer extends infinitely downward.

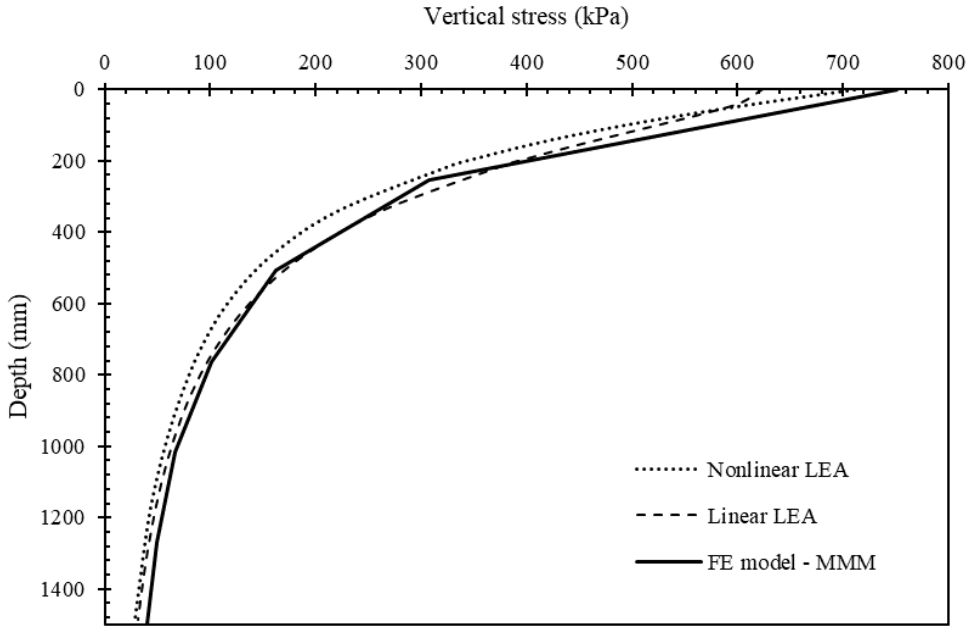

(a)

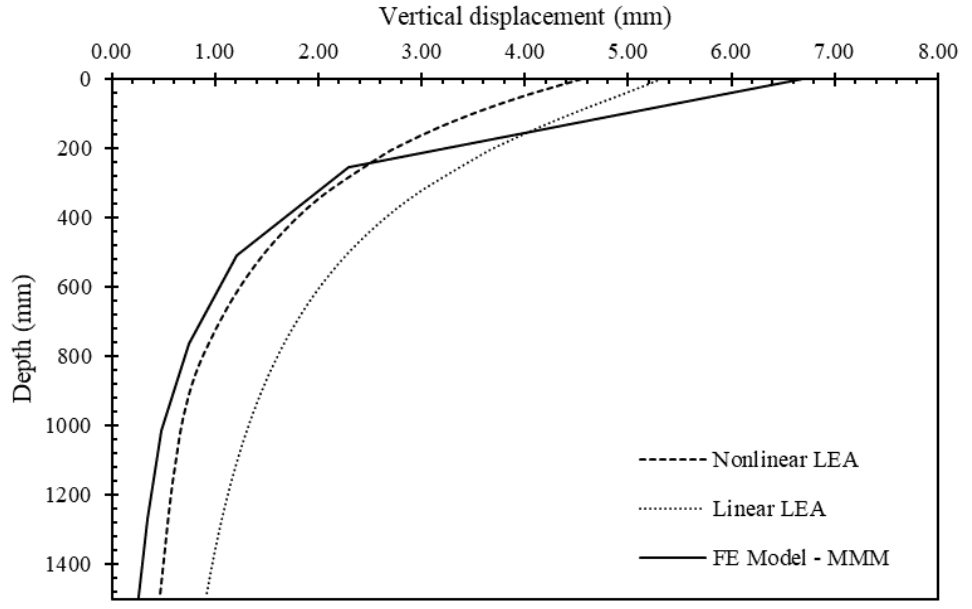

(b)

Figure 3.7 Comparison of simulation results from the FE model (with a jointed mat over elastoplastic subgrade modeled with MMM with unbonded interface) versus linear LEA and nonlinear LEA for F-15 loading: (a) vertical stress, (b) vertical displacement.

Vertical displacements are particularly affected by the lack of a boundary condition in the vertical extent of the model. Second, the LEA solution is confined to elastic material properties, while the FE model implements the elastic-plastic MMM to characterize subgrade response. The FE model can produce the same response as the LEA model given a linear elastic material response for the subgrade material and similar boundary conditions for the subgrade and continuous mat. The advantage of the LEA model is it offers a very simple and quick method for approximating stress and deformation responses. It is clear that a FE-based platform provides much more modeling extensibility. In many cases, the critical factors affecting subgrade deformation can only be modeled with FE method. Therefore, the FE method is a good companion to traditional analyses that will only grow in value as experience is gained in its use.

3.4 Validation Against Full-Scale Test Data

The test data from the Rapid Parking Ramp Expansion (RPRE) full-scale instrumented testing program are used for validation of the FE model (Rushing and Tingle, 2007). The original purpose of the RPRE program was to establish performance metrics for a new lightweight airfield mat to replace the traditional AM2 mat. The program consisted of the full-scale instrumented testing of the AM2 mat system over engineered fill with CBRs of 6, 10, 15, 25, and 100 under simulated F-15 and C-17 load carts. The 6 CBR test data (Rushing and Tingle, 2007) are used for comparison with the FE model.

The AM2 mat consists of a single aluminum extrusion with hinge-type male-female connectors. The adjacent (short) sides are joined by welded overlap-underlap connections secured with an aluminum locking bar. The extruded core consists of vertical stiffeners spaced apart in the long direction. An 18.3-m wide by 12.2-m long section of AM2 matting with two

traffic lanes for the F-15 and C-17 load carts were placed over an 18.3-m wide by 12.2-m long by 0.9-m deep test section consisting of 6 CBR Vicksburg Buckshot (CH) clay.

The test section was instrumented with earth pressure cells (EPC) and single depth deflectometers (SDD) to measure the response of the soil support under the matting. Figure 3.8 shows the instrumentation layout in both plan view and profile view for the F-15 test section to provide spatial locations within the traffic lane and with depth. The AM2 mats were constructed in a brickwork (or staggered) lay pattern as seen in the fully constructed test section in Figure 3.4 and Figure 3.5, where load cart trafficking occurred perpendicular to the long edge of the mat panels. The traffic lane for the F-15 test section was 1.5-m wide.

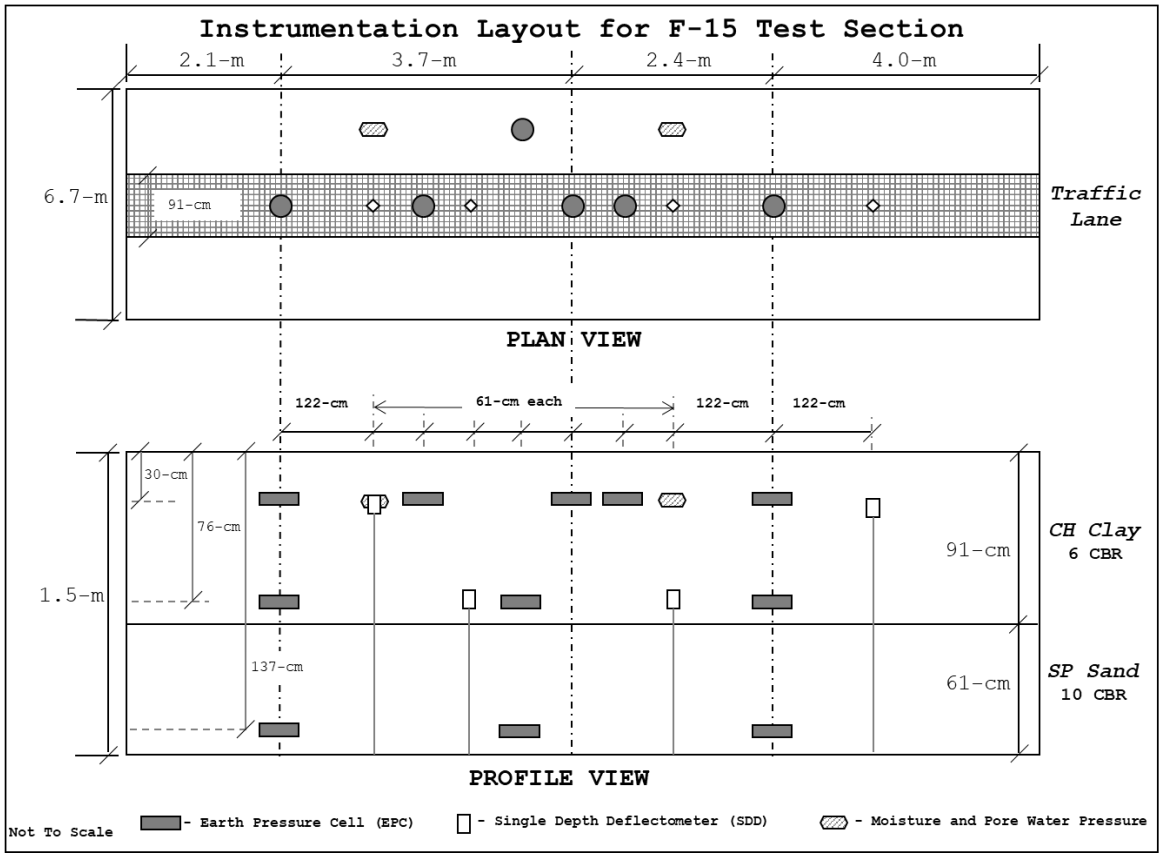

Figure 3.8 Full-scale test section instrumentation layout for F-15 (after Rushing and Tingle 2007)

Following the work of Brown and Thompson (1973), the load cart traffic was distributed normally across the traffic lanes so that the centerline saw more load repetitions than the outer portion of the traffic lane. The F-15 and C-17 load carts are configured to resemble the main landing gear configurations of their respective aircraft. While the F-15 consists of only a single tire main landing gear, where the left and right main gears are spaced approximately 2.75-m apart, the C-17 landing gear configuration is more complex. Figure 3.9 shows the landing gear configuration of the C-17 nose and main gears. The approximate tire pressures for the F-15 and C-17 are 2.25 MPa and 0.98 MPa, respectively, and their tire contact areas are 700 cm^2 and 2,040 cm^2, respectively.

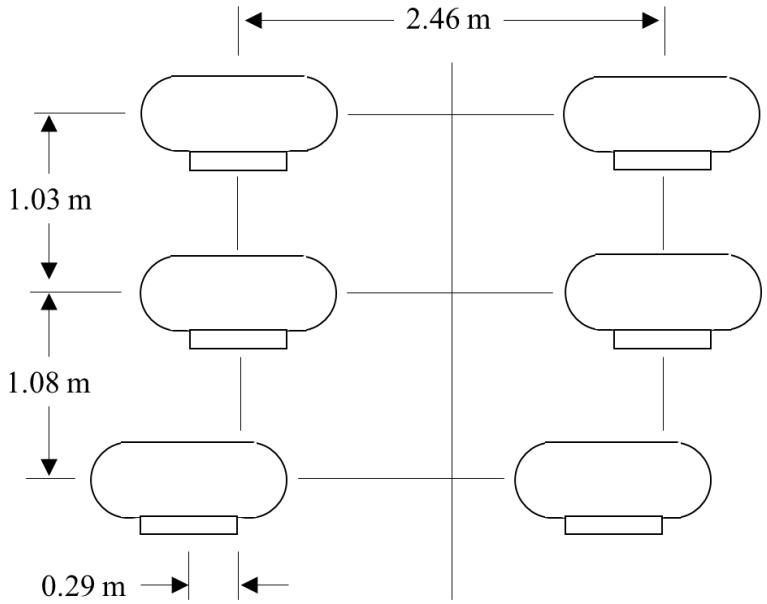

Figure 3.9 C-17A Globemaster III main landing gear configuration.

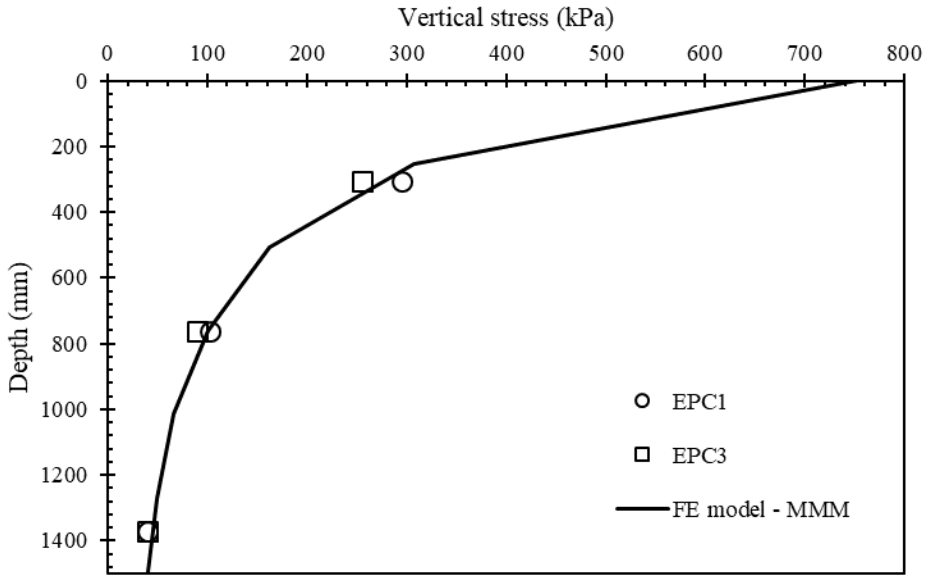

(a)

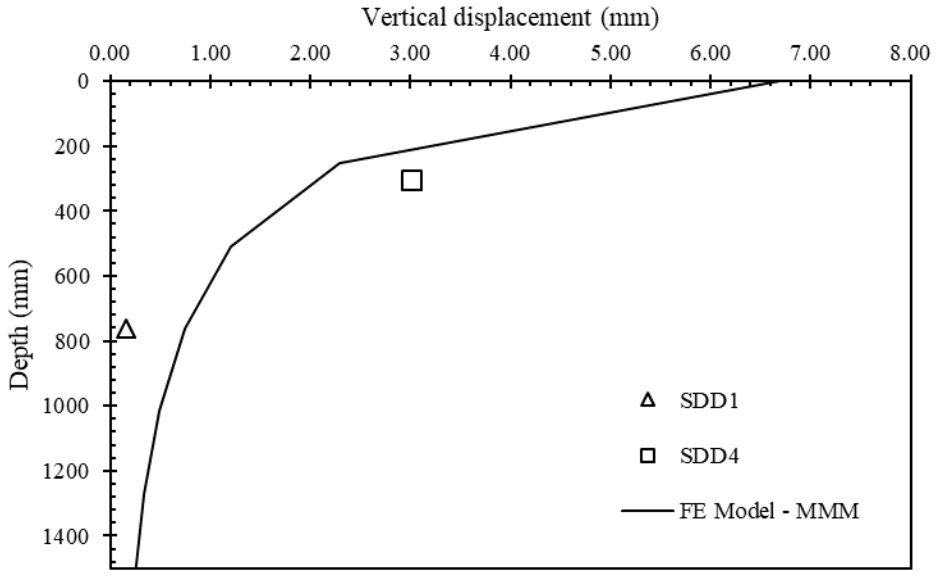

(b)

Figure 3.10 Comparison of simulation results from the FE model (with a jointed mat over elastoplastic subgrade modeled with MMM with unbonded interface) versus measured values from full-scale instrumented testing for F-15 loading: (a) vertical stress, (b) vertical displacement.

The rutting failure criteria are defined for the F-15 and C-17 by the Tri-Services (Air Force, Army, and Navy). The Tri-Services published a Capabilities Development Document (2004) that dictates 31.8-mm of permanent deformation in the soil support beneath the mat for an F-15 is considered a rutting failure, whereas 76.2-mm of permanent deformation is considered a rutting failure for a C-17.

Figure 3.10 graphically depicts the 3D-FE results with respect to the EPC and SDD test data. The FE vertical stresses with depth match very well with the EPC test data after the first pass over the instrumentation. While the SDD test data shows a little more scatter, there is still reasonable agreement in the displacements rendered by the FE model and the SDD-measured displacements. While the FE model and measured test data for vertical stress response are virtually identical, there is good reason to believe that the SDD at 762-mm depth was not working properly. The same field test was conducted on 10 CBR CH subgrade by Rushing et al. (2008) with SDDs at approximately 305-mm and 610-mm depth. The 305-mm SDD test data is relatively close to the 305-mm SDD test in the 6 CBR field test, but the 610-mm SDD test data is noticeably greater than the corresponding 6 CBR test (i.e., 0.79-mm to 0.15-mm, respectively). Similarly, the corresponding 15 CBR CH subgrade field test conducted by Rushing and Mason (2008) showed that the 305-mm SDD test data was relatively close to the corresponding 6 CBR field test, but again the 610-mm SDD registered 0.788-mm. The FE model gives approximately 1.02-mm vertical displacement at 610-mm depth and about 0.75-mm vertical displacement at 762-mm for the 6 CBR simulation. Therefore, it is reasonable to assume that the SDD at 762-mm in the 6 CBR field test was malfunctioning and that the FE model appears to be predicting reasonable vertical displacements at these depths.

3.5 Sensitivity Studies

A series of sensitivity studies on different variables are conducted to highlight their relative impact on subgrade response. The first study compares two different aircraft loads and gear configurations consisting of the single-wheeled main gear of the F-15E Eagle and the multi-wheeled main gear of the C-17A Globemaster III. A second study shows the influence of the variation in cover material stiffness and thickness on the subgrade response. A third study is conducted on modeling the mat as a continuous medium-thick plate versus modeling the mat as interconnected with hinge connector elements. The final parametric study is done on modeling the mat-soil interface as fully-bonded (no-slip) and unbonded (full-slip).

The last two parametric studies address unique aspects of the mat problem that are not well understood or documented – namely, the effects of modeling the mat as a jointed system and modeling the soil-mat interface conditions. While asphalt and unbound granular layers are typically modeled as a fully bonded interface, this is not the case with a mat-soil interface. Furthermore, while the load transfer occurring within concrete slabs from either dowels or aggregate shear interlocking is well documented, not much is known concerning the load transfer mechanisms occurring at the joints of airfield mats and its subsequent effect on subgrade deformation. These parametric studies are not seeking to resolve these issues, since this requires significant field testing. Instead, the parametric studies are intended to highlight the relative differences in subgrade response that can inform the design of future field investigations.

3.5.1 Aircraft Gross Weight and Gear Configuration

The effect of different landing gear configurations is investigated with respect to the FE models for the F-15 and C-17 aircraft.

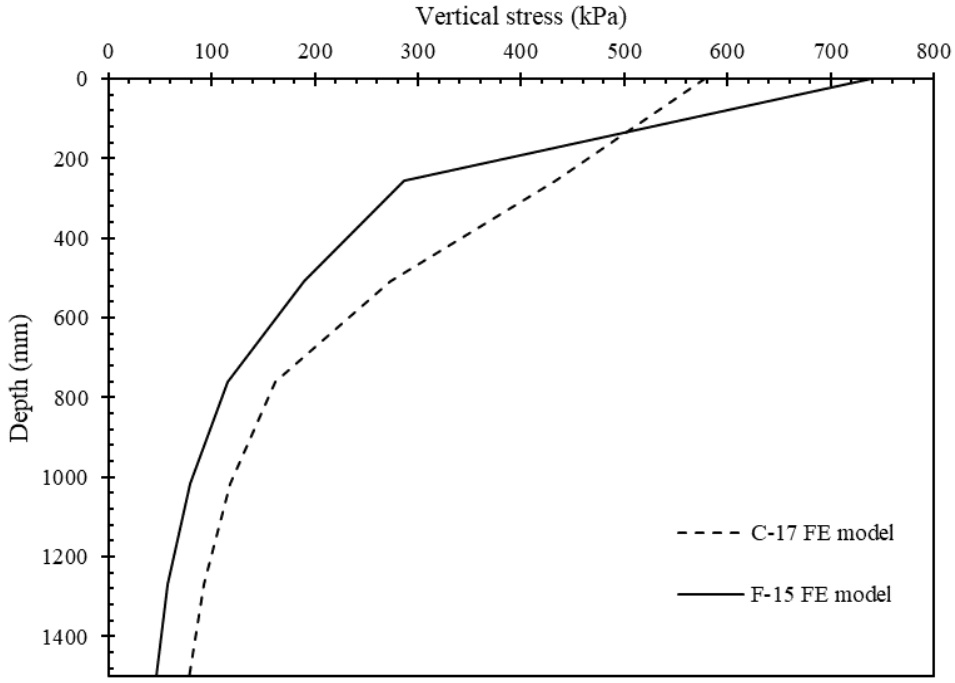

(a)

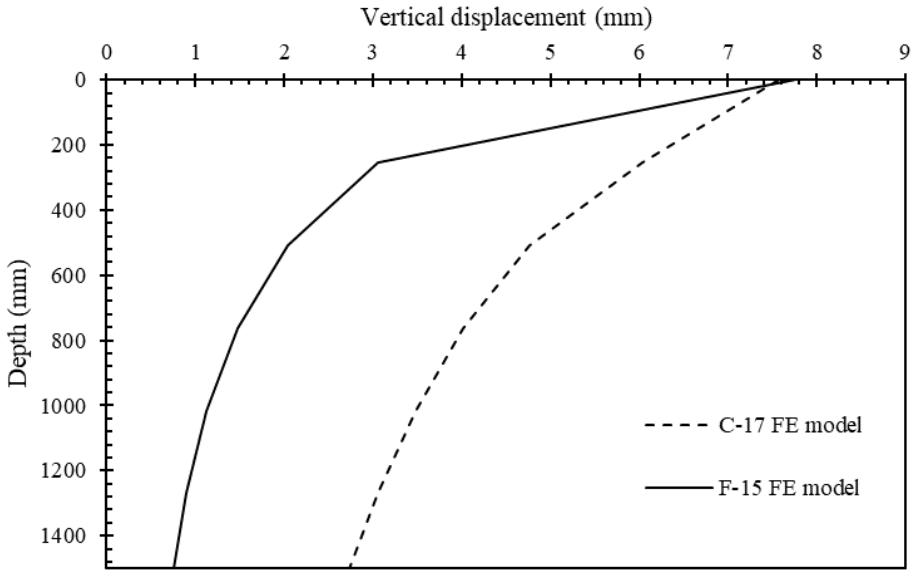

(b)

Figure 3.11 Results from the FE model with a plate model over elastic subgrade with unbonded interface for F-15 and C-17 loadings: (a) vertical stress, (b) vertical displacement.

Figure 3.11(a) shows the comparison between the vertical stress responses of the single wheel and multi-wheel load with depth from the F-15 and C-17, respectively. Figure 3.11(b) shows the displacement comparisons between the two landing gear types. While the F-15 has a higher vertical stress response near the surface of the subgrade, the C-17 gross weight coupled with the load distribution from multiple tires renders both a higher vertical stress response and larger displacements with depth. These factors are further investigated in the parametric studies dealing with cover material thickness and stiffness.

3.5.2 Cover Material Thickness and Stiffness

The influence of varying the cover material stiffness and thickness is investigated with respect to the concepts of subgrade response and cumulative damage. First, a series of LEA are conducted with *WinJULEA* on both the C-17 and F-15 main landing gear configurations over cover material thicknesses ranging from 152-mm to 1,524-mm. Figure 3.12 shows the layered elastic results for both the C-17 and F-15. As the cover material increases, the aircrafts' influence on subgrade deformation response decreases.

Next, a set of LEA is conducted in *PCASE* to study the effects of varying the cover material thickness with respect to cumulative damage. One of the shortcomings of typical LEA programs like *WinJULEA* and *KENLAYER* is the axisymmetric solution's constraint of circular loaded areas. An important difference between these LEA algorithms and *PCASE* is that *PCASE* implements an integration scheme to incorporate elliptical tire shapes, which can be important when feeding computed stresses or strains into performance models for determining cumulative damage.

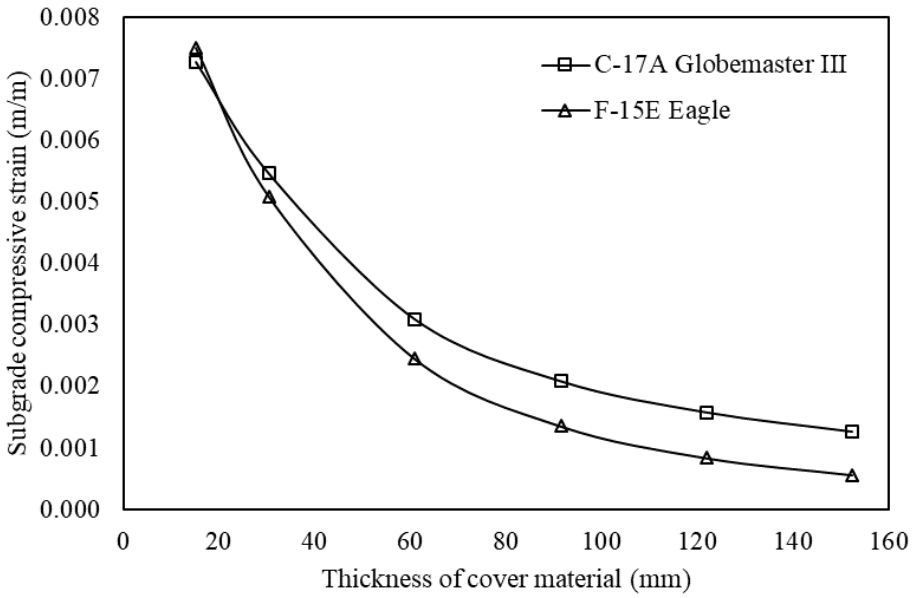

Figure 3.12 Subgrade compressive strains versus the thickness of cover material for C-17 and F-15 loadings.

The cumulative damage model in *PCASE* is based on Miner's fatigue hypothesis (1945), where the cumulative damage factor (CDF) represents a summation of each aircraft's and season's contribution to the overall life consumed in the pavement structure. It is represented by the following Equation (3.10):

$$CDF = \sum_{i=1}^{NAC} \sum_{j=1}^{NS} \frac{n_{ij}}{N_{ij}} \tag{3.10}$$

where the two summations are over the different aircraft in the traffic mix (as a function of landing gear configuration lending to effective stress repetitions) and the different seasons (which affect the modulus values) in the analysis, n_{ij} is the actual number of stress repetitions accumulated, and N_{ij} is the total fatigue life of the structure governed by a performance model. In design the sum of the ratios for all the aircraft in each season should be unity. The

performance model used to calculate the service life of the structure is the AM2 distress model proposed by Stache et al. (2019a), shown below:

$$N = 10^{\left(\frac{16.368-\frac{\sigma_{d,max}}{CBR}}{3.913}\right)} \tag{3.11}$$

where $\sigma_{d,max}$ is the maximum deviator stress calculated in the subgrade layer, CBR is the California Bearing Ratio of the subgrade, and *N* is the predicted service life (in coverages) of the structure. Figure 3.13 shows the CDF curves for a typical AM2 mat section over a CH subgrade (E = 56 MPa) where the engineered cover material thicknesses are varied (E = 345 MPa). Plot (a) in the figure shows the CDF curves for a relatively thin cover material (t = 152 mm), whereas the proceeding plots show the effects of incrementally increasing the thickness. The last plot (d) shows the approximate design thickness where the CDF ≈ 1.0. When the cover material thickness is relatively thin, the F-15's high tire pressures control the damage done to the subgrade, despite it having a significantly lower gross weight than the C-17. But as the cover material thicknesses increase, it is clear that the C-17 becomes the predominant aircraft controlling the design.

In Figure 3.14 the stiffness of the cover material is adjusted. As opposed to plot (a) of Figure 3.13, the presence of the cover material leads to the significantly heavier gross weight and wide load distribution of the C-17 as the controlling factors in the damage computation, irrespective of the stiffness of the cover material. Plot (d) highlights the design principle that increasing the stiffness of the cover material reduces the required thickness compared to the similar design in plot (d) of Figure 3.13, where the C-17 controls both designs.

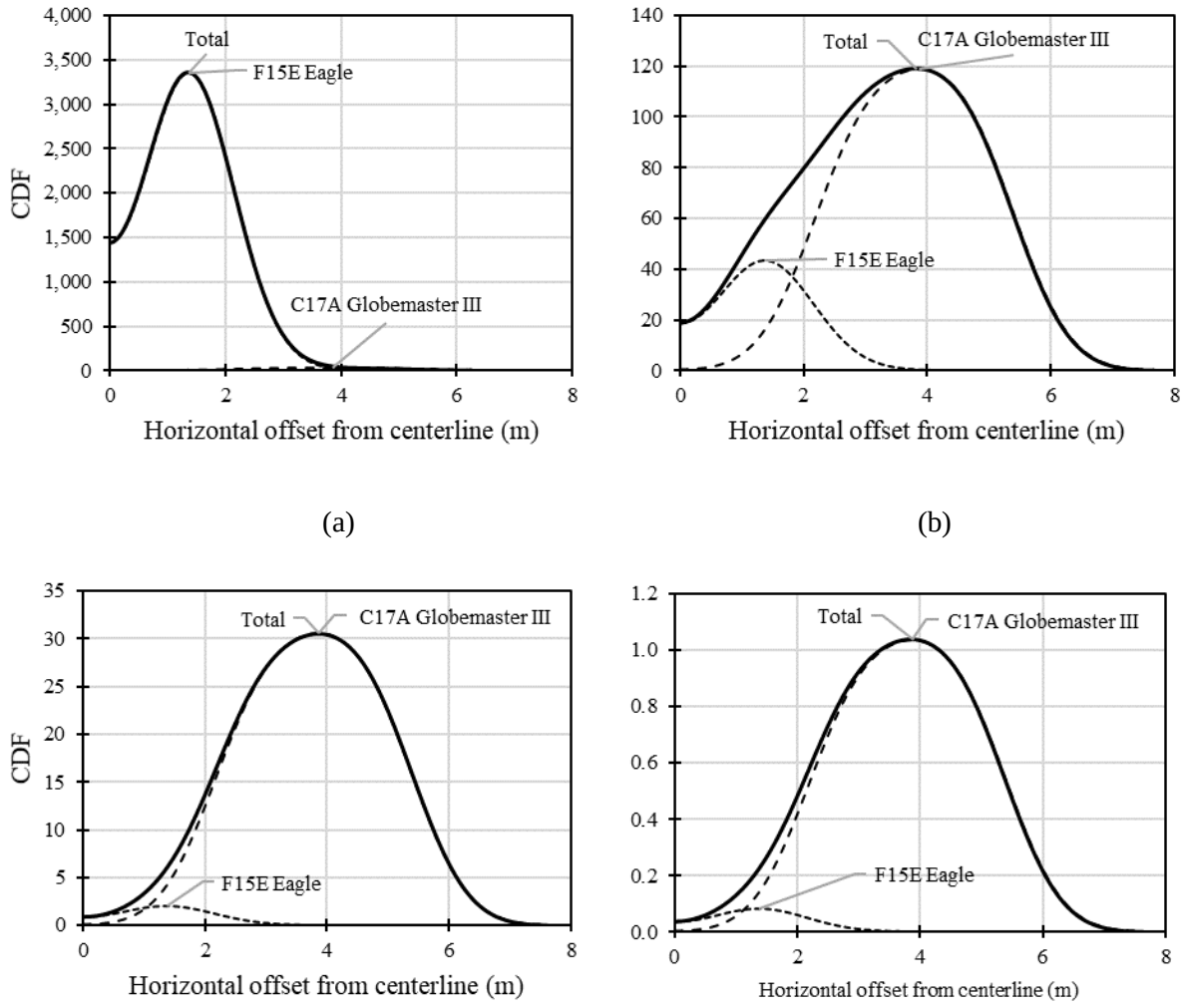

Figure 3.13 Cumulative damage curves for different thicknesses of cover material (E = 345 MPa) between an AM2 mat and subgrade for a traffic mix consisting of C-17 and F-15 aircraft: (a) t = 152 mm, (b) t = 254 mm, (c) t = 610 mm, and (d) t = 813 mm for a CDF ≈ 1.0.

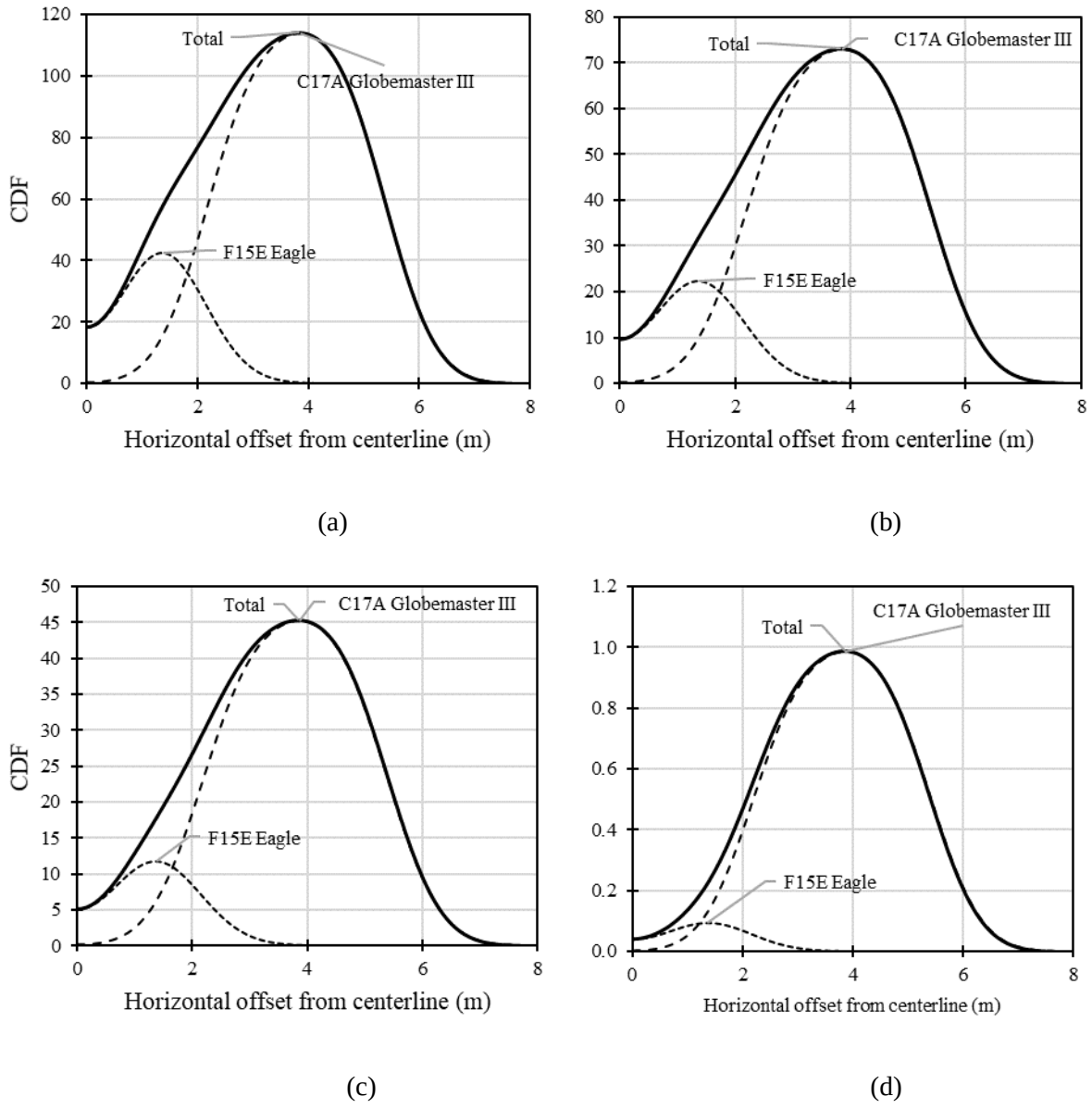

Figure 3.14 Cumulative damage curves for a cover material of t = 200 mm with varying stiffnesses between an AM2 mat and subgrade for a traffic mix consisting of C-17 and F-15 aircraft: (a) E = 175 MPa, (b) E = 690 MPa, (c) E = 1,034 MPa, and (d) E = 1,034 MPa with a CDF = 1.0 (t = 590 mm).

An important interpretive lens to use when analyzing these two sets of damage analyses is that the AM2 mat is used in *expeditionary* airfields, typically constructed over existing

(unprepared) subgrades. Due to both time constraints and limited access to high quality construction materials, mat structures either consist of thin marginal cover materials or none at all. Consequently, the plot (a) scenario in Figure 3.13 communicates the more likely conclusion – i.e., early rutting failures in expeditionary airfields made with AM2 mats are controlled by the high contact pressures of the F-15 or similar aircraft. Furthermore, similar to Figure 3.1, Figure 3.13 and Figure 3.14 reiterate the unique geotechnical challenge posed by the mat-soil interaction problem. Whereas typical flexible pavement structures are designed to fail at depth in the subgrade as opposed to the higher quality base or subbase layers, the proximity of the failure experienced in a typical mat structure is quite different. Rutting failures will most likely originate near the surface just below the mat, whether the mat is placed with a cover material, as is the case in the examples given in Figure 3.13 and Figure 3.14, or simply over an existing subgrade.

3.5.3 Mat as Continuous and Jointed Systems

The first parametric study investigated the effect of modeling the airfield mat system as a continuous plate structure versus a jointed system of interlocking mats. Figure 3.15 shows the results of modeling the mat structure as a continuous plate and as a jointed system. The jointed system renders a larger vertical stress response at the subgrade surface, while the continuous plate model is larger with depth. A similar result occurs with respect to the deformation response plot. While the jointed system transfers a slightly higher load near the subgrade surface, the effects of the F-15 main gear load are felt deeper in the subgrade due to the continuous plate modeling approach. This depth difference is important when considering the rutting failure mechanism in mats, since it has already been established above that rutting failures in mat structures most often occur near the surface, regardless of whether a cover material is used or not.

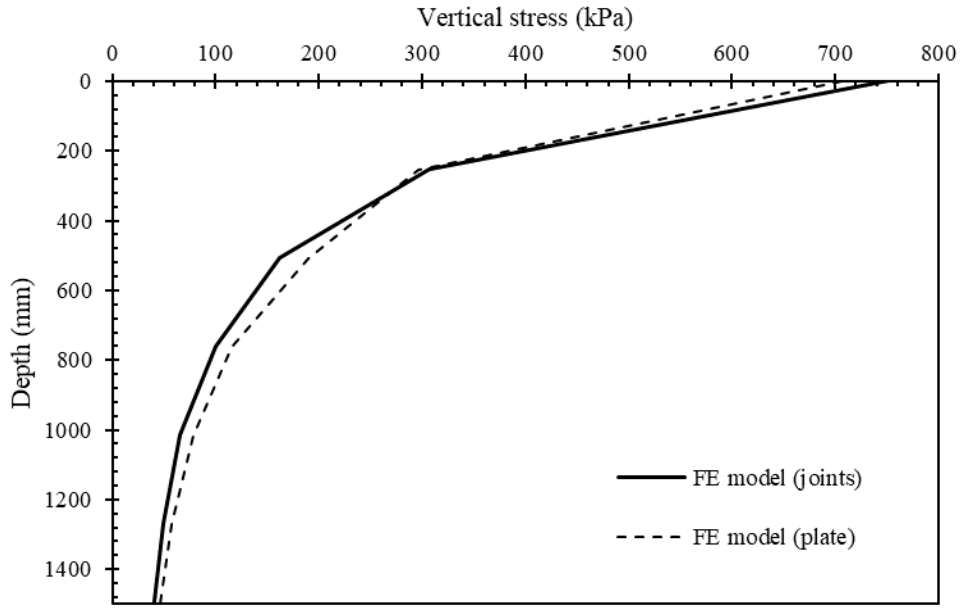

(a)

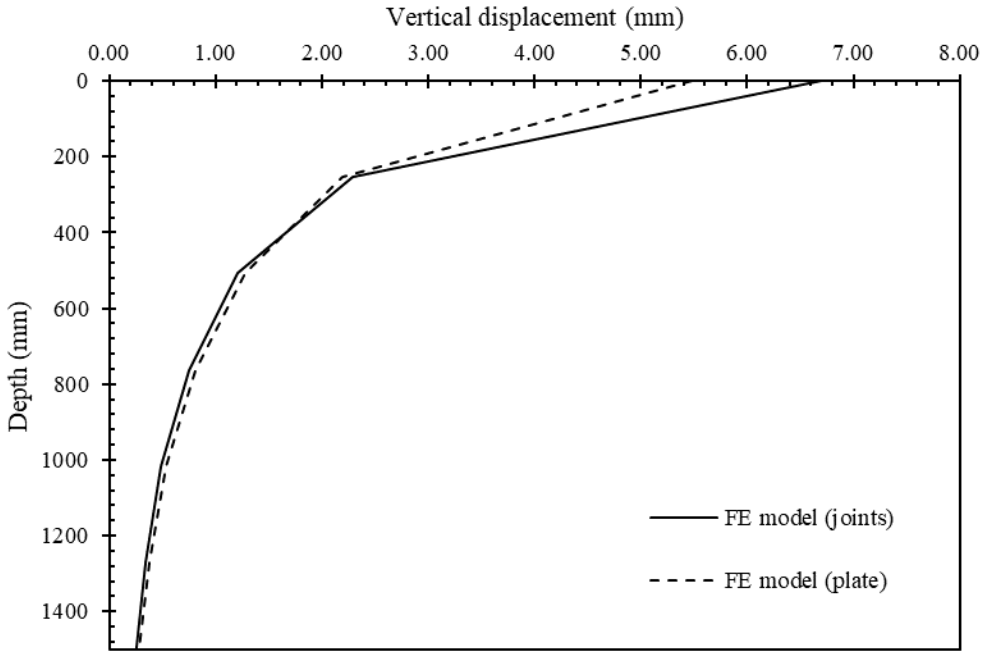

(b)

Figure 3.15 Comparison between the FE results obtained from the jointed and plate modeling approaches where the MMM is used for the subgrade and unbonded interface: (a) vertical stress, (b) vertical displacement.

3.5.4 Mat-Soil Interface Conditions

The last parametric study investigated the effect of modeling the interface conditions between the bottom of the airfield mat and the top of the subgrade as a fully bonded interface versus an unbonded interface. In reality, this interface condition is somewhere in between, where some friction is mobilized between the mat and soil that is a function of the roughness of the bottom of the mat and the type of unbound material beneath, similar to the adhesion principles assumed in retaining walls for cohesive materials. Comparative studies have been conducted in flexible pavement structures where the effects of bond condition in the unbound layers on distresses and performance were determined (Kruntcheva et al., 2005, Hu and Walubita, 2010). But since a field-testing study for airfield mat systems of this nature has yet to be conducted, the purpose here is to simply take note of the implications of the two modeling approaches.

Figure 3.16 shows the results of the two modeling approaches in terms of vertical stress and deformation where the jointed system modeling approach is shown with linear elastic material properties used for the subgrade layer. Figure 3.17 shows the results of the two modeling approaches in terms of vertical stress and deformation where the jointed system modeling approach is shown with the MMM used for the subgrade layer. Interestingly, while Figure 3.16 renders what is expected from corresponding calculations in LEA solutions where the frictional (fully bonded) interface results in a slightly higher stress and deformation response in the subgrade, Figure 3.17 shows that using the MMM as the subgrade results in higher responses in the unbonded interface condition. On the other hand, Figure 3.18 shows the results from the same simulations as Figure 3.17 except the mats were modeled as a continuous plate rather than a jointed system. In the case of the continuous plate approach, the vertical stress and displacement for a fully bonded condition were slightly higher than the unbonded scenario.

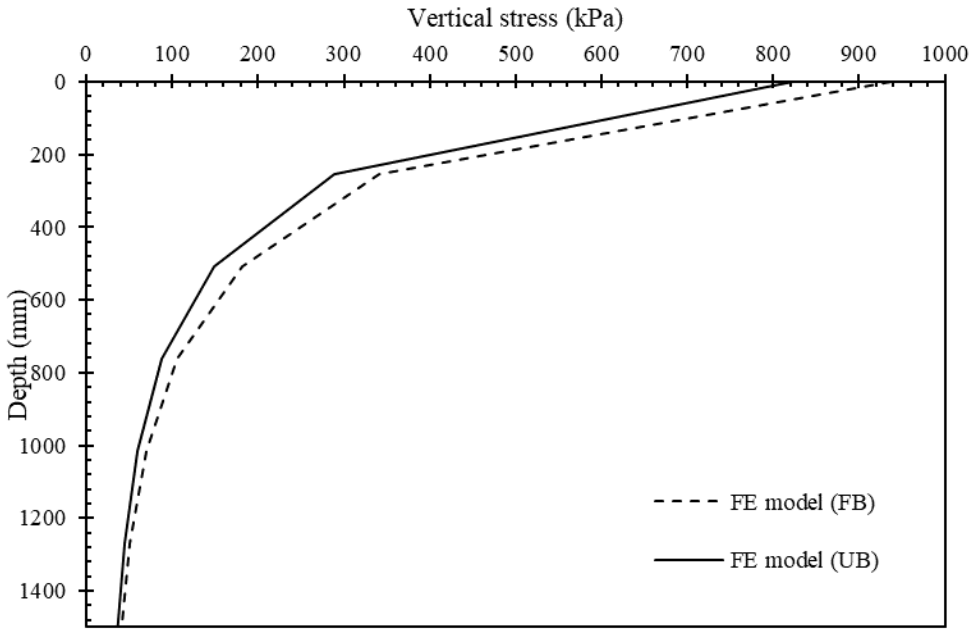

(a)

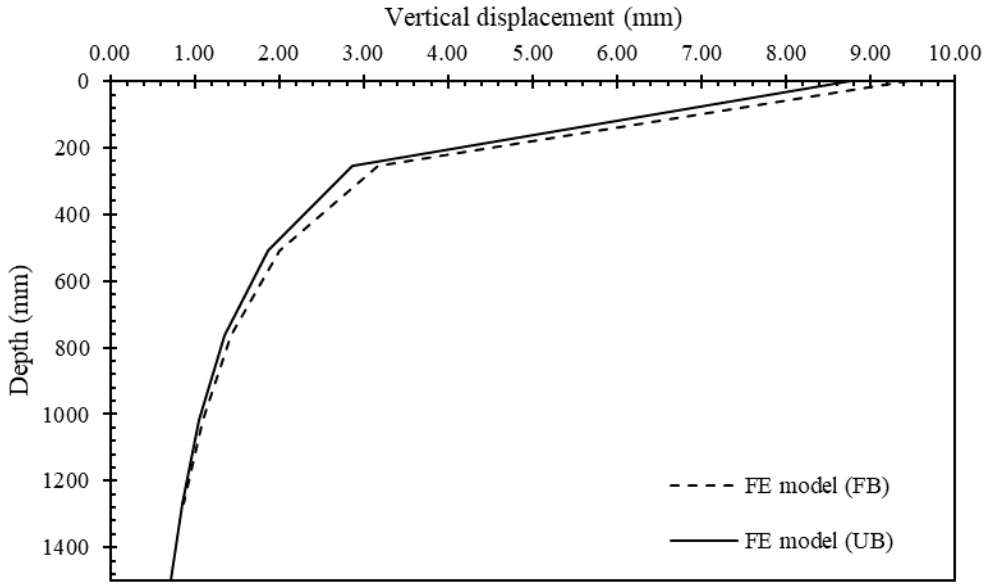

(b)

Figure 3.16 Comparison between the fully bonded ("FB") and unbonded ("UB") modeling approaches using an elastic subgrade and jointed mat system: (a) vertical stress, (b) vertical displacement.

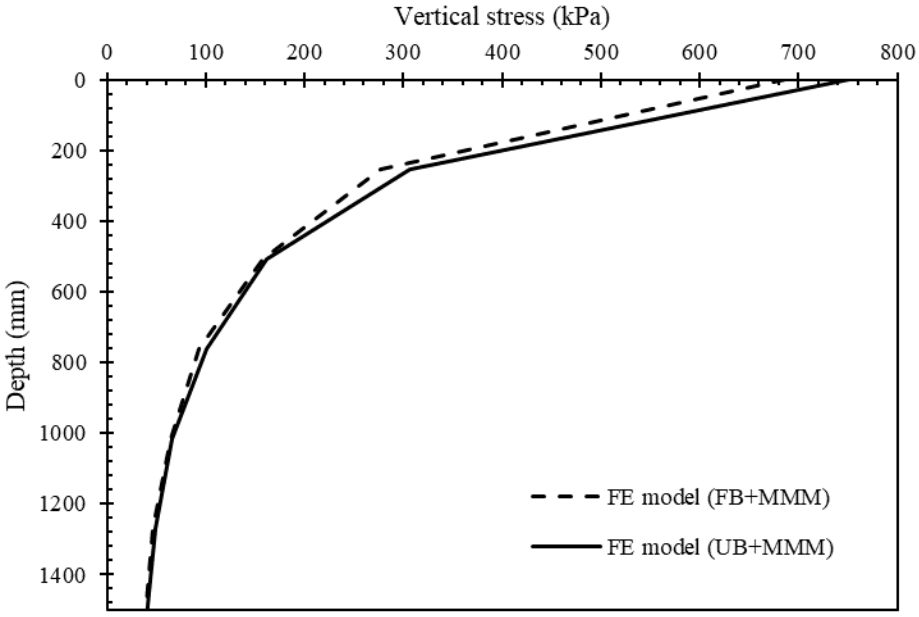

(a)

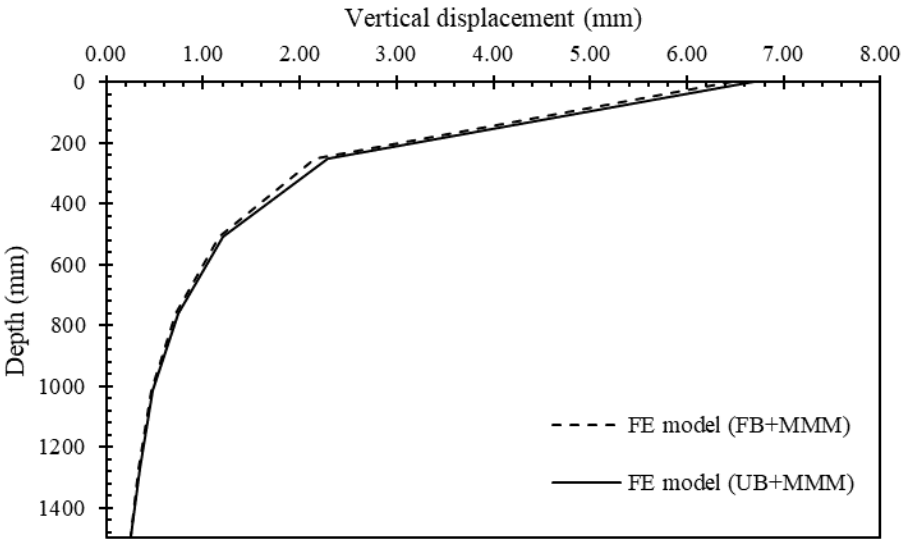

(b)

Figure 3.17 Comparison between the fully bonded ("FB") and unbonded ("UB") modeling approaches where the MMM is used to represent subgrade response and the mats are modeled as a jointed system: (a) vertical stress, (b) vertical displacement.

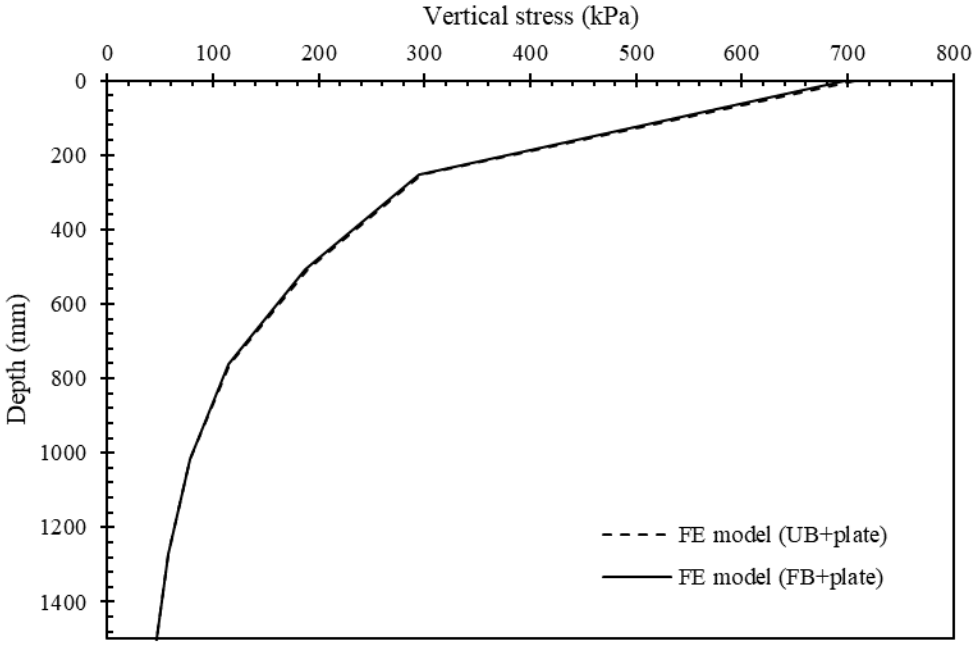

(a)

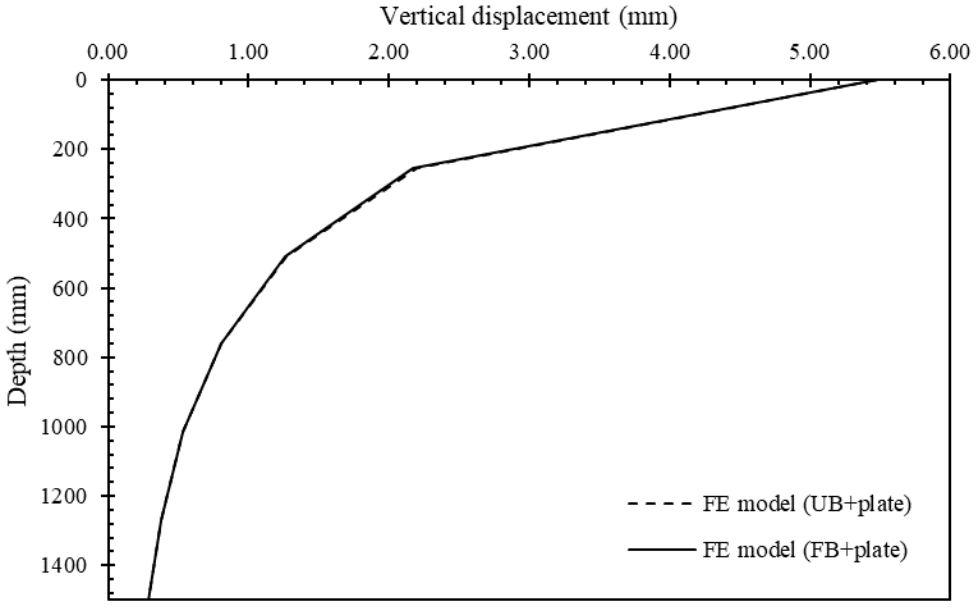

(b)

Figure 3.18 Comparison between the fully bonded ("FB") and unbonded ("UB") modeling approaches where the MMM is used to represent subgrade response and the mat is modeled as a continuous plate: (a) vertical stress, (b) vertical displacement.

There are multiple variables at play in these different figures. Modeling the airfield mats with joints results in higher stress and deformation responses near the surface. On the other hand, differences in response due to variations in the interface conditions are related to the mobilization of shear stress in a fully bonded condition and the variation in the orientation of the principal stress axes in the full slip (no friction) condition.

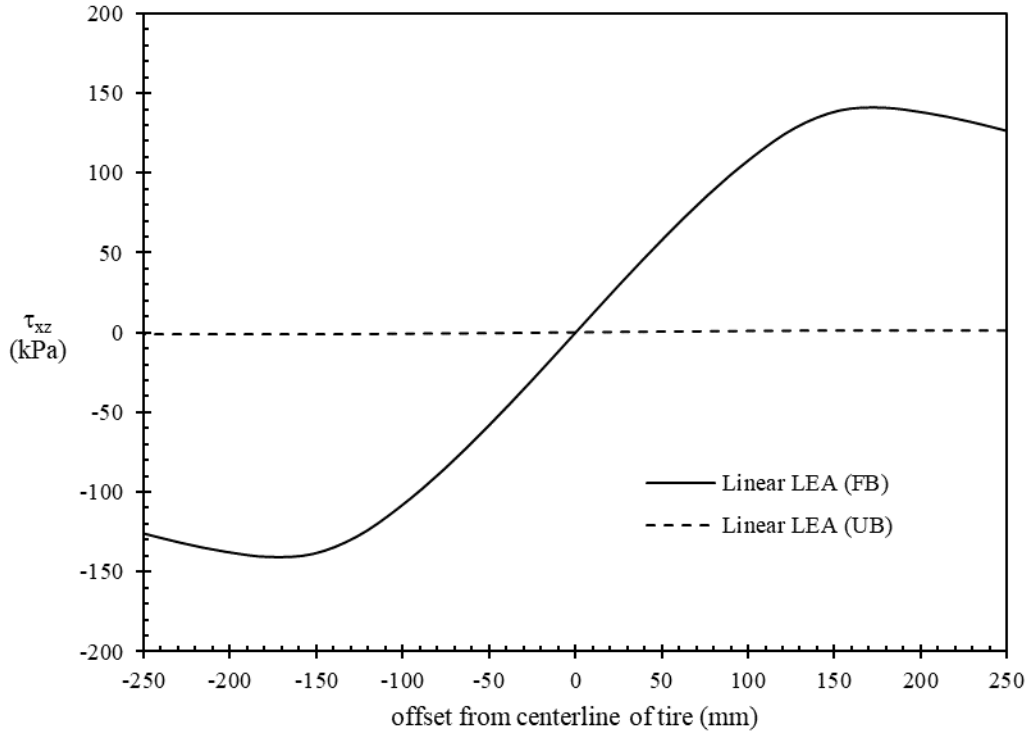

Figure 3.19 Comparison between the shear stress mobilized at the soil-mat interface during fully bonded ("FB") and unbonded ("UB") interface conditions in linear LEA using *WinJULEA*.

Figure 3.19 shows that significantly more shear stress is mobilized in the *xz*-plane along the soil-mat interface at the top of the subgrade during a fully bonded condition compared to a full-slip condition. Figure 3.20 highlights the variation in the orientation of the principal stress

axes at the top of the subgrade during a full-slip condition compared to a fully bonded condition. Figure 3.21 illustrates the effect of changing the interface condition between the subgrade and mat with respect to orientation of the principal stress axes and mobilization of shear stress at the soil-mat interface. Because of the shear stress mobilized at the soil-mat interface, the fully-bonded condition results in a reduction in the confinement stresses σ_x and σ_y with a corresponding increase in σ_z. On the other hand, the full-slip condition results in higher values of σ_x and σ_y with a corresponding decrease in σ_z. Finally, there is also the difference between modeling the subgrade as a linear elastic material compared to a nonlinear, elastic-plastic material, where the stress-strain relationships for the two material models can produce different responses.

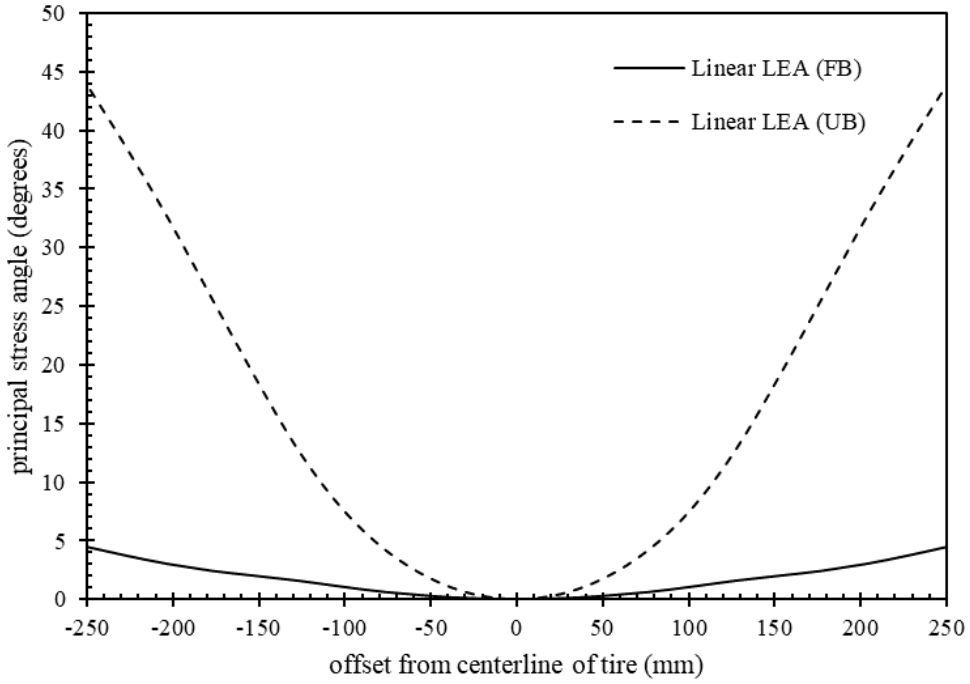

Figure 3.20 Comparison of the variation of principal stress axes orientation at the soil-mat interface for fully bonded ("FB") and unbonded ("UB") interface conditions in linear LEA using *WinJULEA*.

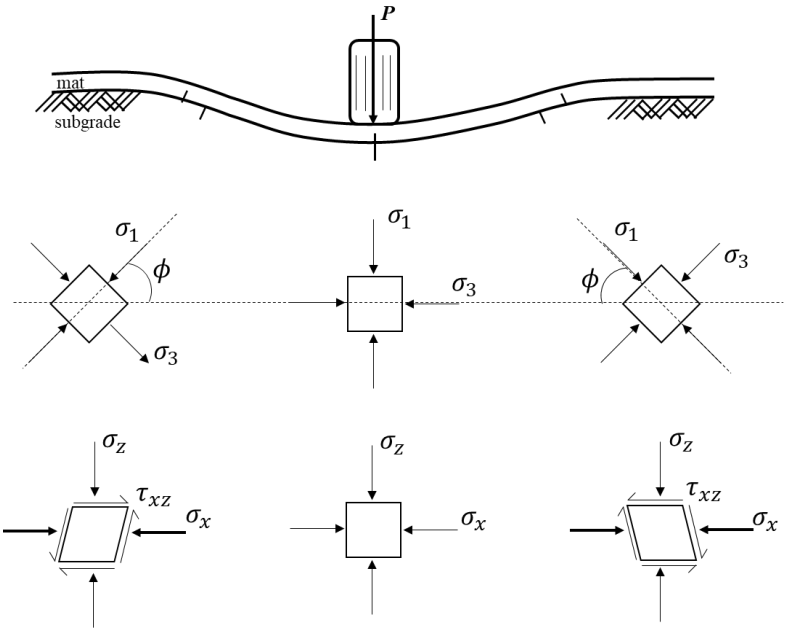

(a)

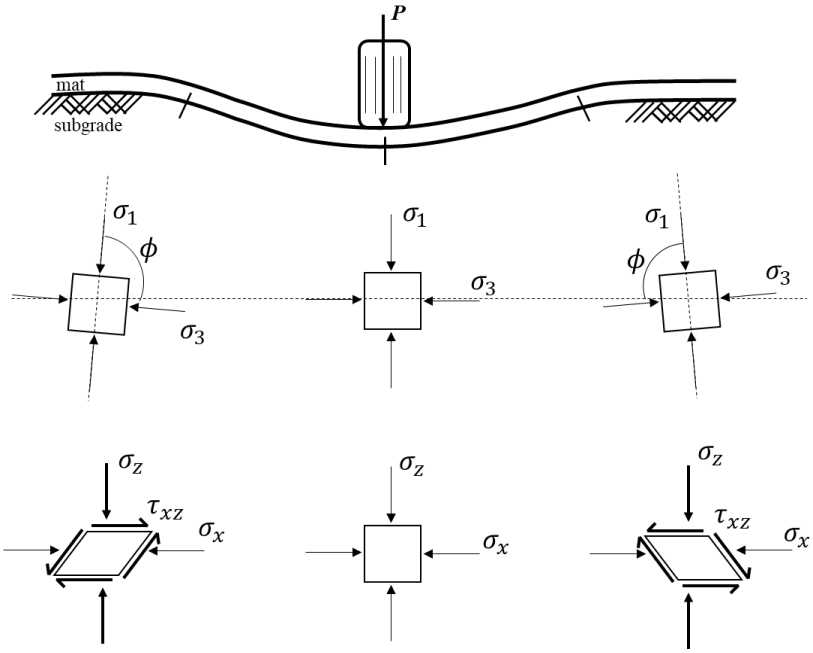

(b)

Figure 3.21 Comparison between (a) unbonded and (b) fully bonded interface conditions with respect to variation of the principal stress axes and mobilization of shear stress at the soil-mat interface. Bold arrows signify an increase with respect to the other interface condition.

CHAPTER IV

EFFECTS OF PRINCIPAL STRESS ROTATIONS AND EXCESS PORE-WATER PRESSURE CHANGES ON SOFT SUBGRADE DEFORMATION OF AIRFIELD MAT STRUCTURES UNDER PSEUDO-DYNAMIC LOADING

This chapter has been submitted for review and possible publication in a scholarly journal. The paper is currently under peer review process while this dissertation has been written. This chapter has been reformatted and replicated herein with minor modifications in order to outfit the purposes of this dissertation.

4.1 Introduction and Background

Matting systems such as the AM2 are used to construct expedient airfields during deployed military operations. Airfield mats are emplaced when equipment and manpower are limited, logistics are challenging, and the quality of engineered materials are marginal (Gartrell, 2007). Consequently, AM2-surfaced airfields are typically emplaced over relatively soft material, where rutting is the predominant failure mechanism (e.g., Rushing and Tingle, 2007; Stache et al., 2019a). Critical factors such as aircraft gear load and tire pressure, joint load transfer, and subgrade conditions are important in predicting the deformation response in both typical and expedient pavement structures. However, an often overlooked factor contributing significantly to airfield subgrade deformation is repeated loading coupled with aircraft wander. This loading condition results in complex stress histories in the supporting subgrade with

variation in the principal stress axis orientation. Conventional predictions of pavement performance are conducted using a mechanistic-empirical modeling approach (Gonzalez et al., 2012; Clausen et al., 1977; Shook et al., 1982). If a finite element (FE) modeling approach is employed, it is typically conducted with a pulsating cyclic load in two-dimensional (2D)-axisymmetric space (Rushing et al., 2015).

In the broader pavements and geotechnical engineering community, the effects of principal stress rotation due to repeated loading on the accumulation of plastic strains and permanent subgrade deformation have been well documented (e.g., Chan and Brown, 1994; Lekarp and Dawson, 1998; Inam et al., 2012; Jeffries et al., 2015; Gallage et al., 2016). These studies concentrate primarily on replicating observed field behavior with laboratory testing to highlight the importance of principal stress rotations on the accumulation of plastic strains in pavement subgrades. Willis et al. (2006) and Johnson et al. (2007) implemented a FE model using a time-staggered series of tire imprints approach for their investigations of the expanding influence of plastic strains in the subgrade due to aircraft wander. Although this finding is important, the role of principal stress rotations in the development and expanding influence of the plastic subgrade strains was not highlighted in either study.

In the smaller expedient airfield matting community, there has been significant field testing of the AM2 and other matting technologies dating back to the 1960s (e.g., Thompson and Burns, 1960; Burns and Fenwick, 1966; Ulery and Wolf, 1971). More recent military testing and evaluation efforts of the AM2 mat systems include the Rapid Parking Ramp Expansion Program (Rushing and Tingle, 2007; Rushing et al., 2008; Rushing and Mason, 2008; Garcia et al., 2014a, 2014b), which were used in the development of a new proposed mechanistic-empirical mat performance criteria (Stache et al., 2019a). These studies and many other investigations not

mentioned here were primarily used in identifying the different failure mechanisms that occur in mat systems and in developing lighter expeditionary surfaces with thinner profiles, lower densities, and improved welding technologies. Numerical analyses, on the other hand, are much less prevalent. Foster (2007) simulated a foam webcore mat system using an isotropic elastic material model for the subgrade with infinite elements as a part of the AM-X program. Leski et al. (2012) modeled a mobile, composite airfield mat with an elastic subgrade material model to confirm field-testing results. Finally, Doyle et al. (2012) conducted FE analysis on various mat systems using the Drucker-Prager constitutive material model for the subgrade and made comparisons with earth pressure cell (EPC) data from several test sections. It is important to note that whereas Foster (2007) and Leski et al. (2012) focused on mat response, Doyle et al. (2012) looked at subgrade stress response under monotonic loading. Along with other structural factors, it was shown in Chapter 3 that the mat-soil interface bonding condition and the load transfer occurring at the mat joints affect the subgrade response under statically loaded AM2 mats (Stache et al., 2019c).

As a tire moves laterally and longitudinally across the mat surface, the direction of the shear stresses reverse in the subgrade. The reversal of the shear stress direction corresponds to a rotation of the principal stress axis orientation and inevitably contributes to rutting in the subgrade (Chan and Brown, 1994). In a 2D-axisymmetric FE simulation, a cyclic load can be applied but there is minimal rotation of the principal stresses since the load does not move from its original point of application. A full three-dimensional (3D)-FE model must be developed that simulates aircraft trafficking with wander to accurately capture any significant variation in the principal stress axis orientation. Furthermore, the constitutive model for the subgrade must be capable of capturing the resulting complex stress histories from the moving loading condition.

Since rutting is the predominant failure mechanism for airfield mats constructed over soft subgrades, it is important to quantify the role of principal stress rotations resulting from aircraft trafficking and wander. However, this critical aspect has been overlooked in the majority, if not all, of the previous studies. To address this issue, the main objective of this study is to properly investigate the effect of rotation of the principal stress axes and variations in excess pore-water pressures on the soft subgrade deformation of the AM2 matting system under repeated, wandering aircraft traffic. For this purpose, we conduct a pseudo-dynamic FE analysis where traffic wander is incorporated into the numerical model to highlight its contribution to the development of deformation in the existing soft subgrade. The soft subgrade is modeled by implementing the MMM, a user-defined elasto-plastic kinematic hardening model capable of modeling the soil behavior under repeated loadings and complex stress histories. The FE modeling results are compared against those attained from a set of full-scale testing program reported by Rushing and Tingle (2007).

4.2 Finite Element Modeling

4.2.1 Geometry

In this study, we numerically simulate the AM2 mat system using the commercial FE software *ABAQUS* (*ABAQUS*, 2017). A continuous, medium thick plate FE model is used to represent the AM2 mat response. While the effects of mat joint load transfer can affect the near surface subgrade response, it is reasonable to model the mat as a continuous plate if the areas of concern are with depth in the subgrade (Stache et al., 2019c). Since conducting a pseudo-dynamic FE analysis of this nature requires extensive computational effort, attempts are made to optimize the size of the model. The vertical extents of the subgrade mesh were determined analytically through FE sensitivity testing.

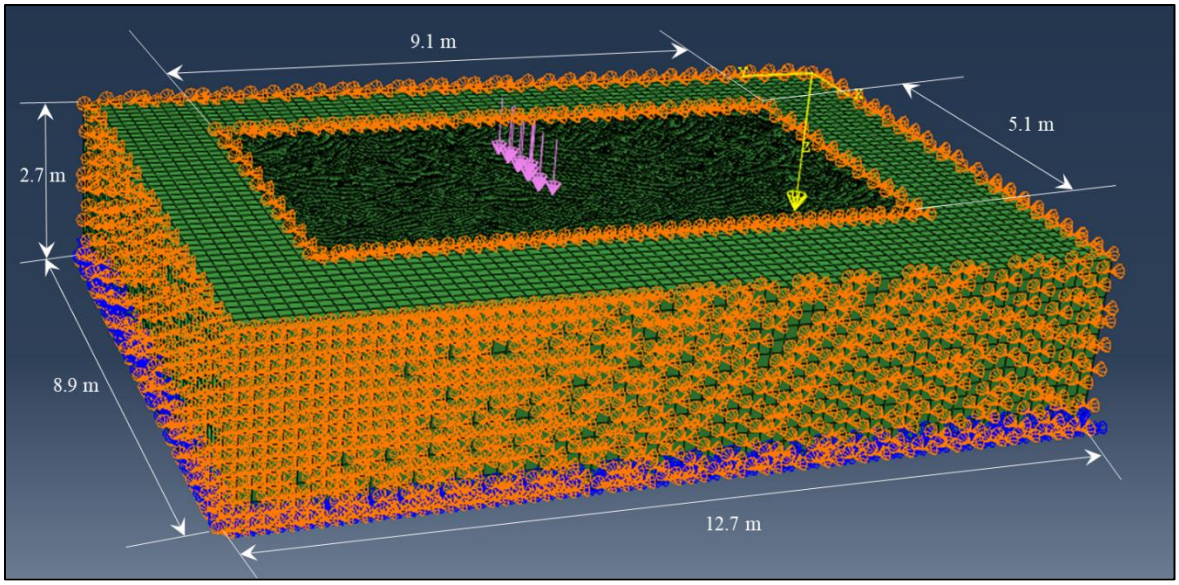

Figure 4.1 Three-dimensional FE model of the mat on subgrade used in the study with the loading condition along the traffic lane for the first and second passes, FE mesh, boundary conditions, and geometric dimensions.

The analytical approach implemented is similar to that used by Ioannides and Donnelly (1991), where the influence of the vertical extent boundary conditions on subgrade response was minimized as a function of the mat's radius of relative stiffness, *l*. The radius of relative stiffness for a plate supported by an elastic spring foundation can be computed as:

$$l = \sqrt[4]{\frac{Eh^3}{12(1-v^2)k}} \tag{4.1}$$

where E corresponds to the composite mat modulus of elasticity, h is the mat thickness, v is the mat Poisson's ratio and k is the modulus of subgrade reaction. The model dimensions were optimized based on a set of sensitivity analyses to make sure the selected boundaries have no artificial effects on results. The optimum height was determined to be 10*l*, or about 2.7 m. As noted by Ioannides and Donnelly (1991), the displacement does not converge to a constant value due to the presence of lateral boundaries at the mat edges. This effect is mitigated by extending

the lateral boundaries beyond 7*l*. As shown in Figure 4.1, the model dimensions include 12.7 m (length), 8.9 m (width), and 2.7 m (height).

4.2.2 Constitutive Models

There have been a number of methods for approximating or "back-calculating" the modulus of elasticity of the composite AM2 mat (e.g., Doyle et al., 2012; Rushing and Howard, 2018). Gonzalez and Rushing (2010) conducted a back-calculation of the modulus of elasticity using a simply supported three-point bending test. FE simulations were conducted where deflection basins were matched using the measured flexural rigidities from the test while adjusting the modulus of elasticity using the Mindlin plate solution (1951). Equation (3.1) was used to iterate upon the modulus of elasticity values in the FE model. Full-scale testing of the AM2 shows that the mat has an elastic response at low levels of stress repetitions, regardless of the subgrade stiffness. As such, it is appropriate for this study to assume the AM2 mat can be characterized by only the back-calculated composite modulus and Poisson's ratio.

To simulate the subgrade response, the MMM is defined and implemented as a user-defined material model (UMAT) in *ABAQUS*. The MMM is an elasto-plastic kinematic hardening model recently developed by Stache et al. (2019b) (presented in Chapter 2). The use of the MMM is motivated by its ability to capture plastic strain under complex loading, as demonstrated by Stache et al. (2019b), that would not be predicted by traditional yield-surfaces models with isotropic hardening. Interested readers are referred to Chapter 2 for further details regarding the underlying theory, formulations, calibration, and validation of the MMM against various laboratory test data. It is noted that Stache et al. (2019c) (see Chapter 3) used the MMM to study the main factors in subgrade rutting failures of the AM2 mat systems over soft soils under static loading. The main differences between the current study and Stache et al. (2019c)

can be summarized as follows: Stache et al. (2019c) showed that the soil-mat interface bonding condition and the load transfer occurring in the mat joints contributed to the subgrade deformation response under static loading. This study focuses on the role of principal stress rotation induced by traffic wander on subgrade deformation and pore-water pressure response under pseudo-dynamic loading.

In this study, we numerically model Buckshot clay, a high plasticity clay (CH) from Vicksburg, MS, to represent a soft subgrade. The soil was tested during the full-scale testing program reported by Rushing and Tingle (2007), which is used for FE model development and validation purposes in the current study. Table 3.2 shows the average density and moisture contents on the full-scale test section repartee by Rushing and Tingle (2007). Since the average densities and water contents for the Buckshot clay from Table 3.2 result in a degree of saturation exceeding 90%, a fully-saturated assumption for the subgrade was made corresponding to the calibrated MMM parameters found in Stache et al. (2019c). Table 3.3 and Table 3.4 detail all the material and geometric properties used in the FE model when comparing against the full-scale instrumented test data.

4.2.3 Boundary Conditions, Mesh, and Loadings

The lateral extents and bottom of the subgrade are pinned. The mat system is also pinned, which corresponds to the anchoring system in full-scale testing. Both the mat and subgrade are modeled with 8-noded brick elements (C3D8). Contact pairs were implemented in *ABAQUS* to define the contact at the mat-subgrade interface. The tangential behavior was defined as a frictionless full-slip condition, where the mat was allowed to slide freely over the soil. The normal behavior was defined by a classical Langrage multiplier hard contact pressure-

overclosure relationship, where contact pressures are fully transmitted between the mat and soil surfaces once they are in contact.

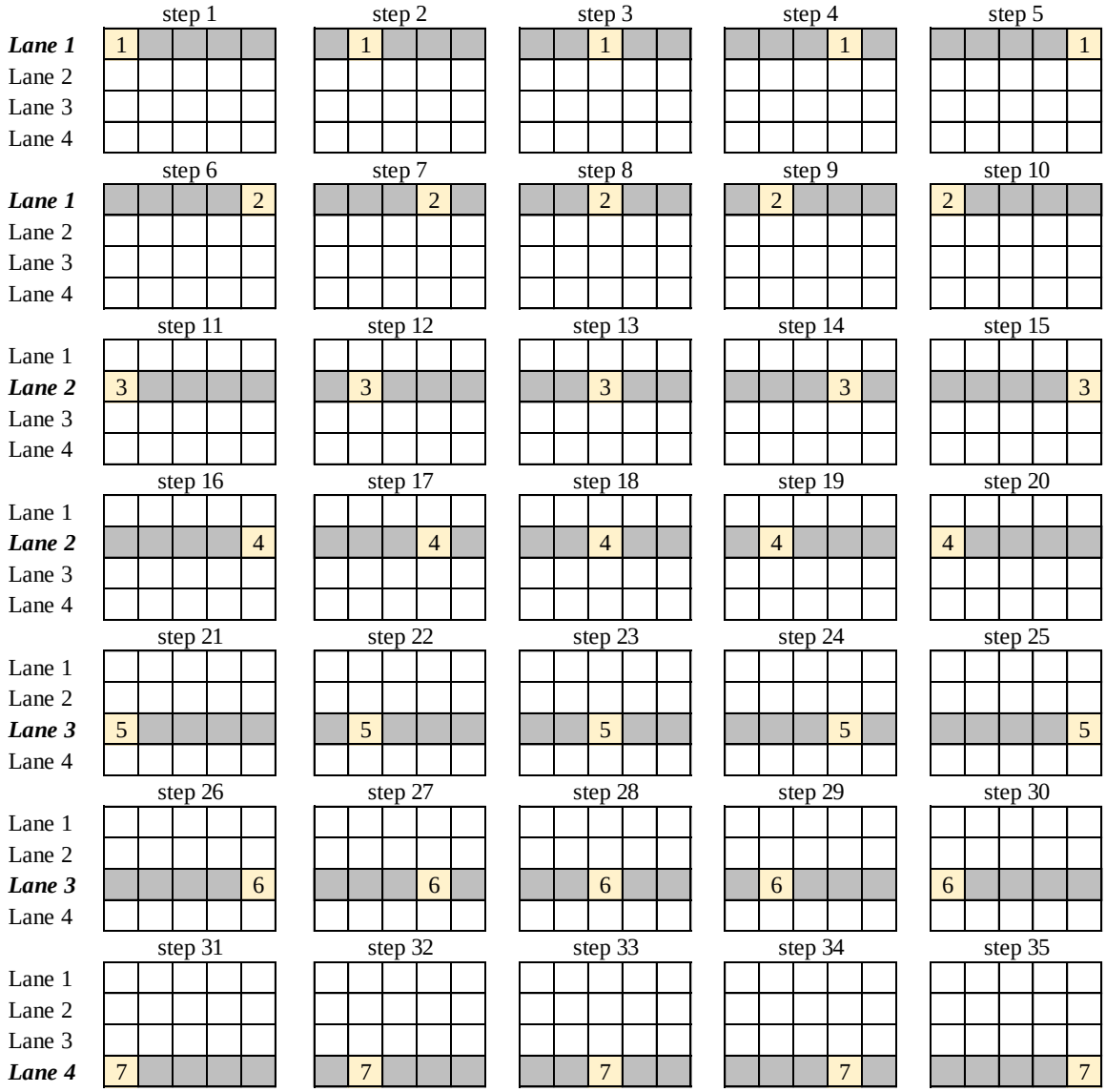

Figure 4.2 Time-stepping procedure for simulating moving tire. Greyed areas signify the trafficked lane in that step. Tanned boxes represent the location of the tire imprint during the step, where the number corresponds to the pass number.

The near surface subgrade response is greatly affected by the mat-subgrade interface condition, as noted by Stache et al. (2019c). Modeling the interface as fully-bonded causes a mobilization of the shear stresses, while modeling it as a full-slip condition induces larger near surface principal stress rotations. The actual mat-subgrade interface condition is not well understood and probably somewhere in between these two extremes (Stache et al., 2019c). For the purposes of this study, a full-slip condition is assumed since lateral movement of the subgrade at the interface is certainly allowed during loading, and the interface condition has less influence at the subgrade depth of concern.

Similar loading conditions are implemented in the numerical model as those used in the Rapid Parking Ramp Expansion (RPRE) full-scale instrumented testing program (Rushing and Tingle, 2007), which will be further described later in this paper. The simulation of trafficking over the test section model is accomplished through a "pseudo-dynamic" approach using a series of time-staggered tire imprints. This approach is not truly dynamic as it does not consider inertial effects. This is a reasonable assumption, however, as inertial effects are negligible in a slow-moving load cart during full-scale testing. Each time-staggered tire imprint load is static and linearly ramped over each step in an implicit time integration scheme. A layout of the loading procedure for the seven passes across four traffic lanes is given in Figure 4.2. Throughout the simulation time history, the series of tire imprints serves as an approximation of the tire load moving across the mat section.

4.3 Comparison Against Full-Scale Test Data

The test data from the RPRE full-scale instrumented testing program (Rushing and Tingle, 2007) are used for validation of the FE model. The original purpose of the RPRE program was to establish performance metrics for a new lightweight airfield mat to replace the

traditional AM2 mat. The program consisted of the full-scale instrumented testing of the AM2 mat system over engineered fill with CBRs of 6, 10, 15, 25, and 100 under simulated F-15 and C-17 load carts. The six CBR test data (Rushing and Tingle, 2007) are used for comparison with the pseudo-dynamic FE model.

The geometric and weight properties for the AM2 mat are given in Table 3.1. Figure 3.4(b) and Figure 3.5(a) show the fully constructed test section and the F-15 load cart. The AM2 mat consists of a single aluminum extrusion with hinge-type male-female connectors. The adjacent (short) sides are joined by welded overlap-underlap connections secured with an aluminum locking bar. The extruded core consists of vertical stiffeners spaced apart in the long direction. An 18.3-m wide by 12.2-m long section of AM2 matting with two traffic lanes for the F-15 and C-17 load carts were placed over an 18.3-m wide by 12.2-m long by 0.9-m deep test section consisting of six CBR Buckshot clay.

The test section was instrumented with earth pressure cells (EPC) and single depth deflectometers (SDD) to measure the response of the soil support under the matting. Figure 3.8 shows the instrumentation layout for the F-15 test section. The AM2 mats were constructed in a brickwork (or staggered) lay pattern as seen in the fully constructed test section in Figure 3.4(b), where load cart trafficking occurred perpendicular to the long edge of the mat panels. The traffic lane for the F-15 test section was 1.5-m wide.

Following the work of Brown and Thompson (1973), the load cart traffic was distributed normally across the traffic lanes so that the centerline saw more load repetitions than the outer portion of the traffic lane. The F-15 load cart is configured to resemble the main landing gear configuration of the F-15E Eagle fighter aircraft. The approximate tire pressure and contact area

for the F-15 load cart corresponding to the maximum allowable F-15E takeoff configuration are 2.25 MPa and 700 cm^2, respectively.

Since Rushing and Tingle (2007) only published the maximum instrumentation values for each pass, these values were "converted" to the FE model time history in which the load cart pass occurred. Admittedly, this conversion produces unrealistically smooth test data plots, but it serves the purpose of comparing the *maximum* readings with the FE model results in the overlay of the simulation time history.

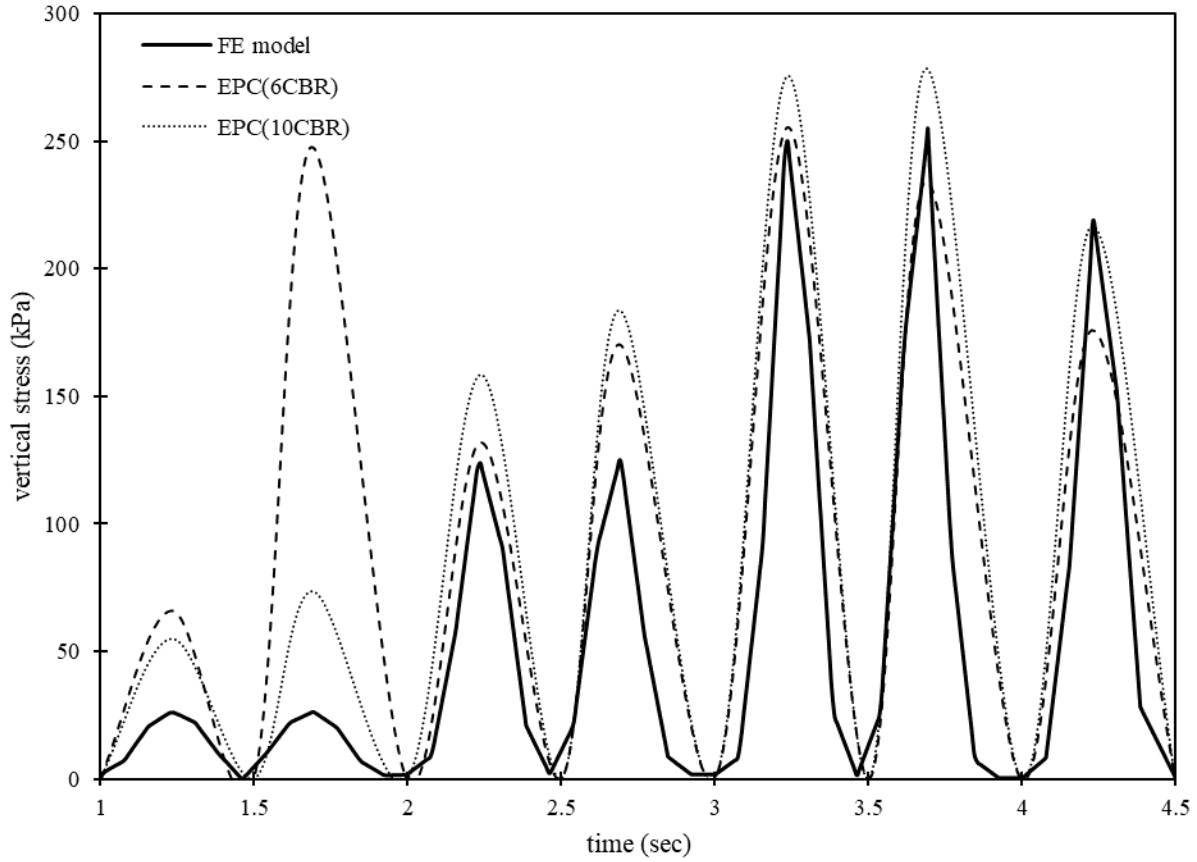

Figure 4.3 FE model vertical stress time history compared to EPC test data at 305 mm depth. Test data from 10 CBR testing highlights the anomalous 6 CBR response from 1.5-2.0 sec due to load cart driver error. The response should be similar to the previous reading at 1.0-1.5 sec.

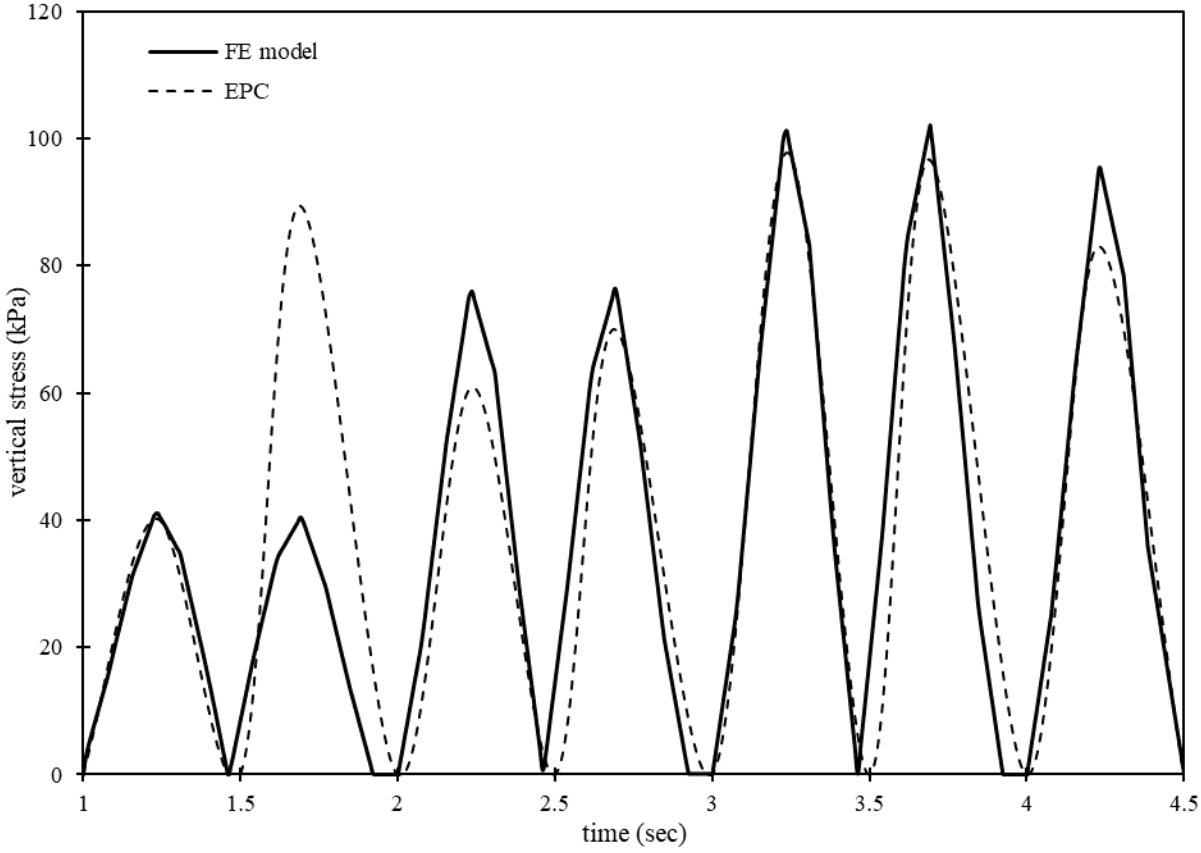

Figure 4.4 FE model vertical stress time history compared to EPC test data at 762 mm depth.

Figure 4.3 and Figure 4.4 graphically depict the 3D-FE time history results with respect to the EPC test data at 305-mm and 762-mm depths. Figure 4.5 graphically depicts the 3D-FE time history results with respect to the SDD test data at 305-mm depth. The SDDs at 762-mm depth did not seem to produce reasonable output throughout the duration of testing. Whereas the 762-mm SDDs during the 6 CBR testing remained around 0.003-mm (Rushing and Tingle, 2007), the corresponding SDDs during 10 and 15 CBR testing produced deformation output for the first 10 passes ranging from 0.3-mm to 0.8-mm under the same loading conditions (Rushing

et al., 2008; Rushing and Mason, 2008). For this reason, the 762-mm SDD test data can be reasonably excluded from comparison with the 3D-FE model.

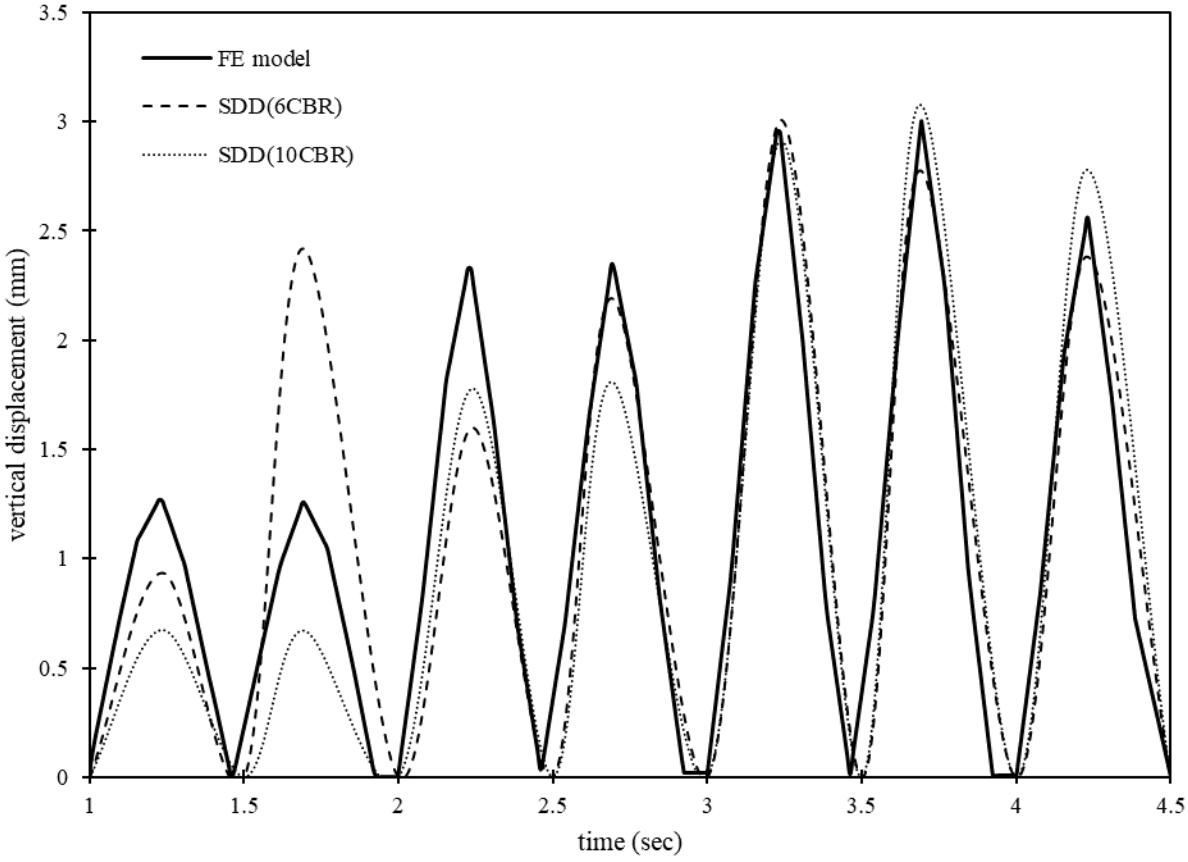

Figure 4.5 FE model vertical displacement time history versus SDD test data at 305 mm depth. Test data from 10 CBR testing highlights the anomalous 6 CBR response from 1.5-2.0 sec due to load cart driver error. The response should be similar to the previous reading at 1.0-1.5 sec.

With the exception of the second EPC and SDD pulses between 1.5 and 2.0 seconds in Figure 4.3, Figure 4.4, and Figure 4.5, the FE model response matches very well with the measured pressures and deflections. It is clear to see the simulated tire moving closer to the instrumentation location in the progression of the stress and deformation time histories. The

anomalous EPC and SDD pulse readings between 1.5 and 2.0 seconds are abnormally high, considering the tire is supposed to be located two traffic lanes from the instrumentation according to the traffic pattern. It is difficult to know with certainty how well the load cart driver remained within reasonable tolerances of the assigned horizontal offsets. Whereas the FE model simulation trafficking is exact, it is likely that there is some additional wandering of the load cart within and outside the specified lane. For example, it appears that the driver during testing misdirected the load cart during the second pass from the first lane into the second or third lane. As shown in Figure 4.3 and Figure 4.4, the corresponding test data at the same depth from the 10 CBR trafficking reveals that the EPC and SDD readings during the first and second passes should be similar since the load cart is trafficking at the same horizontal offset from the instrumentation (Rushing et al., 2008). Therefore, it is reasonable to say that the FE model is rendering appropriate stress and deformation responses during the second pass as well.

4.4 Results and Discussion

In the previous section, the FE model was shown to compare well with full-scale test data. The FE model is now used for further analyses on complex stress histories and rotation of principal stresses. Properly addressing the effects of repeated, wandering aircraft loads on subgrade deformation response requires modeling complex stress histories. Laboratory tests such as the cubical triaxial test and the directional shear test offer the ability to probe principal stress space and monitor the effects of principal stress axis rotation. It is important to note that laboratory testing such as the directional shear test and hollow cylinder apparatus are probably the best window for truly observing the effects of principal stress rotation (e.g., Arthur et al., 1980; Arthur et al., 1981; Ishihara and Towhata, 1983; Sture et al., 1987; Arthur et al., 1989; Alawaji et al., 1990; Gutierrez et al., 1991; Nakata et al., 1998).

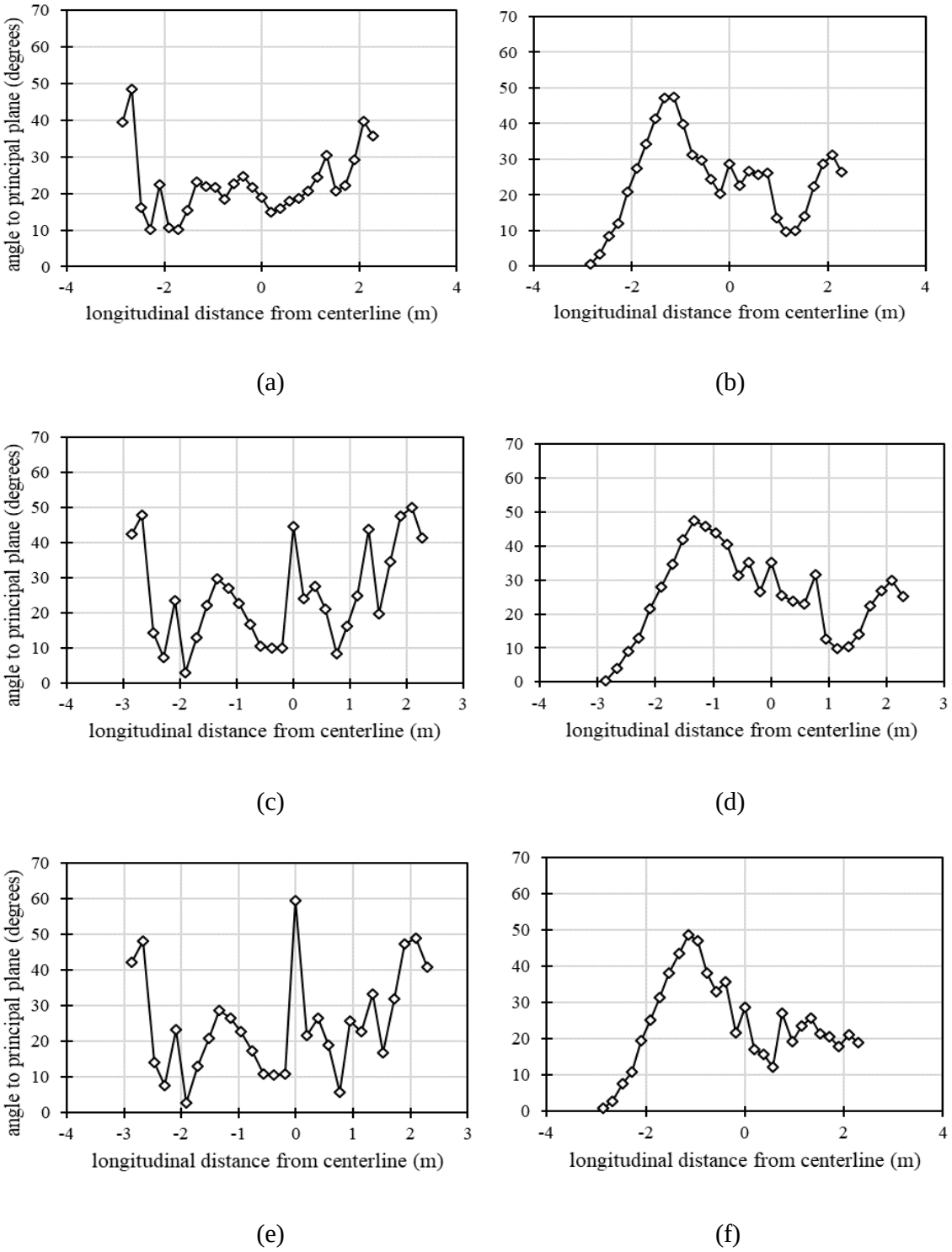

Figure 4.6 Rotation of principal stress axes along the third lane during the (a) 2nd, (b) 3rd, (c) 4th, (d) 5th, (e) 6th, and (f) 7th passes. For example, the orientation of the axes rotate from pass 2 (plot a) to pass 3 (plot b).

Such investigations contributed to a better understanding of flow theory, kinematic hardening, and stress-induced anisotropy with respect to principal stress rotation.

It is difficult to gather comparable test data on principal stress rotation in full-scale field testing. Whereas such laboratory tests provide significant insight into known field behavior, simulating traffic wander using a full 3D-FE model could yield promising results as well. While such a model cannot be fully validated in the absence of comparable field test data, using a 3D-FE modeling approach enables us to look at *relative* deformation response resulting from the introduction of principal stress axes rotations and variations in excess pore-water pressure.

Figure 4.6 shows the orientations of the principal stress axes along the third lane at different points during the time history. It is important to notice that with each successive pass of the simulated moving tire, there is a corresponding rotation of the principal stress axes along the length of the traffic lane. These rotations contribute to the deformation response and the variation of excess pore-water pressures. The simulation data from the remaining figures were extracted from the FE model at the same corresponding horizontal offsets in the third lane and 305-mm depth that the EPC and SDD instrumentation were located during full-scale testing.

Aircraft traffic wander produces complex stress paths that are unlike those in other engineering-related problems. The moving load produces what is referred to as a “heart-shaped” stress path in the subgrade. This phenomenon has been investigated experimentally using laboratory tests such as the hollow cylinder apparatus (Qian et al., 2016; Shi et al., 2018; Yang et al., 2019) and the cyclic torsional shear test (Guo et al., 2016). Figure 4.7 shows the heart-shaped stress paths in deviatoric stress space that form as a result of the stress reversals and the corresponding rotation of the principal stress axes in the 3D-FE simulation. As the tire moves longitudinally up and down a traffic lane, the torsional shear stress reverses. Furthermore, as the

tire moves laterally to the next lane it produces its own unique stress path. While each stress path maintains the characteristic heart-shaped plot, the size of the stress path changes as the tire wanders to the next lane closer in proximity to the node of interest. By way of comparison, the loading condition from a cyclic triaxial test varies only the stress difference $(\sigma_{33} - \sigma_{11})/2$ while the cyclic torsional shear test only varies the shear stress τ_{13} (Ishihara and Towhata, 1983). Consequently, the stress paths from each test are straight lines in the deviatoric stress space. Similarly, there is a short-coming in restricting a trafficking analysis on subgrade deformation to a 2D-axisymmetric FE model, since the principal stress rotations contributing to variations in excess pore-water pressure and subgrade deformation are absent from the simulation.

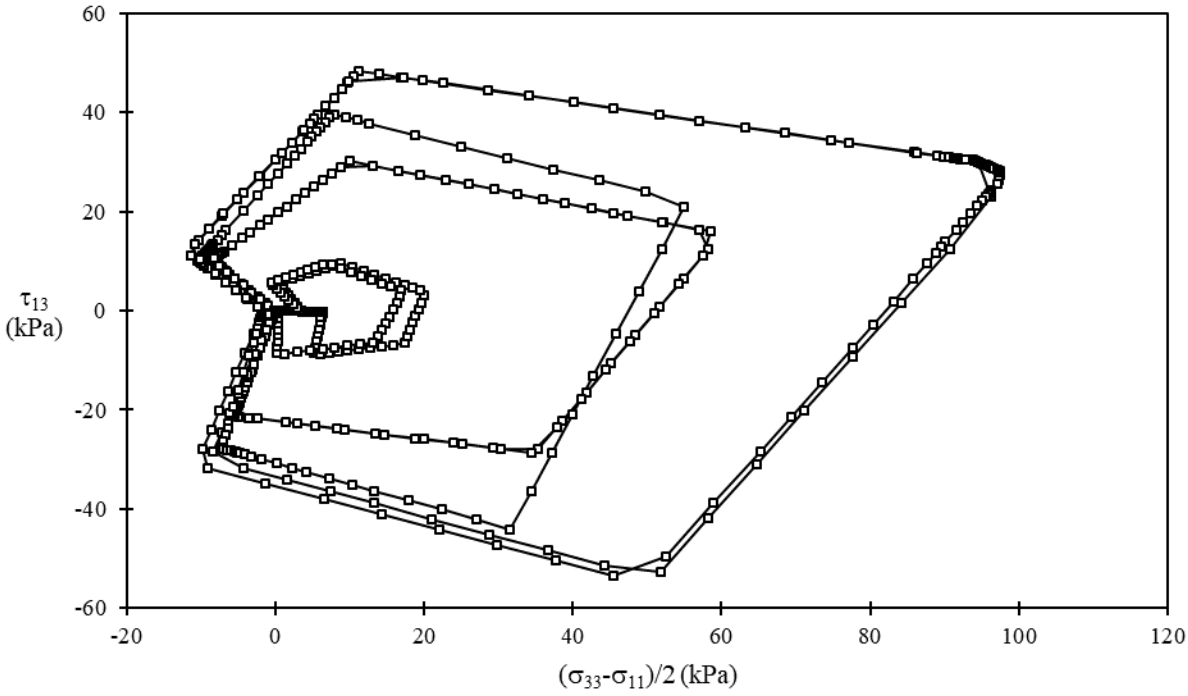

Figure 4.7 Complex heart-shaped stress paths at 305 mm depth as a result of aircraft traffic wander, plotted with respect to torsional shear stress τ_{13} and the stress difference $(\sigma_{33} - \sigma_{11})/2$.

The following plots make use of a time-like strain length parameter, ξ. Unlike strain, the strain length parameter is always positive and increasing. The parameter "stretches" out the hysteric plots to better view the variation throughout the time history. The strain length parameter can be computed as:

$$\xi = \sqrt{de_{11}^2 + de_{22}^2 + de_{33}^2} \tag{4.11}$$

where de_{11}, de_{22}, and de_{33} are the increments of deviatoric strains. Figure 4.8 shows the deviatoric stress plotted over the strain length, while Figure 4.9 shows the variation of the excess pore-water pressures.

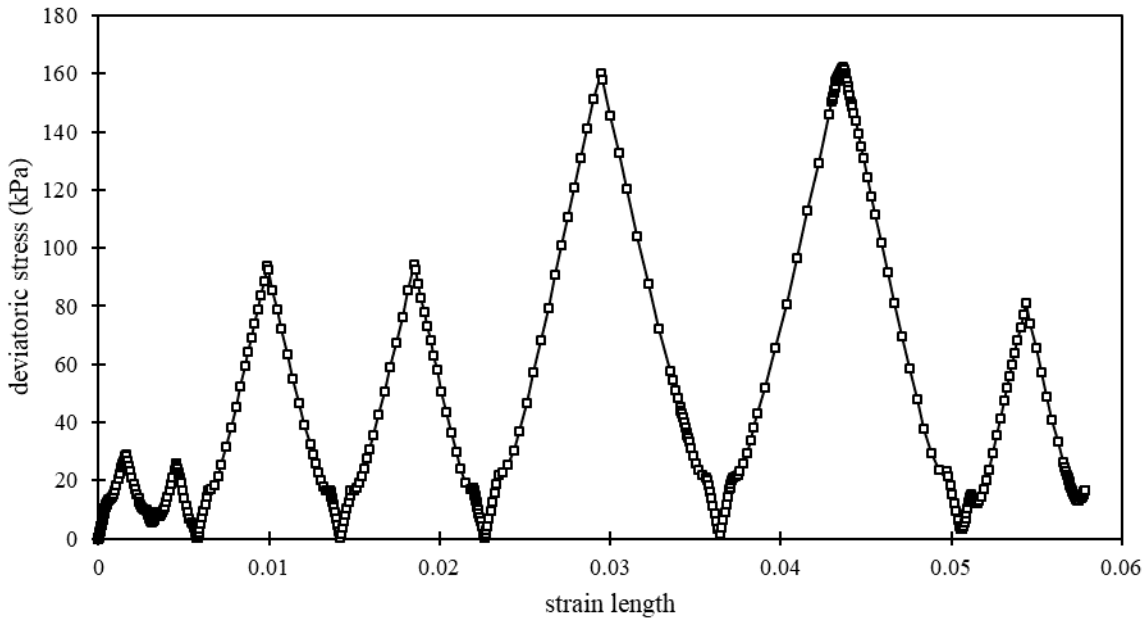

Figure 4.8 Variation of the deviatoric stress as a result of load wander with respect to the dimensionless strain length parameter at 305 mm depth.

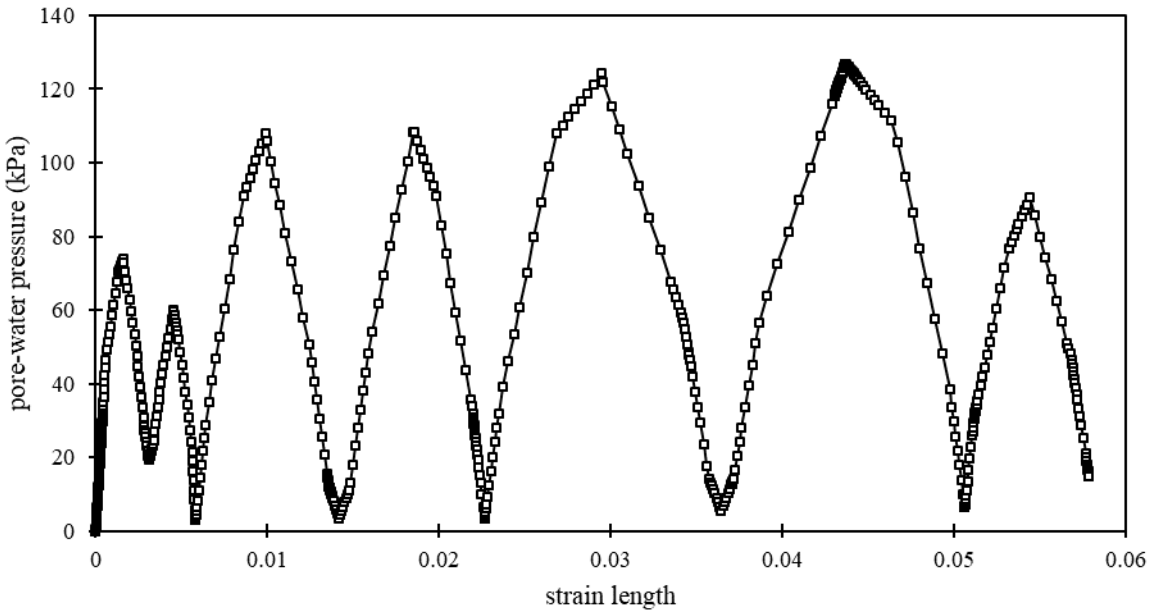

Figure 4.9 Variations in excess pore-water pressure due to load wander at 305 mm depth.

The shear stress is cycling up and down as a result of the moving tire across the different traffic lanes and the rotation of the principal stresses. Similarly, the excess pore-water pressure varies in accordance with the stress reversals. Furthermore, the magnitudes of the deviatoric stress and pore-water pressure increase as the simulated tire moves laterally across each lane closer to the node of interest. The total work W_T done on the subgrade as a result of the complex loading can be computed as:

$$W_T = \int \boldsymbol{\sigma}\dot{\boldsymbol{\varepsilon}}dt \tag{4.12}$$

where the total work is the product of the stress tensor and the strain rate tensor. The total work can be decomposed into its shear and hydrostatic components, where the contributions of distortion and volume change-related work are accounted for. In the MMM purely hydrostatic volume change is coupled with the volume change resulting from shearing in the shear-dilatancy

relationship of Equation (4.10). Figure 4.10 reveals that W_T is always positive and trends upward, except during unloading where the work is non-negative.

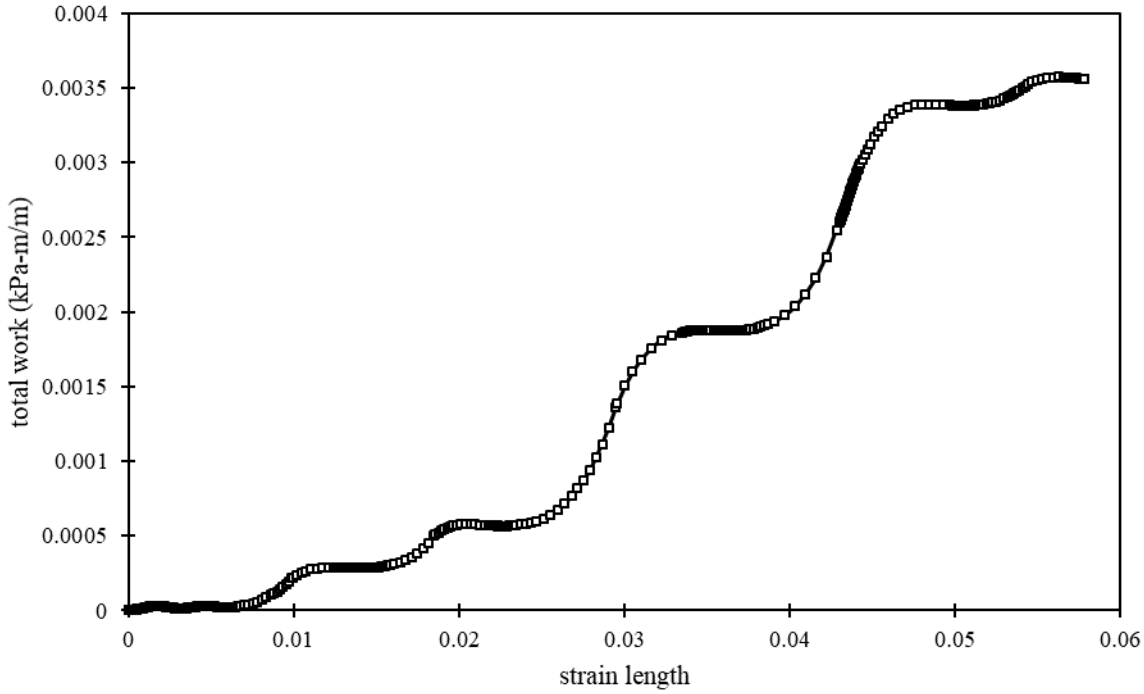

Figure 4.10 Total work done on subgrade due to load wander at 305 mm depth.

So while the deviatoric work and excess pore-water pressures may sometimes decrease, the total work steadily increases as a result of the dilative volume change. The F-15E simulated loading does not produce a *global* yielding response at 305 mm depth. However, a distinguishing feature of the MMM highlighted in Chapter 2 is that there is yielding occurring at the *mechanism* level (Stache et al., 2019b). The individual plastic sliders of the MMM shown in Figure 2.2 yield at different points, giving the effect of multiple nested yield surfaces (Stache et al., 2019b). Therefore, there is kinematic hardening taking place in the soil which cannot be accounted for by traditional elastic-plastic models. On this note, *plastic* work is also included here in Figure 4.10,

where the total work remains positive and increasing throughout the variations of the simulated load across the mat structure.

The role that complex load-induced principal stress axis rotation has on subgrade deformation response can be clarified by comparison to the corresponding results of a 2D-axisymmetric simulation implementing a pulsating cyclic load. Figure 4.11 shows the vertical displacements from the two loading conditions at 305-mm depth at different horizontal offsets from the load application.

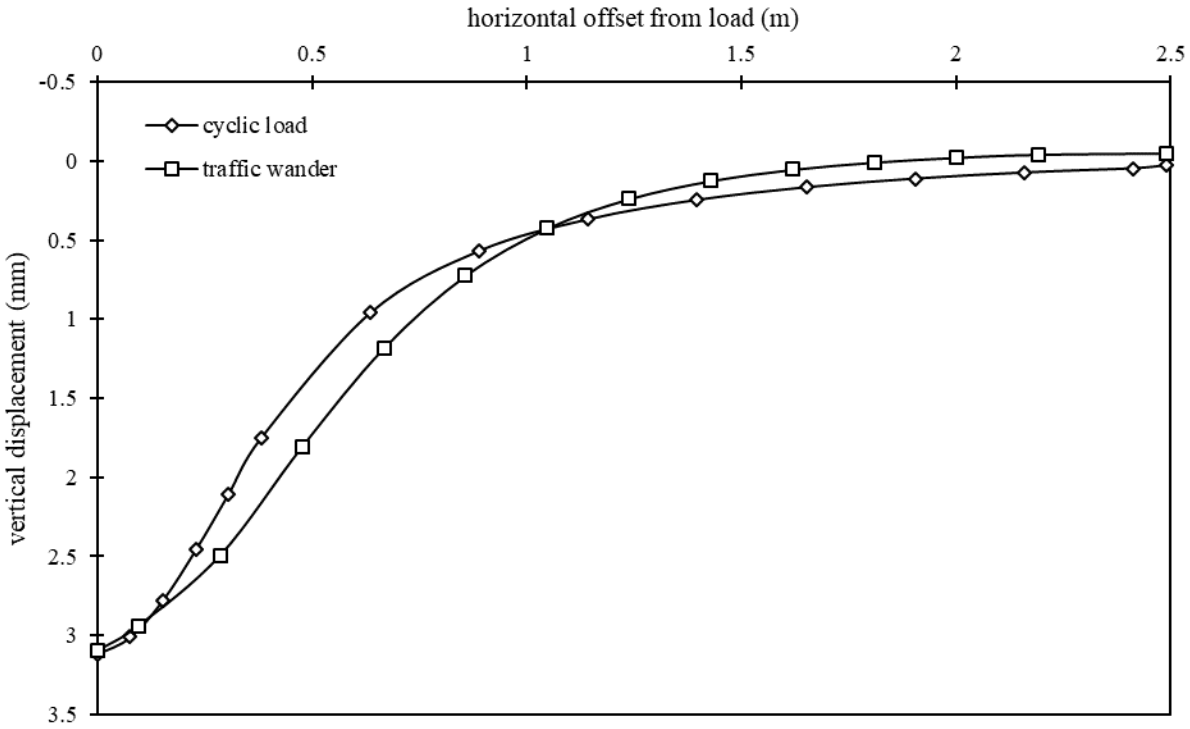

Figure 4.11 Comparison in deformation field between a full 3D FE model with traffic wander and 2D axisymmetric model with cyclic loading at 305 mm depth.

The cyclic loading plot is extracted at the seventh load cycle. The traffic wander plot is extracted during the seventh pass of the moving tire. The elastic deflections measured beneath the load are similar. However, the field of the deformation influence resulting from traffic wander extends noticeably farther outward than the cyclic load field of influence. As way of reminder, it is important to note that this is the first time this particular horizontal offset (i.e., traffic lane) has experienced the full load application in the traffic wander loading scenario. No load applications have occurred at the offsets to the right in the traffic wander plot. The first six passes all occurred at offsets to the left. The extended deformation influence is therefore a result of the rotations of the principal stress axes from the simulated moving tire. This important feature would be missed by a conventional elastic-plastic model with isotropic hardening (Neher et al., 2002).

There is evidence of the early stages of upheaval at more distant lateral offsets in the traffic wander plot. The cyclic load plot only shows compression across the offsets. The upheaval phenomenon revealed in the traffic wander simulation better matches what actually occurs on the outer edges of trafficking during full-scale testing. The outward extension of the field of deformation influence and the occurrence of upheaval near the edges of the test section will only become more pronounced with further trafficking. These phenomena, along with the variations in excess pore-water pressure, cannot be accurately simulated without the incorporation of traffic wander and the subsequent principal stress axis rotations. On this note, the MMM proved itself as a formidable soil constitutive model for capturing the complex stress histories and variations in excess pore-water pressures resulting from the principal stress axis rotations.

CHAPTER V

CONCLUSIONS AND RECOMMENDATIONS

5.1 Summary and Conclusions

In Chapter 2, an elasto-plastic kinematic hardening model based on endochronic theory known as the MMM was presented as a candidate constitutive model for complex problems in soils. A specified example of such complex problems was modeling pavement problems, which commonly involve different material types in the pavement structure and complex loading conditions that result in variations of principal stresses from traffic wander and kinematic hardening from repeating loading. The model was calibrated and tested against various soil types found in the unbound layers and subgrades of pavement structures, such as crushed limestone, sand, and clay. The model was also tested against a variety of different loading conditions characteristic of pavement problems, such as axisymmetric conditions in conventional triaxial compression tests, variations in principal stresses, and repeated stress reversals in resilient modulus tests, displaying a wide range of predictive capabilities.

In the calibration and testing of the model against the triaxial test data for the three materials, the MMM showed generally good agreement with the shear response across all confining pressures. The MMM also displayed the ability to capture changes in the excess pore water pressure for the clay, volume change in the Leighton Buzzard sand, and the load-unload legs for the limestone. The ratcheting behavior of the MMM fit well with the resilient modulus test data, while certain limitations in the model to capture the inevitable softening and hardening

effects that take place during initial loading and stress reversals, respectively, as a result of sample preparation were discussed. Furthermore, it was shown that the model was capable of representing the stress hardening effect in the resilient modulus that occurs in base course aggregates with increasing deviator stresses.

The proposed model is straightforward in its theoretical development but very robust in its capabilities to capture the aforementioned behaviors for different soil types. The calibration procedure requires only conventional triaxial and isotropic consolidation tests to extract global parameters, while a simple approach was shown for determining the mechanism parameters. For users desiring an even simpler method for estimating mechanism parameters, regression equations were also provided with reasonable fit to various soil types.

In Chapter 3, an investigation was conducted on the effects of different geometric and load-related parameters on the deformation response of subgrades under loaded an AM2 airfield mat system. A set of layered elastic and finite element analyses was used to look at the effects of aircraft load and gear configuration and cover material thickness and stiffness. Modeling-related issues not well understood for the numerical analysis of AM2 airfield mats, such as simulating the mat systems as a continuous plate or a jointed system and modeling the soil-mat interface under full-slip and no-slip conditions, were also investigated. The subgrade material model used in the FE simulations was the MMM. The FE model was compared with the standard linear and nonlinear layered elastic analysis programs *WinJULEA* and *KENLAYER*, and then compared against full-scale instrumented test data of the AM2 on a subgrade with CBR = 6. The response of the jointed mat FE model with the MMM subgrade matched well with the EPC and SDD field data. A summary of the findings from the sensitivity study are given below:

1. *Aircraft load and gear configuration* – aircraft with relatively low gross loads but high tire pressures will render a higher vertical stress and displacement response near the surface, but heavier aircraft with distributed loads across multiple wheel landing gears will show higher stress and displacements with depth. This finding is consistent with corresponding flexible pavement studies and is further confirmed in the other parametric studies below.
2. *Cover material thickness* – with relatively thin cover material thicknesses, lighter aircraft with higher tire pressures will affect subgrade response more than heavier aircraft with multi-wheel gears, but as cover material thickness increases, aircraft with higher gross weights transmit loads deeper into the subgrade than lighter aircraft. This was shown in terms of both subgrade compressive strain and the concept of cumulative damage.
3. *Cover material stiffness* – in a similar vein as thickness, as the cover material stiffness increases, the cumulative damage effect of heavier multi-wheel gear aircraft becomes more prominent compared to relatively lighter single wheel gear aircraft.
4. *Continuous plate and jointed mat* – modeling the airfield mat as a jointed system renders higher vertical stress and deformation response near the subgrade surface than modeling the mat as a continuous plate.
5. *Soil-mat interface conditions* – in general, modeling the soil-mat interface with a full-slip condition results in greater rotation of principal stress axes at the interface, whereas a no-slip condition results in greater shear stress mobilization at the interface. But there is still significant laboratory and field testing in this area required to understand the shear transfer phenomenon before the interface condition can be accurately modeled.

Chapter 4 examined the effects of principal stress axes rotation and variations in excess pore-water pressures on subgrade deformation response in AM2 airfield mat structures resulting from repeated, wandering aircraft loading. A 3D FE analysis implementing a time-staggered series of tire imprints was used to look at the resulting complex stress histories and variation in excess pore-water pressures. The subgrade material model used in the FE simulation was the Multi-Mechanical Model (MMM). The 3D FE model vertical stress and displacement time history matched very well with the corresponding earth pressure cell and single depth deflectometer measurements from full-scale instrumented testing of the AM2 on a subgrade with CBR = 6. The simulated pseudo-dynamic moving tire resulted in rotations of the principal stress axes and variations in the excess pore-water pressures. The field of deformation influence along the width of the simulated trafficked area extended farther outward than a similar axisymmetric FE simulation where only cyclic pulse loads were used. Results suggest that a full 3D modeling approach incorporating traffic wander can accurately capture the deformation response resulting from moving load conditions, fluctuating excess pore-water pressures, and principal stress rotations. Employing non-traditional plastic models such as the MMM provides further insight into the subgrade response under complex loading histories. Further studies are recommended with a view towards fully validating the efficacy of these models. In parallel, further efforts are needed on laboratory investigations on principal axes rotation with emphasis on loading paths imposed on pavement subgrades.

5.2 Recommendations for Future Research

Based on the findings of this study, the following recommendations are made for future research in this area:

- Currently, an initial stiffness approach is used for updating the deformations in the next time step in the UMAT. This method is beneficial for problems that do not experience significant material nonlinearity, since it does not require the recomputation of the stiffness matrix each time step. On the other hand, if significant plastic strains develop in the problem, a tangent stiffness formulation is required.
- As noted in Chapter 2 when simulating the resilient modulus test, lab test data show the initial stiffness and subsequent unload-reload stiffnesses are different. This phenomenon is not well understood or captured by most constitutive models. While external equilibrium has been achieved in the triaxial cell, there are residual stresses within the specimen resulting from sample preparation and initial seating of the specimen that must be accounted for through the initial internal state variables in the constitutive model. Specifying the initial internal state for soil materials is a problem common to all kinematic hardening models.
- The constitutive model was tested against shear and pore-water pressure response as well as the cyclic loading for resilient modulus testing (Chapter 2). The 3D FE models were validated against vertical stress and deformation test data from EPC and SDD data (Chapter 3 and 4). While the relative effects of principal stress rotations resulting from both the mat-soil interface condition and traffic wander were discussed, the model was not completely validated with respect to principal stress rotations. Further studies are recommended with a view towards fully validating the efficacy of these models. In parallel, further efforts are needed on

laboratory investigations on principal axes rotation with emphasis on loading paths imposed on pavement subgrades.

- This dissertation discusses the MMM's ability to represent the deformation response of both granular and *saturated* cohesive materials. It would be beneficial to implement the preliminary work of Berney (2004) on *partially saturated* cohesive soils into a UMAT in a 3D FE model. With respect to the *ABAQUS* UMAT syntax, this would require not only accounting for the partially saturated response in the driver, but also a reformulation of the material stiffness matrix. This effort could either be in conjunction with or separate from the first research need concerning the formulation of a *tangent* stiffness matrix. Furthermore, while laboratory test data exists for calibrating the MMM, full-scale instrumented testing with pore-water pressure data is needed for FE model validation with respect to pore-water pressure response.
- While the example used in this dissertation to implement the MMM was for expedient airfields constructed with AM2 mat systems to represent cohesive subgrade response, the MMM has much broader applications. The most related application would be implementation of the MMM into more conventional pavement problems to model unbound granular layer response.
- There were two important studies done in Chapter 3 concerning structural features of the AM2 mat that are not well understood: the load transfer mechanism in the mat joints and the bonding condition at the mat-soil interface. The two different connections used to link the AM2 mat panels together are complex and very difficult to model accurately. Furthermore, while the mat-soil interface condition

is typically modeled with an unbonded condition, this is not actually the case. The true behaviors of these two structural features need to be characterized in laboratory and field testing programs as they have vital importance in near surface subgrade response.

REFERENCES

ABAQUS (2017). ABAQUS user's manuals, Version 2017. Dassault Systèmes, Providence, RI, USA.

Al-Aghbari, M. Y., & Mohamedzein, Y. A. (2004). Model testing of strip footings with structural skirts. Proceedings of the Institution of Civil Engineers-Ground Improvement, 8(4), 171-177.

Alawaji, H., Alawi, M., Ko, H.Y., Sture, S., Peters, J.F. and Wood, D.M., 1990. Experimental observations of anisotropy in some stress-controlled tests on dry sand. In IUTAM/ICM Symposium: Antoni Sawczuk in Memoriam (pp. 251-264). Mechanical Engineering Publications.

Allou, F., Chazallon, C., & Hornych, P. (2007). A numerical model for flexible pavements rut depth evolution with time. International Journal for Numerical and Analytical Methods in Geomechanics, 31(1), 1-22.

Allou,F., Petit, C., Chazallon, C., & Hornych, P. (2010). Shakedown approaches to rut depth prediction in low-volume roads. Journal of engineering mechanics, 136(11), 1422-1434.

Arthur, J.K., Cutler, F., Dunstan, T., Ford, J. and Pulsford, J.R., Leavell, D. A., Peters, J. F. 1989. Design, Development, and Operation of a Directional Shear Cell (No. WES/TR/GL/89-16). ARMY ENGINEER WATERWAYS EXPERIMENT STATION VICKSBURG MS GEOTECHNICAL LAB.

Arthur, J.R.F., Bekenstein, S., Germaine, J.T. and Ladd, C.C., 1981. Stress path tests with controlled rotation of principal stress directions. In Laboratory shear strength of soil. ASTM International.

Arthur, J.R.F., Rodriguez del C, J.I., Dunstan, T. and Chua, K.S. (1980). Principal stress rotation: a missing parameter. Journal of the Geotechnical Engineering Division, 106(4), 419-433.

Atkinson, J. H., Richardson, D., & Stallebrass, S. E. (1990). Effect of recent stress history on the stiffness of overconsolidated soil. Géotechnique, 40(4), 531-540.

Baaser, H., & Heining, C. (2015). Application of Endochronic Plasticity on Simulation of Technical Rubber Components. KGK-KAUTSCHUK GUMMI KUNSTSTOFFE, 68(6), 90-92.

Bazant, Z. P., & Bhat, P. D. (1976). Endochronic theory of inelasticity and failure of concrete. ASCE J Eng Mech Div, 102(4), 701-722.

Bazant, Z. P., & Bhat, P. D. (1977). Prediction of hysteresis of reinforced concrete members. ASCE J Struct Div, 103(1), 153-167.

Bažant, Z. P., & Shieh, C. L. (1980). Hysteretic fracturing endochronic theory for concrete. Journal of the Engineering Mechanics Division, 106(5), 929-950.

Bažant, Z. P., Krizek, R. J., & Shieh, C. L. (1983). Hysteretic endochronic theory for sand. Journal of Engineering Mechanics, 109(4), 1073-1095.

Berney, I. V., & Ernest, S. (2004). A partially saturated constitutive theory for compacted fills (No. ERDC/GSL-TR-04-4). ENGINEER RESEARCH AND DEVELOPMENT CENTER VICKSBURG MS GEOTECHNICAL AND STRUCTURES LAB.

Bhatia, S.K. and Nanthikesan, S. (1987). The Development of Constitutive Relationship for Seismic Pore Pressure. Developments in Geotechnical Engineering, 42, 19-30.

Blázquez, R., Krizek, R. J., and Bažant, Z. P. (1980). "Site factors controlling liquefaction." J. Geotech. Engrg. Div., 106(7), 785–801.

Bonaquist, R. F., & Witczak, M. W. (1997). A comprehensive constitutive model for granular materials in flexible pavement structures. In Eighth International Conference on Asphalt Pavements Federal Highway Administration (No. Volume I).

Brown, D.N., and O.O. Thompson. (1973). Lateral distribution of aircraft traffic. Miscellaneous paper S-73-56. Vicksburg, MS: U.S. Army Engineer Waterways Experiment Station.

Burns, C. D., & Fenwick, W. B. (1966). Development of CBR Design Curves for Runways to be Surfaced with M8A1 (formerly T10) Steel Landing Mat (No. AEWES-Misc-Paper-4-817). Army Engineer Waterways Experiment Station, Vicksburg, MS.

Capabilities Development Document for Rapid Parking Ramp Expansion, United States Air Force Operational Capabilities Requirements Office, Washington, D.C., 2004.

Chan, F. W. K., & Brown, S. F. (1994). Significance of principal stress rotation in pavements. In PROCEEDINGS OF THE INTERNATIONAL CONFERENCE ON SOIL MECHANICS AND FOUNDATION ENGINEERING-INTERNATIONAL SOCIETY FOR SOIL MECHANICS AND FOUNDATION ENGINEERING (Vol. 4, pp. 1823-1823). AA BALKEMA.

Chazallon, C., Hornych, P., & Mouhoubi, S. (2006). Elastoplastic model for the long-term behavior modeling of unbound granular materials in flexible pavements. International Journal of Geomechanics, 6(4), 279-289.

Cuellar, V., & Bazant, Z. P. (1977). Densification and hysteresis of sand under cyclic shear. J. Geotechnical Engineering Div. Proc. ASCE, 103 (GT5), 399-416.

Donaghe, R. T., & Gilbert, P. A. (1983). Cyclic Rotation of Principal Planes to Investigate Liquefaction of Sands (No. WES/MP/GL-83-24). ARMY ENGINEER WATERWAYS EXPERIMENT STATION VICKSBURG MS GEOTECHNICAL LAB.

Doyle, J. D., Howard, I. L., Gartrell, C. A., Anderton, G. L., Newman, J. K., & Berney IV, E. S. (2012). Full-scale instrumented testing and three-dimensional modeling of airfield matting systems. International Journal of Geomechanics, 14(2), 161-170.

Duncan, J. M., & Chang, C. Y. (1970). Nonlinear analysis of stress and strain in soils. Journal of Soil Mechanics & Foundations Div. 96(5), 1629-1653.

Elizaroughi, A. A. (1978). Application of endochronic constitutive law to one-dimensional liquefaction of sand. Ph.D. Thesis Northwestern Univ., Evanston, IL.

Foster, D. C. (2007). Decks for Rapid Runway Mat Application. Air Force Research Lab Wright-Patterson AFB, OH, Materials and Manufacturing Directorate.

Gallage, C., Dareeju, B., Dhanasekar, M., & Ishikawa, T. (2016). Effects of principal stress axis rotation on unsaturated rail track foundation deterioration. Procedia Engineering, 143, 252-259.

Garcia, L., T.W. Rushing, and Q.S. Mason. (2014a). AM2 25 CBR Subgrade Sensitivity Test, ERDC/GSL TR-14-7, U.S. Army Engineer Research and Development Center, Vicksburg, MS.

Garcia, L., T.W. Rushing, B.A. Williams, and C.A. Rutland. (2014b). AM2 100 CBR Subgrade Sensitivity Test, ERDC/GSL TR-14-37, U.S. Army Engineer Research and Development Center, Vicksburg, MS.

Gartrell, C.A. (2007). Full-Scale Instrumented Testing and Analysis of Matting Systems for Airfield Parking Ramps and Taxiways, ERDC/GSL TR-07-33, U.S. Army Engineer Research and Development Center, Vicksburg, MS.

Ge, Y. N., & Chen, G. (2012). Validation on the mechanical models of asphalt pavement structures with field measured data associated with increasing freight movements (No. 25-1121-0001-241). Mid-America Transportation Center.

Gonzalez, C.R., and T.W. Rushing. (2010). Development of a New Design Methodology for Structural Airfield Mats, International Journal of Pavement Research and Technology, 3(3): 102-109.

Guo, L., Chen, J., Wang, J., Cai, Y., & Deng, P. (2016). Influences of stress magnitude and loading frequency on cyclic behavior of K0-consolidated marine clay involving principal stress rotation. Soil Dynamics and Earthquake Engineering, 84, 94-107.

Gupta, A., Kumar, P., & Rastogi, R. (2015). Mechanistic–empirical approach for design of low volume pavements. International Journal of Pavement Engineering, 16(9), 797-808.

Gutierrez, M., Ishihara, K. and Towhata, I., 1991. Flow theory for sand during rotation of principal stress direction. Soils and foundations, 31(4), pp.121-132.

Habiballah, T., & Chazallon, C. (2005). An elastoplastic model based on the shakedown concept for flexible pavements unbound granular materials. International Journal for Numerical and Analytical Methods in Geomechanics, 29(6), 577-596.

Hau, K. W., McDowell, G. R., Zhang, G. P., & Brown, S. F. (2005). The application of a three-surface kinematic hardening model to repeated loading of thinly surfaced pavements. Granular Matter, 7(2-3), 145-156.

Helwany, S., Dyer, J., & Leidy, J. (1998). Finite-element analyses of flexible pavements. Journal of Transportation Engineering, 124(5), 491-499.

Hornych, P., Chazallon, C., Allou, F., & El Abd, A. (2007). Prediction of permanent deformations of unbound granular materials in low traffic pavements. Road Materials and Pavement Design, 8(4), 643-666.

Houlsby, G. T. (1981). Study of plasticity theories and their applicability to soils. Doctoral dissertation, University of Cambridge.

Hsu, Y.S., Jain, S.K., and Griffin, Jr., O. H. (1991). Verification of endochronic theory for nonproportional loading paths. ASCE J Eng Mech Div, 117(1), 110-131.

Hu, X., & Walubita, L. F. (2010). Effects of layer interfacial bonding conditions on the mechanistic responses in asphalt pavements. Journal of Transportation Engineering, 137(1), 28-36.

Huang, Y. H. (1993). *KENLAYER* computer program. Pavement Analysis and Design, 100-167.

Inam, A., Ishikawa, T., & Miura, S. (2012). Effect of principal stress axis rotation on cyclic plastic deformation characteristics of unsaturated base course material. Soils and Foundations, 52(3), 465-480.

Ioannides, A. M., & Donnelly, J. P. (1988). Three-dimensional analysis of slab on stress-dependent foundation (No. 1196).

Ishihara, K. and Towhata, I., 1983. Sand response to cyclic rotation of principal stress directions as induced by wave loads. Soils and foundations, 23(4), pp.11-26.

Issa, C. A., Peters, J. F., & Jones, E. W. (1995). Structural effects of perlite compaction on cryogenic storage vessels subjected to thermal. Int. J. Pres. Ves. & Piping, 64, 51-65.

Jain, S.K. (2012). Material modeling by endochronic theory: the Virginia Tech experience. International Journal for Computational Methods in Engineering Science and Mechanics, 13(5), 329-333.

Jefferies, M., Shuttle, D., & Been, K. (2015). Principal stress rotation as cause of cyclic mobility. Geotechnical Research, 2(2), 66-96.

Johnson, D., Sukumaran, B., Mehta, Y., & Willis, M. (2007, April). Three dimensional finite element analysis of flexible pavements to assess the effects of wander and wheel configuration. In FAA Worldwide Airport Technology Transfer Conference.

Khoei, A. R., & Jamali, N. (2005). On the implementation of a multi-surface kinematic hardening plasticity and its applications. International Journal of Plasticity, 21(9), 1741-1770.

Kim, M., & Lee, J. H. (2011). Study on nonlinear pavement responses of low volume roadways subject to multiple wheel loads. Journal of Civil Engineering and Management, 17(1), 45-54.

Klisiński, M. (1988). Plasticity theory based on fuzzy sets. Journal of Engineering Mechanics, 114(4), 563-582.

Klisinski, M., Alawi, M.M, Sture, S., Ko, H.-Y., and Muir Wood, D. (1987). Elasto-plastic model for sand based on fuzzy sets. International Workshop on Constitutive Equations for Granular NonCohesive Soils, Case Western Reserve University.

Kruntcheva, M. R., Collop, A. C., & Thom, N. H. (2005). Effect of bond condition on flexible pavement performance. Journal of transportation engineering, 131(11), 880-888.

Lade, P. V. (2005). Overview of constitutive models for soils. In Soil constitutive models: Evaluation, selection, and calibration, Proc. Geo-Frontiers Congress 2005, January 24-26, 2005, Austin, Texas, ASCE, GSP 128, 1-34.

Lekarp, F., & Dawson, A. (1998). Modelling permanent deformation behaviour of unbound granular materials. Construction and Building Materials, 12(1), 9-18.

Leski, A., Wesołowski, M., & Stefaniuk, M. (2012). Evaluation of mobile, composite airfield mat. Composites Theory and Practice, 12(4), 237-244.

Matsuoka, H., & Nakai, T. (1974, December). Stress-deformation and strength characteristics of soil under three different principal stresses. In Proceedings of the Japan Society of Civil Engineers (Vol. 1974, No. 232, pp. 59-70). Japan Society of Civil Engineers.

McDowell, G. R., & Hau, K. W. (2004). The Use of a Kinematic Hardening Model for Estimating Subgrade Stiffness in Layered-elastic Analyses. International Journal of Pavement Engineering, 5(2), 53-59.

McDowell, G.R. & Hau, K.W. (2003). A Simple Non-Associated Three Surface Kinematic Hardening Model. Geotechnique, 53(4), 433-437.

Mindlin, R.D. (1951). Influence of Rotatory Inertia and Shear on Flexural Motions of Isotropic Elastic Plates, Journal of Applied Mechanics, Vol. 18, pp. 31-38.

Miner, M.A. (1945). Cumulative damage in fatigue. Journal of Applied Mechanics, vol. 12, no. 3, pp. A159–A164.

Nakata, Y., Hyodo, M., Murata, H. and Yasufuku, N., 1998. Flow deformation of sands subjected to principal stress rotation. Soils and Foundations, 38(2), pp.115-128.

Neher, H.P., Cudny, M., Wiltafsky, C. and Schweiger, H.F., 2002. Modelling principal stress rotation effects with multilaminate type constitutive models for clay. In Proc. of 8th International Symposium on Numerical Models in Geomechanics, Rome (pp. 41-47).

Nelson, R.B. and Dorfmann, A. (1995). Parallel elastoplastic models of inelastic material behavior. Journal of Engineering Mechanics, 121(10), pp.1089-1097).

PCASE2.09.05. Pavement-Transportation Computer Assisted Structural Engineering software, web site https://transportation.erdc.dren.mil/pcase/software.aspx

Peters, J.F. (1987). Internal variable model for frictional materials. In Proc. of Workshop on Constitutive Equations for Granular Non-cohesive Soils, Cleveland, Balkema (pp. 551-569).

Peters, J.F. (1998). Design Requirements for Computer Program to Analyze Large Seismically Induced Deformations. In Proc. of First US-Japan Workshop on Advanced Research on Earthquake Engineering for Dams, 12-14 November 1996 (No. WES/MP/GL-98-1). ARMY ENGINEER WATERWAYS EXPERIMENT STATION VICKSBURG MS GEOTECHNICAL LAB.

Qian, J. G., Wang, Y. G., Yin, Z. Y., & Huang, M. S. (2016). Experimental identification of plastic shakedown behavior of saturated clay subjected to traffic loading with principal stress rotation. Engineering geology, 214, 29-42.

Qiu, Y., Dennis, N., & Elliott, R. (2000). Design criteria for permanent deformation of subgrade soils in flexible pavements for low-volume roads. Soils and foundations, 40(1), 1-10.

Rushing, T.W. (2018). Performance Prediction Relationships for AM2 Airfield Matting Developed from Full-Scale Accelerated Testing and Laboratory Experimentation, ERDC/GSL TR-18-1, U.S. Army Engineer Research and Development Center, Vicksburg, MS.

Rushing, T.W., and J.S. Tingle. (2007). AM2 and M19 Airfield Mat Evaluation for the RPRE Program, ERDC/GSL TR-07-5, U.S. Army Engineer Research and Development Center, Vicksburg, MS.

Rushing, T.W., N. Torres, and Q. Mason. (2008a). AM2 10 CBR Subgrade Sensitivity Test for the Rapid Parking Ramp Expansion Program, ERDC/GSL TR-08-13, U.S. Army Engineer Research and Development Center, Vicksburg, MS.

Rushing, T.W., and Q.S. Mason. (2008b). AM2 15 CBR Subgrade Sensitivity Test for the Rapid Parking Ramp Expansion Program, ERDC/GSL TR-08-25, U.S. Army Engineer Research and Development Center, Vicksburg, MS.

Sadrekarimi, A. (2016). Static Liquefaction Analysis Considering Principal Stress Directions and Anisotropy. Geotechnical and Geological Engineering, 34(4), 1135-1154.

Sahoo, U. C., & Reddy, K. S. (2010). Effect of nonlinearity in granular layer on critical pavement responses of low volume roads. International Journal of Pavement Research and Technology, 3(6), 320-325.

Schofield, A., & Wroth, P. (1968). Critical state soil mechanics (Vol. 310). London: McGraw-Hill.

Schwartz, C.W. and Yau, A.Y.Y. (2001), “Cyclic plasticity characterization of unbound pavement materials.” Computer Methods and Advances in Geomechanics, Desai et al.

Shi, W., Wang, J., Guo, L., Hu, X., Fu, H., Jin, J., & Jin, F. (2018). Undrained cyclic behavior of overconsolidated marine soft clay under a traffic-load-induced stress path. Marine Georesources & Geotechnology, 36(1), 163-172.

Smith, D. M. (2000). Response of Granular Layers in Flexible Pavements Subjected to Aircraft Loadings (No. ERDC/GL TR-00-3). ENGINEER RESEARCH AND DEVELOPMENT CENTER VICKSBURG MS GEOTECHNICAL LAB.

Stache, J. M., Gonzalez, C. R., Rushing, T. W., & Garcia, L. I. (2019a). Proposing an Updated AM2 Mat Performance Criteria Model. Transportation Research Record, 0361198118825123.

Stache, J. M., Peters, J. F., Hammi, Y., & Vahedifard, F. (2019b). A kinematic hardening model based on endochronic theory for complex stress histories. Computers and Geotechnics, 114, 103117.

Stache, J. M., Vahedifard, F., Peters, J. F., (2019c). "Critical Factors in Subgrade Rutting Failures of Airfield Mats over Soft Soils under Static Loading." International Journal of Geomechanics, ASCE (In Review).

Sture, S., Budiman, J.S., Ontuna, A.K. and Ko, H.Y., 1987. Directional shear cell experiments on a dry cohesionless soil. Geotechnical Testing Journal, 10(2), pp.71-79.

Thompson, A. B., & Burns, C. D. (1960). Criteria for designing runways to be surfaced with landing mat and membrane-type materials. Technical Rep. 3, 539.

Thompson, M. R., & Elliott, R. P. (1985). *ILLI-PAVE* based response algorithms for design of conventional flexible pavements. Transportation Research Record, 1043, 50-57.

Tolentino, R., Rahman, M. M., Cameron, D., & Karim, R. (2019). Prediction of Flexible Pavement's Unbound Granular Materials Using Elasto-Plastic Model SANISAND. In Airfield and Highway Pavements 2019: Testing and Characterization of Pavement Materials (pp. 481-492). Reston, VA: American Society of Civil Engineers.

Ulery Jr, H. H., & Wolf, D. P. (1971). Thickness requirements for soils beneath landing mats; bare base support (No. AEWES-Misc-Paper-S-71-3). Army Engineer Waterways Experiment Station, Vicksburg, MS.

Valanis, K. C. (1971). Irreversibility and existence of entropy. International Journal of Non-Linear Mechanics, 6(3), 337-360.

Valanis, K. C., & Peters, J. F. (1988). Thermodynamics of Frictional Materials. Report 1. Constitutive Theory of Soils with Dilatant Capability (No. WES/TR/GL-88-20). ARMY ENGINEER WATERWAYS EXPERIMENT STATION VICKSBURG MS GEOTECHNICAL LAB.

Valanis, K. C., & Peters, J. F. (1991). An endochronic plasticity theory with shear-volumetric coupling. Journal for Numerical and Analytical Methods in Geomechanics, 15(2), 77-102.

Valanis, K. C., & Read, H. E. (1980). New endochronic plasticity model for soils. Interim report (No. EPRI-NP--1388). Systems.

Valanis, K. C., & Read, H. E. (1986). An endochronic plasticity theory for concrete. Mechanics of Materials, 5(3), 277-295.

Watanabe, O., & Atluri, S. N. (1985). A new endochronic approach to computational elastoplasticity: example of a cyclically loaded cracked plate. Journal of Applied Mechanics, 52(4), 857-864.

Werkmeister, S., Canon Falla, G., & Oeser, M. (2015). Analytical design methodology for thin surfaced asphalt pavements in Germany. In Airfield and Highway Pavements 2015 (pp. 730-741).

White, T. D. (1971). Theoretical landing mat analysis (No. AEWES-Misc-Paper-S-71-21). Army Engineer Waterways Experiment Station Vicksburg, MS.

Willis, M., Johnson, D., & Sukumaran, B. (2006). Three-Dimensional Finite Element Analysis of Flexible Airport Pavements for the Next Generation of Aircrafts. In Airfield and Highway Pavements. The 2006 Airfield and Highway Pavement Specialty Conference American Society of Civil Engineers.

WinJULEA, (2003). Layered Elastic Analysis software, available through the Pavement-Transportation Computer Assisted Structural Engineering (*PCASE*) software, web site https://transportation.erdc.dren.mil/pcase/software.aspx

Wu, Z., Chen, X., & Yang, X. (2011). Finite element simulation of structural performance on flexible pavements with stabilized base/treated subbase materials under accelerated loading (No. FHWA/LA. 10/452). Louisiana Transportation Research Center.

Yang, Q., Tang, Y., Yuan, B., & Zhou, J. (2019). Cyclic stress–strain behaviour of soft clay under traffic loading through hollow cylinder apparatus: effect of loading frequency. Road Materials and Pavement Design, 20(5), 1026-1058.

Zienkiewicz, O. C., Chang, C. T., & Hinton, E. (1978). Non-linear seismic response and liquefaction. International Journal for Numerical and Analytical Methods in Geomechanics, 2(4), 381-404.